2015

Synthetic and biological investigations into hypoxia-activated anti-tumour codrugs

Nicholas Kirk
University of Wollongong

Synthetic and Biological Investigations into Hypoxia-Activated Anti-Tumour Codrugs

A thesis submitted in fulfilment of the requirements for the award of the degree

Doctor of Philosophy

from

University of Wollongong

by

Nicholas Kirk

Bachelor of Medicinal Chemistry (Advanced, Honours 1)

School of Chemistry

2015

Declaration

I, Nicholas Kirk, declare that this thesis, submitted in fulfilment of the requirements for the award of Doctor of Philosophy in the School of Chemistry, University of Wollongong, is wholly my own work unless otherwise referenced or acknowledged. The work has not been submitted for qualification at any other academic institution.

Nicholas Kirk

09/11/2015

Acknowledgements

Firstly, I would like to thank my supervisor Assoc. Prof. Michael Kelso. Without your guidance, I would not have been able to make even the first step of what was a very rewarding experience. Thank you for all of the time and energy spent explaining, guiding and inspiring me to do the best I could. I have learned a lot from working under you. To Pichit: your work ethic, insight and methodical approach to chemistry was an inspiration. Your consistent cheer was even more impressive than that. Almost everything I achieved was by standing on the shoulders of your work. To Rhys, Claudia, Anna Bezos and Tony Willis and everyone else who directly helped with this project, thanks for your contributions. I wouldn't have completed anything close to what I have without your hard work. To Marie and Nat: thank you for all your help in the scary world of tissue culture. Thank you for being so welcoming and generous with your time and energy.

To Ardeshir (dorood!), Alex (B.O. Basher), Ben (ooh bay-bee), Con(athon), Louise, Ramesh, Naveen and all of the other Kelso Lab and School of Chemistry members (especially Alireza): thanks for all the laughs, the singing and yelling, all the ideas, the occasional strangely deep discussions and inappropriate translations. I'm sure I'll see you all again soon.

To mum, dad, my brothers and friends: thank you for (trying to) encourage me to have a life. Thank you for being there even when we were in very different places, both figuratively and literally.

Finally to Erica: thank you for all of your love and support. Thank you for understanding the frustration and appreciating the wins and being beside me on the whole rollercoaster of experiences that this ended up being.

Publications Arising from this Thesis

1. Sudta, P., Kirk, N., Bezos, A., Gurlica, A., Mitchell, R., Weber, T., Willis, A.C., Prabpai, S., Kongsaeree, P., Parish, C.R., Suksamrarn, S., Kelso, M.J., Synthesis, Structural Characterisation, and Preliminary Evaluation of Non-Indolin-2-one-based Angiogenesis Inhibitors Related to Sunitinib (Sutent®). *Aust. J. Chem.* **2013**, *66*, 864.

Manuscripts in Preparation

2. Kirk, N., Sudta, P., Suksamram, S., Kelso, M.J. Design and synthesis of a reductively activated anti-tumour codrug. Target Journal: *ChemMedChem*

3. Kirk, N., Sudta, P., Bezos, A., Ries, C., Willis, A.C., Parish, C.R., Ranson, M., Kelso, M.J. Synthesis and biological assessment of 2-aryl-3*H*-pyrrolizin-3-ones angiogenesis inhibitors. Target Journal: *Bioorg. Med. Chem. Lett.*

4. Kirk, N., Sudta, P., Willis, A.C., Kelso, M.J. Synthesis and unusual reactivity of 3-(3,5-dimethyl-1H-pyrrol-2-yl)-2-(2-nitrophenyl)acrylic acid. Target Journal: *Tet. Lett.*

Abstract

Tumour-selective, non-cytotoxic chemotherapeutics are much sought after in oncology. Two cancer-selective drug types are angiogenesis inhibitors, drugs which halt the growth of new blood vessels in tumours, and hypoxia-activated prodrugs, which are non-toxic agents that are activated into cytotoxins selectively within tumours. It is possible to conceive a dual-action prodrug (a.k.a. codrug) which releases both an angiogenesis inhibitor and a cytotoxin selectively within a tumour after bio-reductive activation. Specifically, prodrugs designed to release nitrogen mustard cytotoxins along with SU5416 from a 2-nitrophenylacetamide precursor were of particular interest.

A synthesis of the prototype hypoxia-activated anti-tumour codrug (*Z*)-**1** was successfully achieved with an overall yield of 12% over 7 steps. A synthetically more convenient route through carboxylic acid intermediate (*Z*)-**5** was unsuccessful, as ester/amide coupling conditions produced the cyclisation product 5,7-dimethyl-2-(2-nitrophenyl)-3*H*-pyrrolizin-3-one **14** in high yield. Instead, it was necessary to optimise a step-wise synthesis through *N*-(4-(bis(*O*-tert-butyldimethylsilyl-2-hydoxyethyl)amino)phenyl)-2-(2-nitrophenyl)acetamide **8**, then perform a Knoevenagel condensation with *N*-protected pyrrole aldehyde **9** to form (*Z*)-**7**. After deprotection and chlorination of (*Z*)-**7**, prototype codrug (*Z*)-**1** was obtained as an air-stable solid.

In order to demonstrate that reduction of (*Z*)-**1** spontaneously produced SU5416 as necessary for *in vivo* activity, chemical NO_2 reductions were performed. (*Z*)-**1** was demonstrated to spontaneously produce SU5416 and the *N*-hydroxy SU5416 analogue **2**-OH in good yields after reduction. Similar results were observed for the ethyl ester (*Z*)-**10** and anilide (*Z*)-**29**. These results represented a crucial proof-of-concept for the scaffold as a codrug and supported further investigation into (*Z*)-**1** in biological systems.

Several side reactions from the synthesis of (*Z*)-**1** were also explored in depth. Indoline-*N*-oxides **15** and **16** were the result of attempted amide couplings of **5** and HBTU or HATU with *N*,*N*-dimethyl-*p*-phenylenediamine (**15**) or *p*-phenylenediamine (**16**). Significant efforts were made to delineate the reaction mechanism. Through NMR studies, it was shown that (*Z*)-**5** spontaneously decarboxylated in chloroform to form (*E*)-alkene **18**. It was also shown that *p*-phenylenediamine reacted with HBTU or HATU in solution to form 2-(4-aminophenyl)-1,1,3,3-tetramethylguanidine **19**. A reaction mechanism combining these two transformations to form **15** was proposed, supported by mass spectral data. **16** was also shown to spontaneously form indolinone-*N*-oxide **17**, a novel analogue of a known antimalarial series, which showed IC_{50} = 381 nM against the K1 strain of *P. falciparum*.

Alkene intermediates synthesised during optimisation of the Knoevenagel condensation necessary for (*Z*)-**1** were tested for activity in a rat aortic ring angiogenesis assay. This assay showed that small ester derivatives such as (*E*)-**10** and (*Z*)-**10** represented a novel class of angiogenesis inhibitors, however all amide analogues tested (such as anilide (*Z*)-**29**) were inactive. The structurally similar 3*H*-pyrrolizin-3-one **14** was also shown to be a potent angiogenesis inhibitor. A facile one-step synthesis of substituted 2-aryl derivatives of **14** was developed, using pyrrole carboxaldehyde **4** and commercially available phenylacetic acid derivatives. 18 derivatives were synthesised through this reaction and tested for angiogenesis inhibition in a semi-quantitative HUVEC tube formation assay. Compound **14** was shown to be the most potent compound, with unsubstituted phenyl derivative **51** and *o*-fluoro derivative **69** also producing significant inhibition of HUVEC tube formation. Compounds **14** and **51** were then tested in a rat aortic ring angiogenesis assay which confirmed their inhibitive capacity, with compound **14** producing similar inhibitory potency to SU5416.

Abbreviations

ADMET	Absorption, distribution, metabolism, excretion, toxicity
ANU	Australian National University
AR	Androgen receptor
ATP	Adenosine triphosphate
CML	Chronic myelogenous leukaemia
DCC	*N*,*N*'-Dicyclohexylcarbodiimide
DIPEA	Diisopropylethylamine
DMAP	4-Dimethylaminopyridine
DMF	Dimethylformamide
DMPD	*N*,*N*-dimethyl-*p*-phenylenediamine
DMSO	Dimethyl sulfoxide
DNA	Deoxyribonucleic acid
EDCI	1-Ethyl-3-(3-dimethylaminopropyl)carbodiimide
EGF(R)	Epidermal growth factor (receptor)
Et	Ethyl
ESI-MS	Electrospray ionisation mass spectrometry
FDA	U.S. Food and Drug Administraiton
F.O.V.	Field of view
(FT)IR	(Fourier transform) Infrared spectroscopy
5-FU	5-fluorouracil
FVP	Flash vacuum pyrolysis
HATU	1-[Bis(dimethylamino)methylene]-1*H*-1,2,3-triazolo[4,5-b]pyridinium 3-oxide hexafluorophosphate

HBTU	2-(1*H*-benzotriazol-1-yl)-1,1,3,3-tetramethyluronium hexafluorophosphate
HER2	Human epidermal growth factor receptor 2
HIF-1	Hypoxia-inducible factor-1
hLM	Human liver microsomes
HOAt	1-Hydroxy-7-azabenzotriazole
HOBt	*N*-Hydroxybenzotriazole
HRMS	High resolution mass spectrometry
HUVEC	Human umbilical vein endothelial cells
hTERT	Human telomerase reverse transcriptase
KHMDS	Potassium hexamethyldisilazide
LDA	Lithium diisopropylamide
mAb	Monoclonal antibody
MAPK	Mitogen-activated protein kinase
Me	Methyl
mLM	Mouse liver microsomes
MMP	Matrix metalloproteinase
MMAE	Monomethyl auristatin-E
mRNA	Messenger RNA
Ms	Mesyl
mTOR	Mammalian target of rapamycin
NADPH	Nicotinamide adenine dinucleotide phosphate
NMR	Nuclear magnetic resonance
PDGF(R)	Platelet-derived growth factor (receptor)
PET	Positron emission tomography

Ph	Phenyl
PI3K	Phosphoinositide 3-kinase
PPD	*p*-phenylenediamine
RBC	Red blood cell
RNA	Ribonucleic acid
RTK(i)	Receptor tyrosine kinase (inhibitor)
SAR	Structure-activity relationship
siRNA	Small interfering RNA
TAV	Tumour-associated vasculature
TBAF	Tetrabutylammonium fluoride
TBDMS	Tert-butyl dimethylsilyl
^{t}Bu	Tert-butyl
TEA	Triethylamine
TGF-β	Transforming growth factor-β
THF	Tetrahydrofuran
TLC	Thin layer chromatography
TMS	Trimethylsilyl
TMU	Tetramethylurea
TNF	Tumour necrosis factor
uPA	Urokinase plasminogen activator
UV-Vis	Ultraviolet-Visible light spectroscopy
VEGF(R)	Vascular endothelial growth factor (receptor)

Table of Contents

List of Figures

List of Tables

List of Schemes

Chapter 1: Introduction

1.1 Cancer Statistics

Cancer is a highly complex group of diseases characterised by uncontrolled proliferation of cells. In 2011, cancer accounted for about 3 in every 10 deaths in Australia, with lung and gastrointestinal tumours the leading contributors.[1,2] Cancer is also responsible for the greatest health-care economic burden in Australia, costing upwards of $3.8 billion per year (7.2% of all direct health expenditure).[1] Domestic research efforts in cancer attract $358 million in funding annually, representing 22% of the health and medical research budget.[1] Improvements in early detection, diagnosis and treatment have drastically improved prognoses for cancer patients over the years.[3] In Australia, 5-year survival rates have improved over 25 years from 45.1% to 66.1%.[1,2] The mortality-to-incidence ratio for all cancer types in Australia has declined at a similar rate over the same period, representing a significant improvement in successful treatment (Figure 1.1).[1]

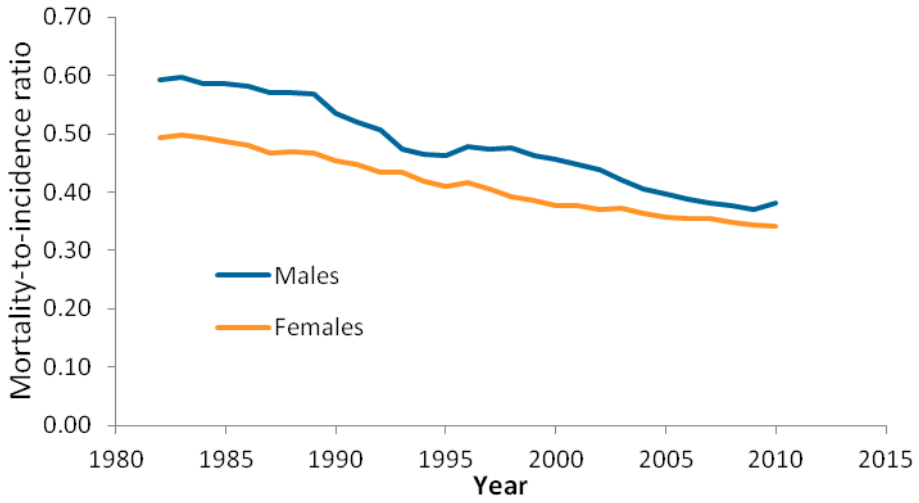

Figure 1.1. Mortality-to-incidence ratios for all cancer types in Australia from 1982 to 2015.[1]

1.2 Molecular Mechanisms of Cancer

Cell division is an intricately controlled process where an array of positive and negative feedback mechanisms finely balance DNA replication, mitosis and apoptosis (programmed cell death) to maintain healthy tissues. This balance is managed by layers of signalling pathways that modulate a plethora of cellular processes involved in tissue homeostasis.[4,5] Cancer occurs when a population of cells is no longer subject to the entirety of these control processes and cell proliferation proceeds to the detriment of the host organism. The simplistic historical notion that cancer is a disease of proliferation has been replaced in recent times by an evolutionary model.[5] According to this model, cancer occurs when a population of cells accumulates a variety of mutations that gives them a survival advantage over neighbouring healthy cells.[5] While cancer actually represents a myriad of different diseases, a number of commonalities are observed amongst most malignant tumours.[5] These include:

- an ability to signal their own growth and bypass anti-growth signals.
- insensitivity to apoptotic messages.
- an ability to overcome internal cell division limits.
- consistent promotion of angiogenesis (growth of new blood vessels).
- superior invasive and metastatic capabilities

With some or all of these characteristics, a population of mutated cells (the cancer) is able to grow unchecked, extravasate into the bloodstream and metastasise to distant tissues to create secondary tumours that can lead to death.

1.3 Traditional Cancer Treatment Protocols

Surgical resection and radiation therapy remain the primary methods of treatment for solid tumours as they allow direct, targeted action on cancerous tissues. Modern cancer treatments combine these with chemotherapy in order to improve outcomes and increase the likelihood of remission.[6]

There are many methods of applying chemotherapy in modern cancer treatments. For instance, drugs are often used as 'adjuvant' therapy to kill circulating cancerous or pre-cancerous cells remaining after surgery and/or radiation.[7–9] Conversely, 'neoadjuvant' therapy uses chemotherapy before other treatments in order to reduce the tumour mass and consequently the extent, complexity and risks of surgery, or the effects of radiotherapy on surrounding tissues.[10,11] Anti-cancer drugs can also be used as palliative agents (i.e. to reduce pain and improve quality of life) in terminal patients.[12–15]

Non-solid cancers are treated primarily with chemotherapy. Treatment of leukaemia (cancer of leukocytes or white blood cells), for instance, is typically layered into multiple chemotherapy protocols. The first aims to kill cancerous cells such that they are undetectable in a patient's blood. This is known as 'remission induction' and involves aggressive treatment with combinations of cytotoxins.[15–18] A second regimen, termed 'consolidation', is then cycled for months or even years to reduce the risk of relapse.[16,19,20] These protocols can also be combined with radiation and bone marrow transplants depending on the nature and severity of a patient's disease. Chemotherapy is also a primary treatment for many lymphomas (cancers derived from lymphocytes).[21]

The availability of biochemical and genetic methods for analysis of cancers has allowed the molecular mechanisms behind many cancer sub-types to be determined. This has spurred the development of more selective chemotherapeutic agents that specifically

target the mechanism(s) identified, reducing the need for cytotoxic agents. These modern drugs tend to be less harmful to patients.[22] Indeed, most FDA-approved chemotherapeutics these days tend to be targeted agents, which are often fast-tracked for approval.[23] Aggressive combination chemotherapy treatments continue to be used, but the physiological burden on patients has been reduced significantly by inclusion of targeted agents.[24]

1.4 Types of chemotherapeutics

Traditional cytotoxic chemotherapeutics target DNA replication and cell division under the premise that cancer cells are selectively killed over healthy cells due to their higher proliferation rates. Classes of cytotoxic agents include the DNA alkylators, DNA intercalators, anti-metabolites and tubulin-binders. Chemotherapy treatments have generally used combinations of these agents to reduce the risk of persistent cancer cells and adaptive resistance.[7,25,26]

DNA-alkylators, such as melphalan, chlorambucil and carmustine (Figure 1.2(a)), function by alkylating DNA (usually via the nucleophilic guanine N7) and cross-linking strands (Figure 1.2(b)).[27,28] These lesions can disrupt DNA replication directly by causing strand-breakages and preventing the binding of proteins, or indirectly by promoting apoptosis through formation of unnatural DNA complexes.[28] Cisplatin and the related carboplatin are traditional DNA alkylators that continue to be used due to their effectiveness in treating testicular cancer. Use of these agents has seen 5-year survival rates in Australia increase to nearly 98%.[1] In contrast, chlorambucil and melphalan tend to be limited to palliative therapy due to their high immunotoxicity.[29,30]

(a)

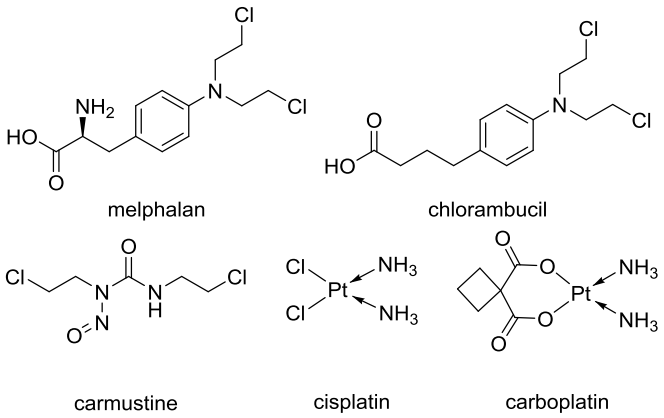

(b)

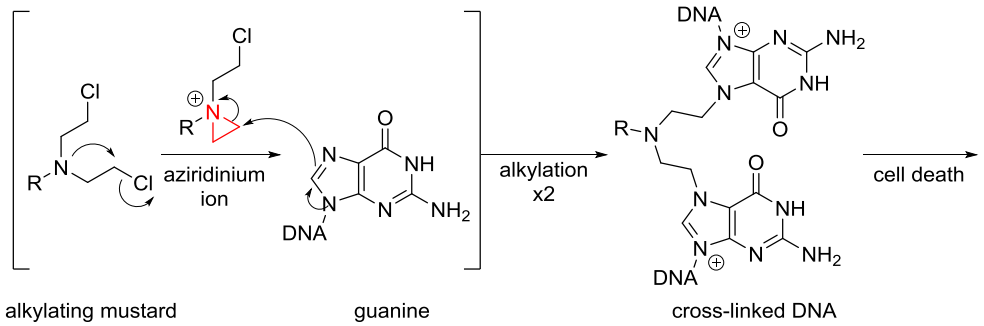

Figure 1.2. (a) Structures of FDA-approved DNA-alkylators. (b) Mechanism of DNA alkylation by nitrogen mustards.

Anti-metabolites like 5-fluorouracil (5-FU), cytarabine, gemcitabine and methotrexate (Figure 1.3) compete with endogenous metabolites during genetic replication cycles. These agents are close structural analogues of nucleosides or vitamins, where small changes have been introduced to ablate their function whilst maintaining their binding to endogenous targets. 5-Fluorouracil is an unnatural analogue of uracil, a nucleobase found in RNA and used in the synthesis of thymine for incorporation into DNA. Metabolites of 5-FU are misincorporated into RNA resulting in a general loss of cellular protein function.[31] 5-Fluorouracil is also a 'suicide inhibitor' of thymidylate synthase.[31,32] The drug is a mainstay of many treatment protocols for head and neck cancers, lymphomas, skin cancers and gastrointestinal tumours.[33] Cytarabine is a

nucleoside mimic that contains a modified arabinose sugar (a stereoisomer of deoxyribose) conjugated to cytosine. It is misincorporated into DNA and causes cell cycle seizure and DNA polymerase inhibition.[34,35]

Methotrexate functions by blocking the activity of dihydrofolate reductase, thus inhibiting production of folic acid (vitamin B9), which is required for DNA and RNA synthesis.[36] Methotrexate is used in a wide variety of indications, including lung and breast cancers and advanced non-Hodgkin's lymphoma.[17] A more recent anti-metabolite, gemcitabine, has become an important addition to chemotherapy. This drug is an analogue of deoxycytidine, where the 2'-position of the deoxyribose has been difluorinated. The compound is misincorporated into DNA and causes apoptosis, although like many anti-metabolites, other targets are affected, e.g. ribonucleotide reductase. [37–40] Unlike other anti-metabolites, however, gemcitabine is effective against solid tumours and is used as a first-line treatment for pancreatic adenocarcinoma. It is also used in combination with other agents for advanced or metastatic non-small cell lung carcinomas and bladder cancer.[41–43]

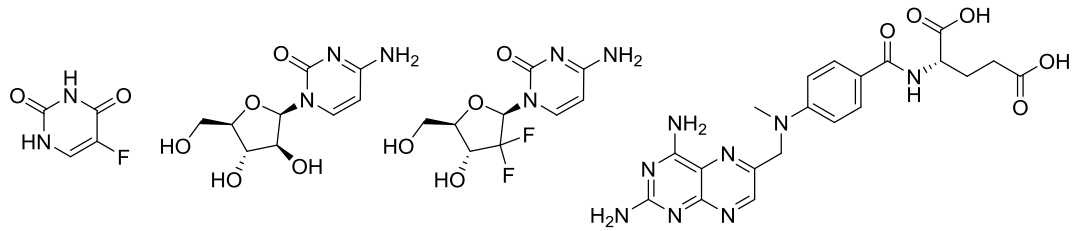

Figure 1.3. Structures of FDA-approved anti-metabolites.

DNA intercalators are planar, aromatic compounds that insert into double-stranded DNA, distorting the tertiary structure and promoting apoptosis (Figure 1.4).[44] These distorted complexes are stabilised by polar interactions with the phosphate backbone.[44] While many DNA-intercalators are limited to use as reagents and probes in biology due

to their toxicity and mutagenicity, doxorubicin continues to be used as a frontline treatment for many cancer types.[45]

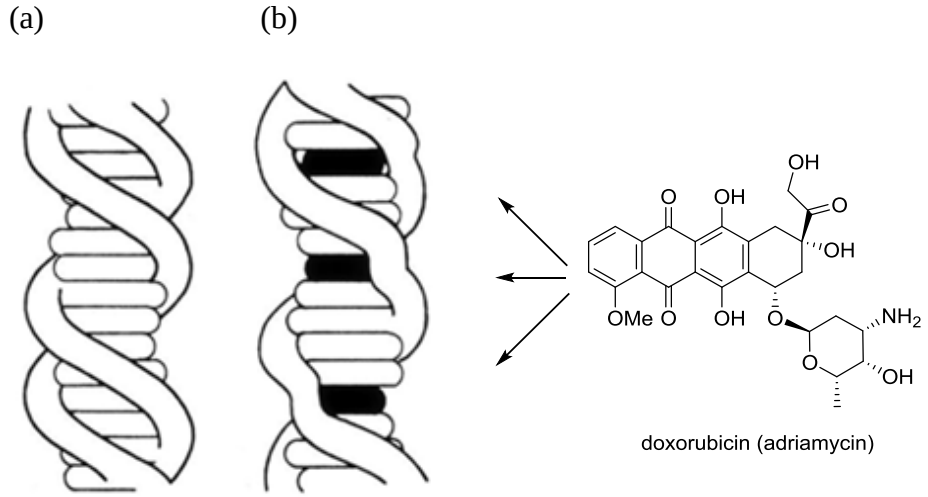

Figure 1.4. Insertion of DNA-intercalators like doxorubicin into double-stranded DNA (i.e. intercalation) distorts DNA tertiary structure.[44,46] (a) Normal double-helical and (b) distorted DNA structure with intercalated doxorubicin.

Paclitaxel and vinblastine are examples of anti-mitotic agents, which target cell division rather than DNA replication.[47] Specifically, anti-mitotic agents impair the function of tubulin, a key protein constituent of the microtubules required for physical budding and division of cells.[47,48] Paclitaxel binding to microtubules leads to their structural stabilisation, preventing disassembly and separation. Vinca alkaloids like vinblastine, on the other hand, inhibit tubulin polymerisation (Figure 1.5).[49,50] Paclitaxel was the first 'blockbuster' oncology drug and continues to be used in ovarian, breast and non-small cell lung cancers, along with several other indications.[51] Vinca alkaloids continue to be widely used for childhood and adult acute lymphocytic leukemias, Hodgkin and non-Hodgkin lymphomas, Wilms tumor, Ewing sarcoma, neuroblastoma and rhabdomyosarcoma.[52]

(a)

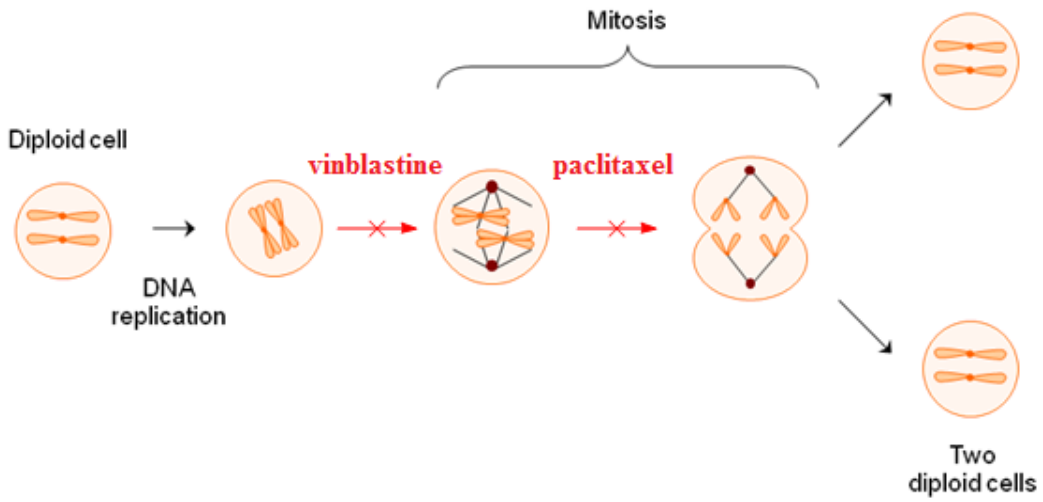

(b)

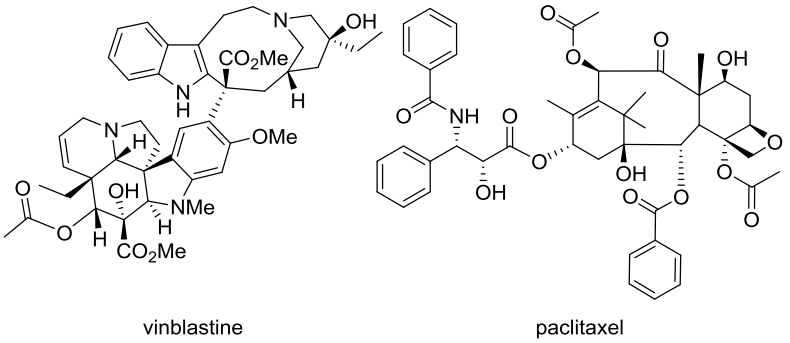

Figure 1.5. (a) Anti-mitotic agents vinblastine and paclitaxel inhibit cell division by targeting tubulin. (b) Structures of vinblastine and paclitaxel.

Drugs targeting DNA-replication and cell-division can affect healthy cells leading to unpleasant side effects. Rapidly dividing cells tend to be the worst affected, including hair follicles (leading to alopecia), blood and immune cells (anaemia, fatigue and immunosuppression) and gastrointestinal cells (nausea, vomiting and diarrhoea).[28,44,53,54] Other side effects commonly experienced with cytotoxins are neutropenia and skin rashes. While the side effects can be somewhat mitigated with other drugs, toxicity to organs (particularly the kidneys and liver) is dose-limiting and often severe. It is well established that many cancers are also resistant to these types of drugs when used alone.

In the past two decades there has been a push to develop more selective agents that target the underlying molecular mechanisms of uncontrolled proliferation in cancer rather than directly targeting replication and cell division.

1.5 Targets for Non-Cytotoxic Chemotherapy

1.5.1 Apoptosis

Millions of mutations occur daily in healthy human DNA due to the sheer volume of replication and mutation rates are increased by various risk factors. Nucleotides can be added, removed or mis-matched during DNA polymerisation, while mutagenic chemicals, UV or ionising radiation and oxidative stress can contribute to base modification, bonding between bases, cross-linkage or other DNA lesions.[55,56]

Several protective mechanisms exist in cells to detect mutations, repair the damage, control cells that contain the mutations and signal apoptosis, where necessary. Genes that code proteins involved in these processes are called tumour-suppressor genes. One key example is p53. The p53 protein is a nuclear transcription factor that responds to DNA damage by influencing cell cycle regulation, DNA repair, apoptosis and cell homeostasis.[57] Mutations or deletions in p53 are found in over 50% of all human tumours.[58] Unfortunately, the complexity of p53's actions and its function as a nuclear transcription factor make it a difficult drug target.[59,60] Efforts to replace dysfunctional p53 in tumour cells using gene therapy techniques have shown considerable promise and there is now an approved adenovirus vector in China (Gendicine).[61] Advexin is a similar vector in Phase III clinical trials in the USA.[62]

1.5.2 Internal Cell Division Limits

All chromosomes are terminated by telomeres; endcaps of repeating DNA sequences that serve to protect the DNA. Telomeres contain a guanine-rich overhang that promotes formation of a protein complex called shelterin. This complex prevents inappropriate cellular processing and chromosomal fusion.[63,64] During DNA replication, a portion of genetic material is lost from the telomere and, as this process repeats, the telomeres continue to shorten, eventually affecting genetic coding sequences.[65] Without telomeres, chromosomal fusion can also occur leading to apoptosis.[65] Telomere shortening limits the number of times a diploid cell can divide (the 'Hayflick limit'), which suppresses cell line immortalisation and excessive proliferation.[66] The ribonucleoprotein reverse transcriptase enzyme telomerase (transcribed from the hTERT gene) functions to maintain the protective endcaps in immortal stem cells.[65] Telomerase activation is central to the survival and proliferation of cancer cells. Over 90% of cancers express telomerase and its function is suspected to be replicated by alternate pathways in the remainder. [67,68]

Telomerase is currently being explored as a new drug target for cancer.[69] Drugs in clinical development include inhibitors of its reverse transcriptase activity,[70,71] small molecule or siRNAs that target the RNA template component hTR[72,73] and G-quadruplex-stabilising ligands.[74]

1.5.3 Invasiveness

An increase in invasiveness and motility is typically observed during later stages of tumour maturation.[5] To grow and eventually metastasise, a tumour needs to be able to degrade its surrounding extracellular matrix, enter a nearby blood vessel and extravasate

into a distant tissue.[75] Tumours can use a number of different chemical and enzymatic processes to achieve this. One hallmark of advanced tumours is that they switch from oxidative phosphorylation for energy production to glycolysis, even when the supply of oxygen is not limited (known as the Warburg effect – Figure 1.6).[76] This process consumes high levels of glucose and produces increased lactic acid, which is expelled into the extracellular matrix.[77,78] The associated decrease in *p*H can promote extracellular protease activity and matrix degradation.[79] Lactate production and transport are considered possible drug targets for reducing invasiveness.[78,80]

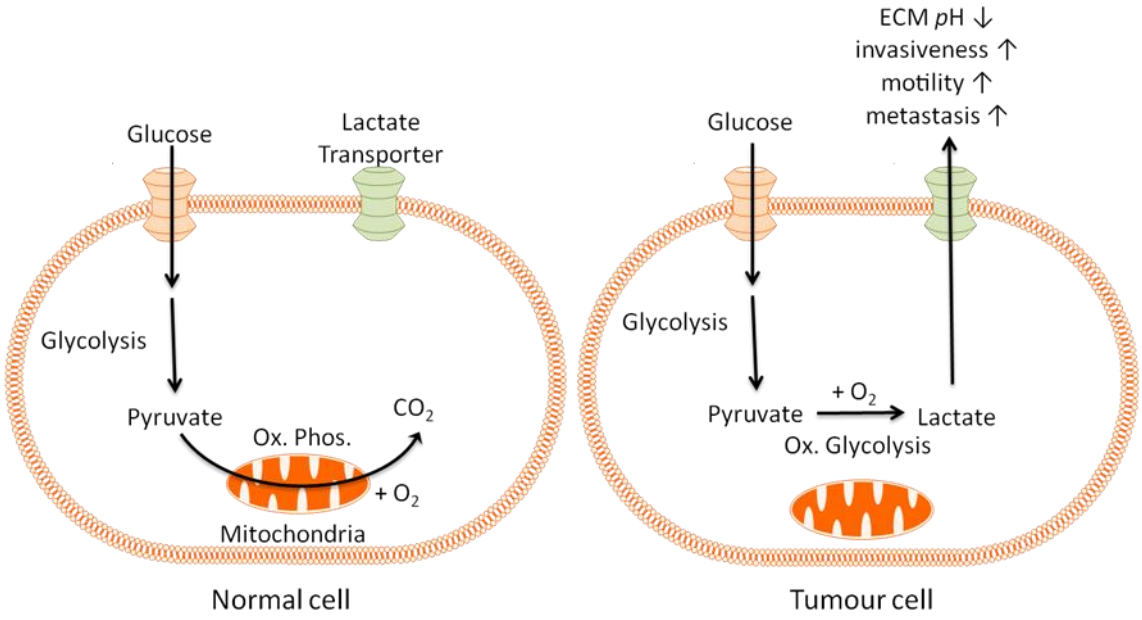

Figure 1.6. The 'Warburg effect' in tumour cells. Oxidative glycolysis is promoted in tumour cells even with a normal oxygen supply, increasing production (and efflux) of lactate. The resulting low extracellular *p*H promotes invasiveness, motility and metastasis.[77,78]

Tumours can also directly promote pro-metastatic enzymatic activity. For example, the broad spectrum serine protease plasmin, which is important in tissue breakdown and clotting, has been shown to be upregulated in metastatic tumours.[81] Other commonly

upregulated proteolytic enzymes include matrix metalloproteinases, cathepsins and the urokinase plasminogen activator (uPa), which are all involved in various stages of detachment and motility pathways.[81–84] Inhibitors of MMPs have generally been disappointing in clinical trials, a feature attributed to the complexity and redundancy of extracellular proteolytic signalling.[85] The uPA system has shown promise as an anti-metastasis target, with an orally bioavailable uPA inhibitor WX-671 currently in 8 different clinical trials.[86,87]

1.5.4 Growth Signalling

Cell proliferation and differentiation in healthy tissues is promoted by cytokines, growth factors and hormones. These signalling molecules affect cells by modulating intracellular reaction cascades. Growth factors promote growth and differentiation and their activity is controlled by endogenous inhibitors and transcription factors. Cancer cells can co-opt growth factor signalling through direct or upstream mutations, leading to constitutive expression and uncontrolled growth.[88] In recent times, targeted cancer drugs have focused sharply on intercepting growth factors and hormones that activate receptor tyrosine kinases (RTKs). These enzymes catalyse the transfer of phosphate groups from ATP to downstream proteins, affecting cell growth, proliferation and cell survival in response to extracellular signals.[89]

The epidermal growth factor (EGF) family of receptors plays a role in the normal growth and development of various tissues[90] and it has been estimated that 50-70% of lung, colon and breast carcinomas (the most common solid tumours) overexpress EGF receptors (e.g. EGFR or ErbB-3).[90] Several RTK inhibitors that block EGFR function have been developed as anti-cancer drugs.[22] These include the small molecules gefitinib

and erlotinib and the monoclonal antibodies (mAbs) cetuximab and panitumumab (Figure 1.7).[91]

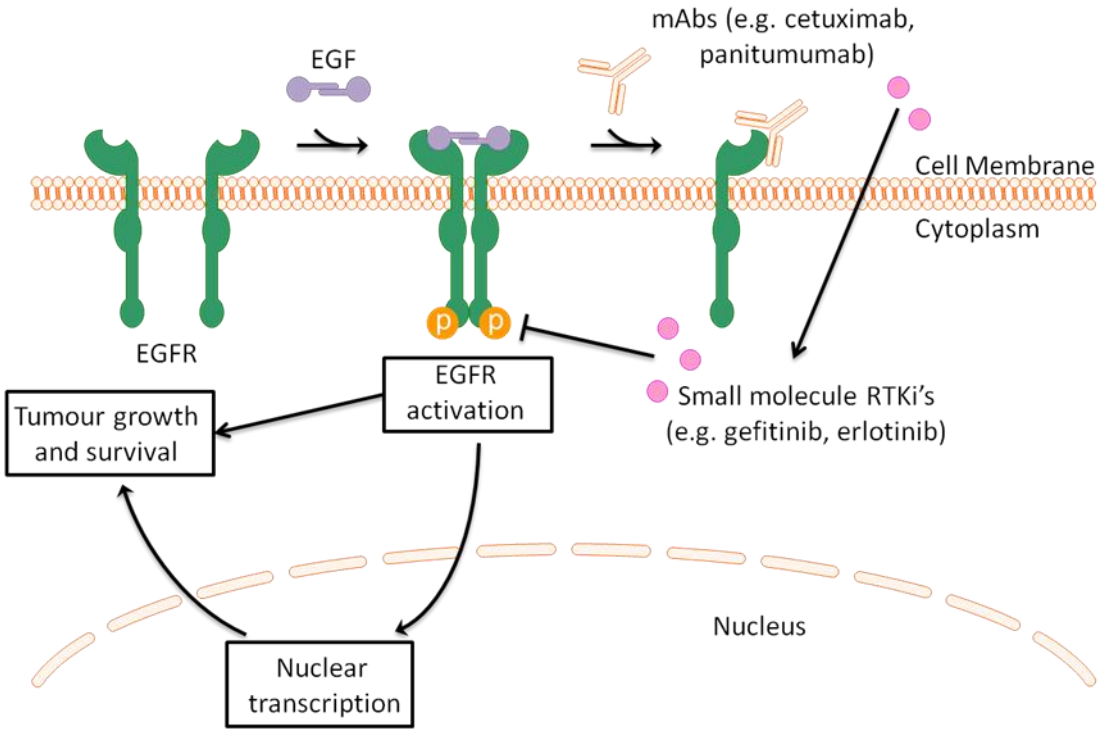

Figure 1.7. Inhibition of EGFR signalling pathways with small molecule RTK inhibitors and mAbs. EGF = epidermal growth factor, EGFR = epidermal growth factor receptor, RTKi = receptor tyrosine kinase inhibitor, mAb = monoclonal antibody.

Another tumour-promoting growth factor is transforming growth factor-β (TGF-β). TGF-β regulates proliferation and differentiation of cells, embryonic development, wound healing and angiogenesis by acting on epithelial, endothelial and haematopoietic cells.[92] Cell motility and invasiveness is enhanced by TGF-β.[92] Mutations causing resistance to TGF-β are observed in over 85% of epithelium-derived human cancers.[93] In these cases, TGF-β primes the surrounding matrix and promotes invasiveness of TGF-β insensitive cancer cells.[93] TGF-β also affects expression of hTERT promoting cell immortality.[94]

While growth factors control the progression of most cancers, some tissues are susceptible to highly aggressive tumours because of tissue-specific hormones. Blocking these hormones can greatly improve efficacy of treatments for sub-types of gonadial, prostate and breast cancers. Trastuzumab (Herceptin) is a monoclonal antibody used in breast cancer that targets HER2, an EGF RTK that promotes cell proliferation.[91,95] Lapatinib is a small-molecule dual HER2/EGFR inhibitor that is used to treat "triple positive" breast cancers.[96] Tamoxifen is a particularly effective small molecule oestrogen receptor antagonist that is used as an adjuvant to surgery when treating oestrogen-dependent breast cancers.[11,97] Early and late-stage prostate cancers are often treated with bicalutamide (Casodex), which antagonises the nuclear androgen receptor (AR).[98] Figure 1.8 shows the structures for these hormone receptor-targeting agents.

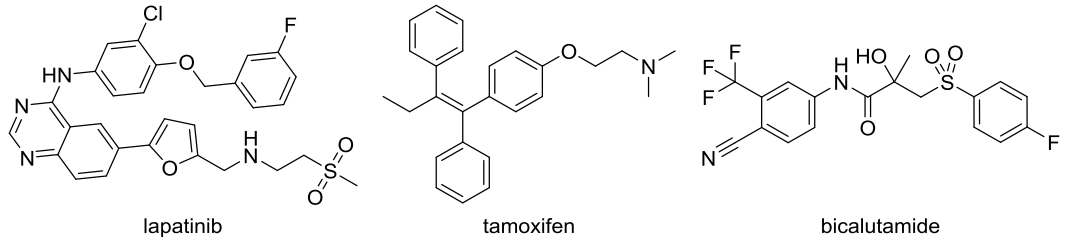

Figure 1.8. Examples of hormone receptor-targeting anti-cancer drugs.

1.5.5 Angiogenesis

Angiogenesis is the growth of new blood vessels from pre-existing vasculature. It is a complex process and is carefully regulated in healthy tissues by families of growth factors and their corresponding nuclear, cytosolic and membrane-bound receptors.[99–101] As localised tumours grow, sections of the tumour become hypoxic (i.e. low oxygen concentration) because of the increased distance of cells from blood vessels due to the aberrant vasculature and their increased metabolic needs (Figure 1.9).[102] Hypoxia is correlated with poor drug uptake and resistance to radiotherapy (due to lower

production of reactive oxygen species) and is considered a marker of poor prognosis.[103–105] Tumours respond to hypoxia by entering latent phases, modifying their metabolism and by promoting angiogenesis; a hallmark of advanced solid tumours.[5,106,107]

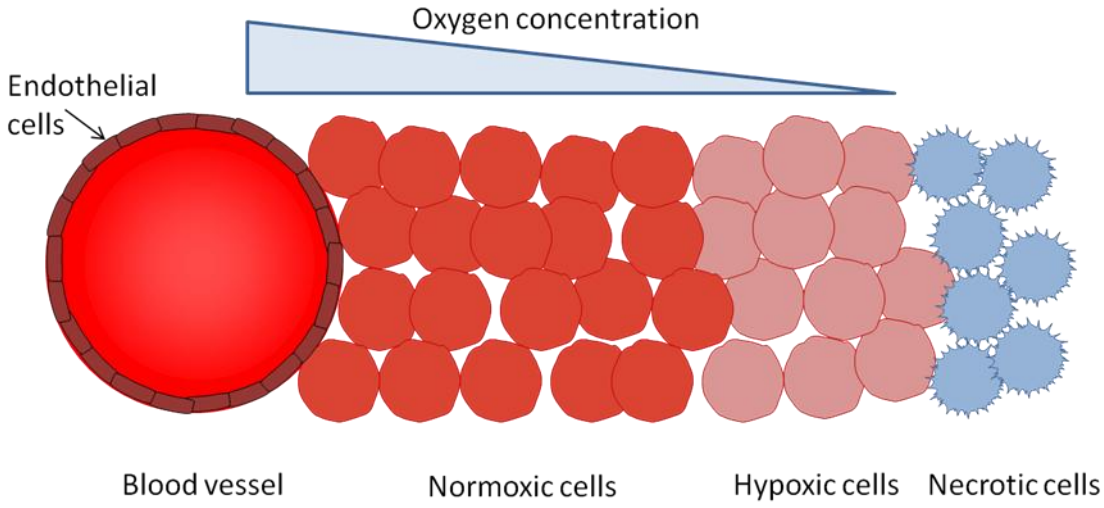

Figure 1.9. Hypoxic and necrotic cells arise in solid tumours due to their increased distance from the nearest blood vessels.[108]

A major pro-angiogenic response to hypoxia is initiated by hypoxia-inducible factor-1 (HIF-1). HIF-1 is a nuclear signalling protein that binds to hypoxia responsive elements on DNA in response to hypoxia, increasing transcription of proteins that restore normal oxygen supply.[107,109] HIF-1 is a heterodimeric protein consisting of two subunits; oxygen-sensitive HIF-1α and constitutively expressed HIF-1β.[110] When oxygen is present, cytosolic HIF-1α is hydroxylated and ubiquitinated by the von Hippel-Lindau tumour suppressor protein and targeted to the proteasome for removal.[111] When a cell becomes hypoxic, the hydroxylation process is slowed and dimerisation of HIF-1αβ occurs, resulting in signal activation.[112]

HIF-1 is often overexpressed in human cancers and its expression is correlated with poor prognosis.[103,104,113,114] Drugs that target several aspects of HIF-1 activity have been

developed.[115] For example, some drugs bind to targets in the phosphatidylinositol 3-kinase (PI3K), mammalian target of rapamycin (mTOR) and extracellular-signal-related mitogen-activated protein kinase (MAPK) pathways, reducing the transcription of HIF-1α mRNA.[116–119] Several drugs that inhibit mTOR have been approved, including the rapamycin derivative Temsirolimus (Figure 1.10), which is used for renal cell carcinomas and other advanced tumours.[120,121]

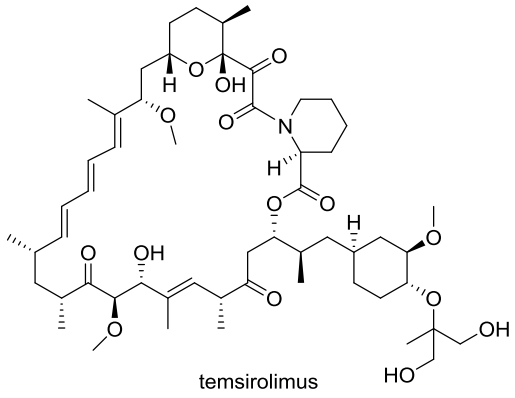

Figure 1.10. Temsirolimus targets mTOR to reduce transcription of HIF-1α.

Important downstream pro-angiogenic signalling proteins include platelet-derived growth factors (PDGFs), vascular endothelial growth factors (VEGFs) and epidermal growth factors (EGFs).[122,123] These RTKs activate a wide variety of downstream targets that promote angiogenesis, cell motility, differentiation, matrix degradation and survival.[91,124] Transcription of these proteins is often upregulated in cancers and their function is poorly controlled, leading to formation of a disorganised, highly permeable vasculature (tumour-associated vasculature, TAV).[99,100,107,124-126]

Two main strategies have been developed to target these processes: (1) sequestration of the signalling proteins using mAbs and (2) inhibition of RTKs using small molecules (Figure 1.11).[123,126,127] Bevacizumab (Avastin®) is a monoclonal antibody that binds to VEGF-A triggering its removal by immune cells. The drug was approved for colorectal

cancer in 2004 and was the first FDA-approved angiogenesis inhibitor.[128] It has since been approved for a variety of advanced lung, renal, ovarian and brain tumours.[128] Imatinib (Gleevec®, Figure 1.12) is a small molecule RTK inhibitor that shows high specificity for the bcr-abl RTK (also known as the "Philadelphia chromosome" or Ph+), a constitutively "on" mutant RTK found in 95% of chronic myelogenous leukaemia (CML) patients.[129] It has since been approved for gastrointestinal stromal tumours and several mutant kinase-related leukaemias.[130] A related analogue dasatinib (Sprycel®) is approved as a first line treatment for CML and Ph+ acute lymphoblastic leukaemia.[131]

Sunitinib (Sutent®) is an FDA-approved angiogenesis inhibitor that was originally indicated for use in imatinib-resistant gastrointestinal stromal tumours.[132] The compound is a multi-target RTK inhibitor that binds to several related PDGF family receptors.[133] Sunitinib was developed in favour of its predecessor semaxinib (SU5416), a VEGFR-2 selective RTK inhibitor that reached Phase II clinical trials.[134] Sunitinib shows a broader inhibition profile across RTKs than SU5416, which is attributed to the F-substituent at the 5-position of the oxindole moiety. A hydrophilic *N*,*N*-diethylethylenediamine carboxamide moiety at the 3-position of the pyrrole improved the compound's ADMET properties. Sunitinib later received approval as a first-line therapy in advanced renal cell carcinoma and against metastatic or unresectable pancreatic neuroendocrine tumours.[135] Both sunitinib and semaxinib are compounds of direct relevance in this PhD project (see later).

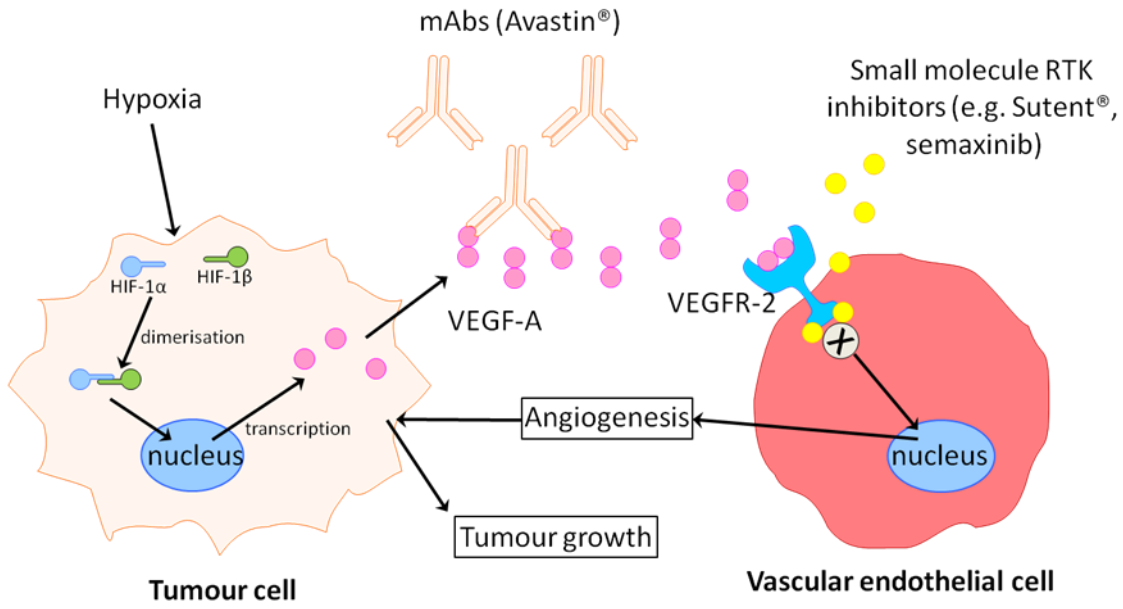

Figure 1.11. Inhibition of angiogenesis and tumour growth by VEGF-A-targeting mAbs and small molecule RTK inhibitors.

Other angiogenesis inhibitors approved for use in cancer include sorafenib (Nexavar®) and erlotinib (Tarceva®), which show similar RTK selectivity profiles to sunitinib. Another drug pazopanib (Votrient®) targets EGFR selectively (Figure 1.12).[127] These targeted RTK inhibitors are often used in combination with traditional cytotoxic drugs as they show mostly cytostatic action.[136] Compared to traditional cytotoxins, however angiogenesis inhibitors tend to be well-tolerated, although it is clear that they are not the 'magic bullets' as originally hoped.[137]

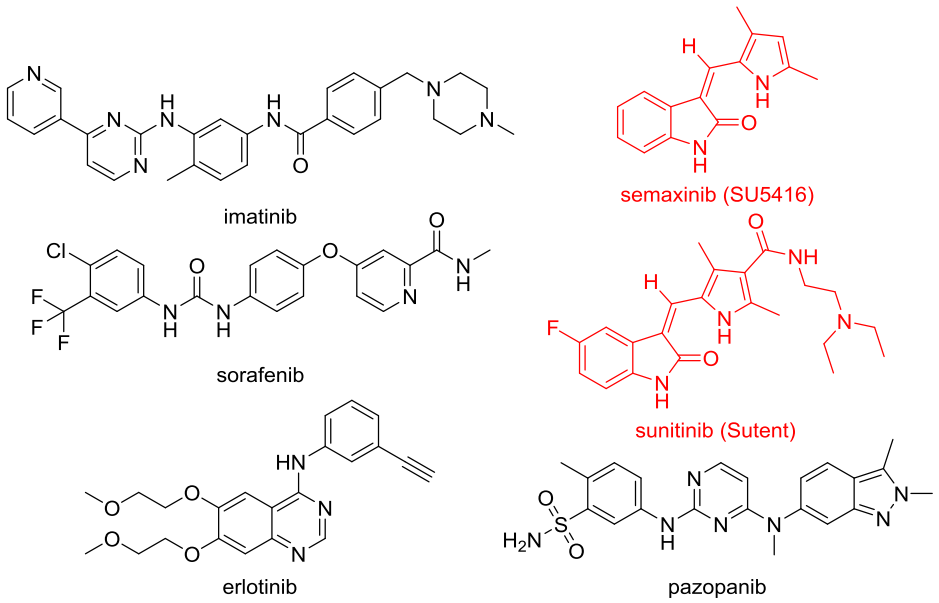

Figure 1.12. Small molecule RTK angiogenesis inhibitors approved for use in cancer treatment. Semaxinib and Sutent (sunitinib) are compounds relevant to the PhD project (red).

1.6 Anti-Cancer Prodrugs

1.6.1 Prodrugs - General

Prodrugs are biologically inert or only weakly active compounds that are modified to active forms by metabolic reactions *in vivo*. Prodrug forms have been investigated for many cytotoxic agents as a means of improving their efficacy and safety profiles.[138,139] Masking the cytotoxic moieties can improve bioavailability, reduce systemic toxicity and modulate first-pass metabolism and plasma half-life. Prodrugs of anti-cancer agents often aim to reduce the gastrointestinal toxicity of their active components and improve selectivity for tumours over healthy tissues.[139,140]

Examples of approved anti-cancer prodrugs are capecitabine and tegafur; both prodrugs of 5-fluorouracil (5-FU).[138] Capecitabine is a hydrophobic carbamate derivative of 5-fluoro-2'-deoxyuridine and is used for treating metastatic colorectal and breast

cancers.[141] Tegafur is a tetrahydrofuran-linked aminal derivative of 5-fluorouracil used primarily in the treatment of gastric and colorectal cancers.[142] Capecitabine and tegafur are enzymatically converted *in vivo* to 5-fluorouridine, the activate metabolite of 5-FU (Figure 1.13). The prodrugs reduce gastrointestinal toxicity and show improved oral bioavailability over the parent 5-FU.[138,141,142] Cyclophosphamide is an inert prodrug activated by a mixed function microsomal oxidase system in the liver to produce multiple active forms, many of which are DNA-alkylators.[143] It is used to treat several leukaemias, lymphomas and brain cancers.[144]

(a)

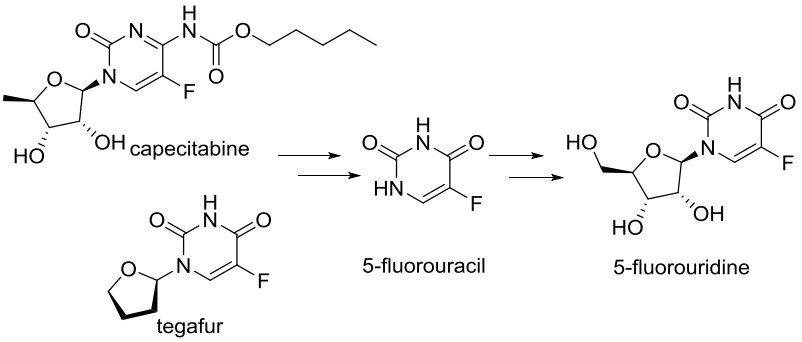

(b)

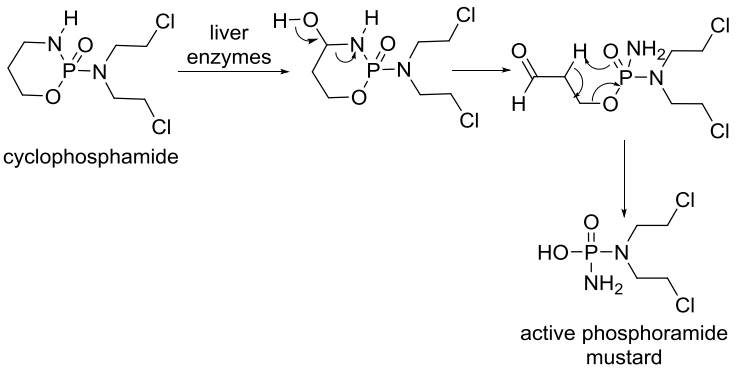

Figure 1.13. (a) Capecitabine and tegafur are FDA-approved prodrug forms of 5-FU that generate the active metabolite 5-fluorouridine *in vivo*. (b) Mechanism of activation of cyclophosphamide *in vivo*.

1.6.2 Tumour-Targeted Prodrugs

Tumour-targeted prodrugs are designed to make use of a variety of activation processes unique to or introduced into cancers. These prodrugs reduce the side effects of highly toxic agents by localised activation in the immediate tumour environment.[145,146] Two major classes of tumour-targeted prodrugs are antibody-drug conjugates and hypoxia-activated prodrugs.

1.6.2.1 Antibody-Drug Conjugates

Antibody-drug conjugates are biologics that use selective recognition of tumour-associated antigens and receptors to deliver an extremely potent cytotoxin selectively to tumours.[147,148] This approach uses the exquisite selectivity of monoclonal antibodies (mAbs) to provide highly specific cancer cell killing. The mAbs are typically linked via a plasma-stable, enzyme-cleavable tether and chemical spacer to the cytotoxin. The conjugates are localised to tumours through antigen recognition and, following internalisation, are cleaved by intracellular enzymes, e.g. cathepsins (Figure 1.14).[149] Fewer than 10 cytotoxin molecules are usually linked to the mAbs to maintain avidity, thus necessitating the use of extremely potent toxins.[148–150]

Two FDA-approved examples are brentuximab-vedotin (Adcetris®) and trastuzumab-emtansine (Kadcyla®).[151] Brentuximab targets CD30, a membrane protein associated with tumour necrosis factor (TNF) signal transduction that is expressed on active T- and B-cells in malignant lymphomas.[152,153] The vedotin portion of the conjugate is comprised of the potent cytotoxin monomethyl auristatin E (MMAE), a *p*-aminobenzoic acid spacer and a cathepsin-cleavable citrulline-valine linker.[151] MMAE is a tubulin polymerisation inhibitor that is 200 times more potent than vinblastine.[154] Brentuximab-

vedotin was approved in 2011 for use in relapsed or refractory Hodgkin's lymphoma and systemic anaplastic large cell lymphomas.[155]

Trastuzumab-emtansine combines trastuzumab's avidity for HER2 with mertansine, a maytansine alkaloid that inhibits microtubule assembly at subnanomolar concentrations.[150,156] These two agents are linked with a succinimidyl-*trans*-4-(maleimidylmethyl)cyclohexane-1-carboxylate moiety. Trastuzumab-emtansine was approved in 2013 for use in HER2+ breast cancers that have progressed following standard treatments.[157] Many other antibody-drug conjugates are likely to enter the clinic as new mAbs, linking strategies and cytotoxins are being discovered.[148,149]

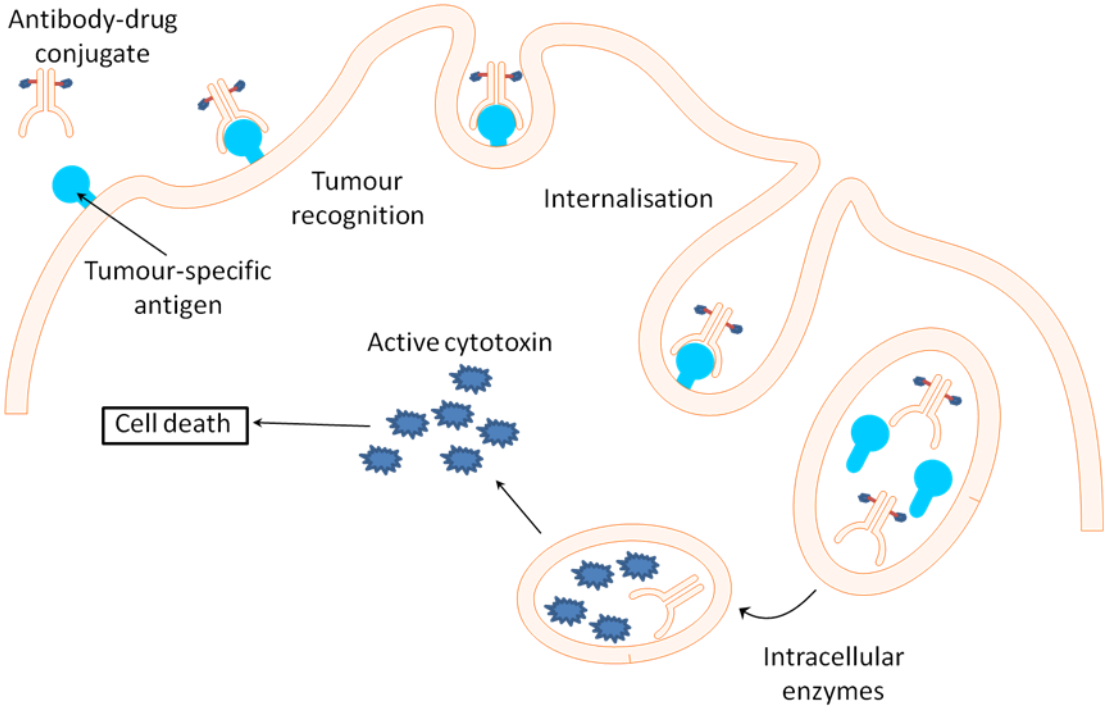

Figure 1.14. Cell killing mechanism of tumour-targeted antibody-drug conjugates.

1.6.2.2 Hypoxia-Activated Prodrugs

Another approach for targeting prodrugs to tumours is to invoke hypoxia-activation. As described earlier, when hypoxia develops in normal healthy tissues HIF-1 signalling

triggers angiogenesis and other cellular mechanisms to restore oxygen levels.[107,158–161] In comparison, virtually all solid tumours over 1 mm^3 contain regions that are at least transiently hypoxic.[102,103,162–164] Many tumours remain viable in spite of hypoxia due to a variety of survival and growth factors, glycolytic enzymes and enzymes involved in invasiveness.[103,106,112,158]

The low concentration of oxygen and low *p*H in hypoxic tumour microenvironments can promote tumour-selective reduction reactions.[115] Several oxidative enzymes exist ubiquitously across tissues and are responsible for many aspects of catabolism, recycling of important species (e.g. nucleobases) and energy generation. Examples include xanthine oxidases, NADPH-cytochrome reductases, lipoxygenases, DT-diaphorase and cytochrome P450. Each of these enzymes catalyse redox reactions that use water and O_2 to oxidise organic substrates.[165–167] This process results in reduced oxygen products, including peroxide and other reactive oxygen species like superoxide, which can be further scavenged by enzymes such as superoxide dismutase and catalase to prevent damage to the cell.[168]

In hypoxic and anoxic tumour cells, oxygen is not present in sufficient quantities to counter the reduction reactions, meaning that when reduced species are formed they are susceptible to further reduction reactions. This tumour-specific feature can be exploited with prodrugs that are activated to produce cytotoxins only after multiple-electron reduction reactions.[108,169] Under normoxic conditions in healthy tissues, the initial reduction products are reversibly reoxidised by systems coupled to molecular oxygen. In hypoxic and anoxic cells in solid tumours, where molecular oxygen supply is limited, the initial reduction products are not back-oxidised and can undergo further reduction reactions to generate reactive species (Figure 1.15). As the process is restricted to

hypoxic tissues, unmasking of the active cytotoxin is localised to the immediate tumour vicinity, minimising its detrimental effects on normal tissues.

A number of requirements need to be met for a hypoxia-activated prodrug to be functional. Firstly, it should be inert in plasma and not be activated by hepatic cytochrome P450s as this can lead to unacceptable liver toxicity. It should accumulate in hypoxic tumours and undergo selective activation, with the active species then diffusing sufficiently to kill nearby normoxic tumour cells (i.e. 'bystander effect').[169]

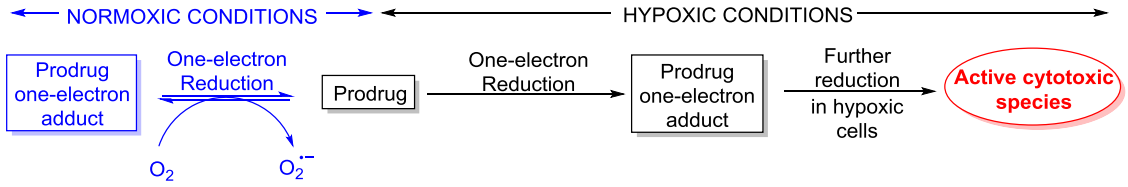

Figure 1.15. Mechanism of selective bioreductive activation of prodrugs in hypoxic tumours.[169]

The most studied class of hypoxia-activated prodrugs are the nitroaromatics.[169] These compounds use reduction of an aryl nitro group to an aryl hydroxylamine or amine moiety to trigger activation of a cytotoxin.[108] For example, cytotoxins such as nitrogen or phosphoramide mustards can be conjugated to nitro aromatic moieties to reduce their intrinsic reactivity towards DNA.[170,171] The strongly electron withdrawing nitro group reduces electron density and consequently nucleophilicity of the reactive functional group in the prodrug. When hydroxylamine or amine groups are revealed following bioreduction, these nucleophilic and/or electron donating groups trigger spontaneous reactions that lead to formation of a cytotoxin.

The first hypoxia-selective prodrug developed for use in cancer was misonidazole (Figure 1.16), a derivative of the anaerobic antibacterial agent metronidazole.[172]

Misonidazole was observed to accumulate in cancer cells after hypoxia-selective reduction, producing species that bind cellular nucleophiles at the 4- or 5-positions of the imidazole ring (Figure 1.16).[173] The compound was originally conceived as a radiosensitiser that could confer radiation sensitivity to hypoxic tumours.[174,175] Unfortunately, clinical evaluation of misonidazole in cancer did not show sufficient efficacy. Nevertheless, ^{18}F-labelled misonidazole has proven to be an effective PET agent for imaging hypoxia in tumours.[165]

TH-302 (evofosfamide) is a related prodrug that uses the nitro-imidazole scaffold as a hypoxia-selective trigger for release of a bromoisophosphoramide alkylating mustard (Figure 1.16).[167,171] It is currently being investigated in Phase III trials in combination with doxorubicin for use in soft-tissue sarcomas. A separate Phase III trial is investigating the compound against advanced pancreatic adenocarcinomas in combination with gemcitabine.[145]

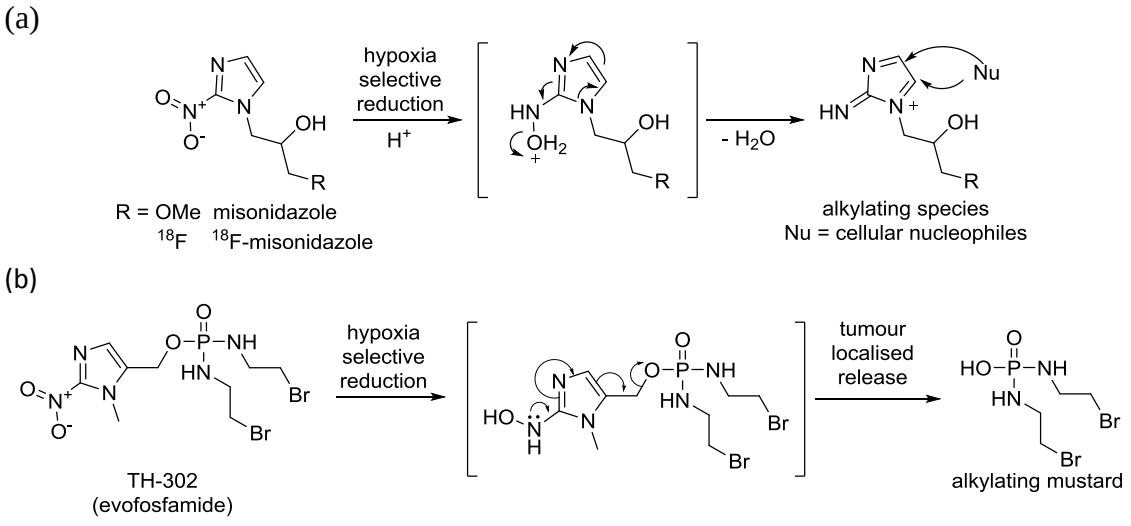

Figure 1.16. Hypoxia-selective activation mechanism of the nitroaromatic prodrugs (a) Misonidazole, and (b) TH-302 (evofosfamide).

In 1994, Denny et al. described nitroaromatic prodrug chemistry for hypoxia-selective activation of cytotoxins that utilise 2-nitrophenylacetic acid as the trigger.[176] An

electron-withdrawing amide bond *para* to a phenylenediamine mustard nitrogen served to reduce its nucleophilic character, preventing aziridinium ion formation and subsequent DNA alkylation. Upon reduction to the hydroxylamine or aniline, a spontaneous 5-membered intramolecular cyclisation occurred to release the active phenylenediamine nitrogen mustard (Figure 1.17). A molecule of oxindole (or *N*-hydroxyoxindole) was released from the prodrug as a waste fragment.

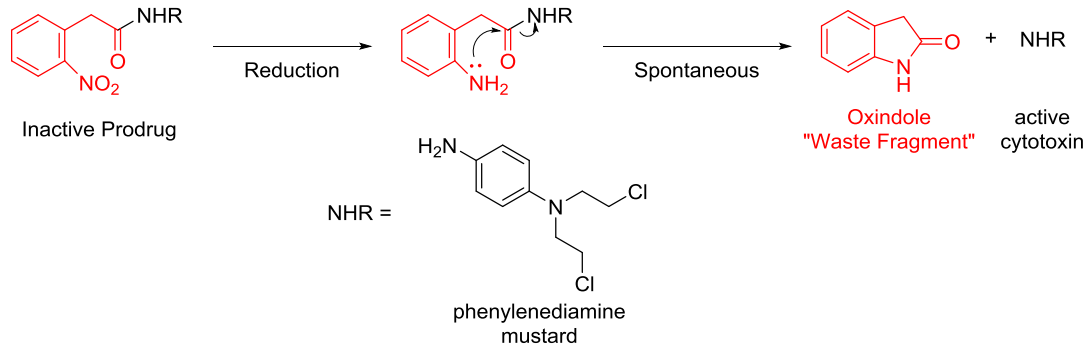

Figure 1.17. Hypoxia-activated 2-nitrophenylacetate-based prodrug chemistry described by Denny et al.[176]

Similar chemistry was later deployed with the angiogenesis inhibitor SU5416 (Figure 1.18), where the 2-nitrophenylacetate group was appended to the oxindole nitrogen of SU5416 to create a hypoxia-activated angiogenesis inhibitor prodrug.[177]

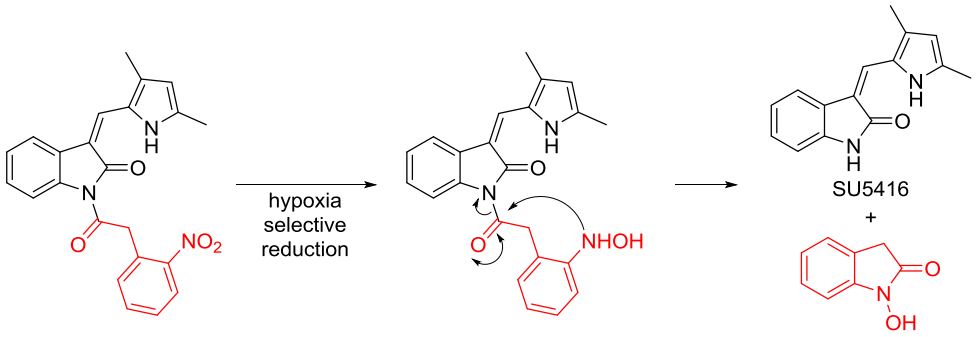

Figure 1.18. Hypoxia-triggered activation of a 2-nitrophenylacetate prodrug derivative of angiogenesis inhibitor SU5416.[177]

1.7 Mutual Prodrugs (Codrugs)

1.7.1 General

Mutual prodrugs (or codrugs) are compounds that combine two active agents into a single prodrug molecule. A number of codrugs are currently in development, as reviewed by Das et al.[178] Examples are being assessed for use in alcohol and tobacco withdrawal, ocular disorders, neurodegenerative disorders, HIV therapy, cardiovascular disease and as anti-cancer and antibacterial agents.[178]

Benorylate (Figure 1.19) is an FDA-approved codrug that combines paracetamol and aspirin via an ester linkage to produce a single, orally active dual-action analgesic.[179] Sulfasalazine is a codrug of the anti-inflammatory agent 5-aminosalicylic acid and the sulfa antibacterial sulfapyridine, which is used to treat rheumatoid arthritis and the inflammatory bowel disorder Crohn's disease.[180,181] The codrug links the two agents via an azo bond. Sultamicillin is an antibiotic codrug that links the two antibacterials ampicillin and sulbactam via an acetal-type linkage. The codrug form shows excellent absorption and decreased gastrointestinal side effects relative to the individual compounds.[182]

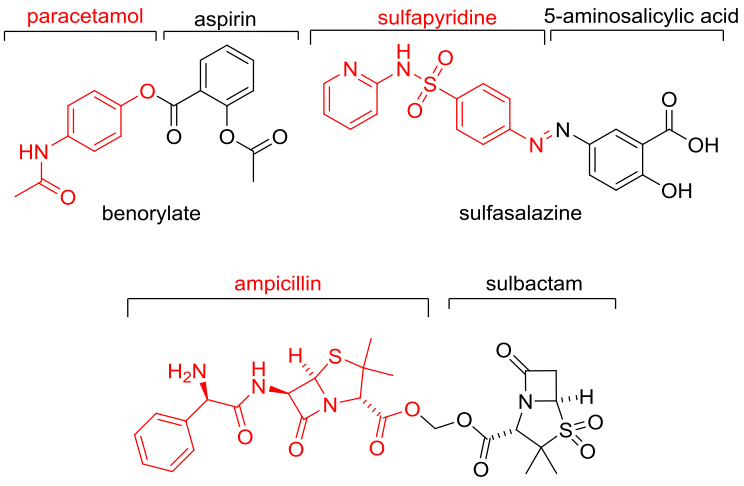

Figure 1.19. Structure of codrugs benorylate, sulfasalazine and sultamicillin.

1.7.2 Rational Design of a Hypoxia-Activated Anti-Tumour Codrug

Inspired by the 2-nitrophenylacetate prodrug chemistry described earlier, we conceived a codrug structure **1**, containing the components of angiogenesis inhibitor SU5416 and a phenylenediamine-based nitrogen mustard (Figure 1.20). In this codrug, the benzylic position of the 2-nitrophenylacetate triggering moiety is substituted by the alkenyl pyrrole portion of SU5416. Attachment of the phenylenediamine mustard via an amide bond should lower the nucleophilic character of the mustard nitrogen, thus preventing aziridinium ion formation and non-selective DNA alkylation. The phenylenediamine mustard proportion should also provide steric bulk that prevents angiogenesis inhibition by the SU5416-like portion (i.e. prevents binding to RTK targets). Hypoxia-selective bioreduction of the aryl nitro moiety to the aniline derivative should trigger a spontaneous 5-membered cyclisation that simultaneously releases the angiogenesis inhibitor SU5416 **2** (as opposed to an oxindole "waste" fragment, see Figure 1.20) and the phenylenediamine mustard. No longer deactivated by the amide bond, the *p*-amino group of the mustard would feed electron density onto the mustard nitrogen to increase its nucleophilicity and promote aziridinium ion formation and DNA alkylation.

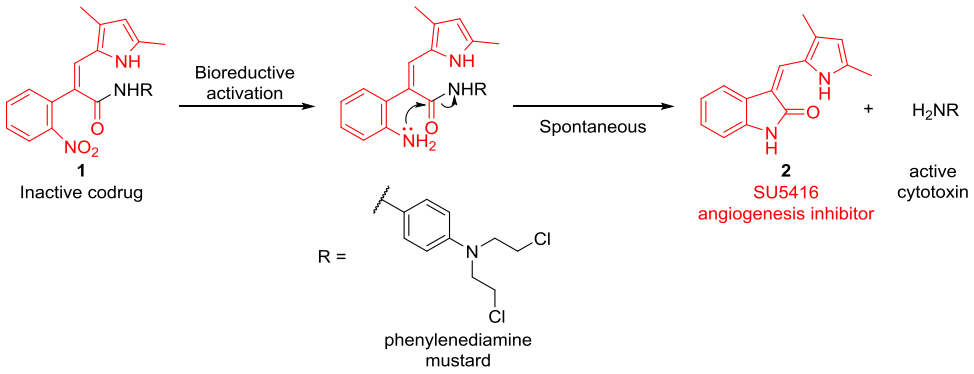

Figure 1.20. Putative hypoxia-selective activation mechanism of SU5416-phenylenediamine mustard codrug **1**.

The advantages of such an agent as an anticancer therapeutic are potentially striking. Due to tumour-selective activation of the codrug, the gastrointestinal and other toxicities of both the cytotoxin and angiogenesis inhibitor components could be mitigated, allowing for higher and more efficacious dosages, imitating combination therapy but without the associated side effects.

1.8 Thesis Aims

The central aim of the PhD thesis was to develop and optimise a synthetic route towards codrug **1** and demonstrate chemical proof-of-concept showing that chemical reduction of the NO_2 group leads to formation of SU5416 and release of the cytotoxin. As detailed in the following chapters, these aims were achieved and in the process several novel discoveries were made.

Chapter 2

Preliminary Synthetic and

Biological Studies

2.1 Retrosynthetic Analysis

The concept of a self-immolative codrug like **1** raised a number of questions about its chemical properties and synthesis. The compound is intended to be stable under physiological conditions and to become reactive *in vivo* after triggering. Several issues were envisioned around when and how to introduce the reactive phenylenediamine mustard during the synthesis. As outlined in Chapter 1.4, mustards function via intramolecular nucleophilic activation to form aziridinium ions, which alkylate DNA. Preventing aziridinium formation was considered essential for the stability and functioning of the prodrug and for personal safety during the synthesis. The presence of an amide group *para* to the mustard nitrogen was expected to suppress activation by reducing its nucleophilicity through electron withdrawal.[170]

Two synthetic routes were conceived towards **1** (Figure 2.1). The first (**Route 1**) involved an early stage Knoevenagel condensation between ethyl-2-(2-nitrophenyl) acetate **3** and pyrrole-2-carboxaldehyde **4** (or a protected derivative). Related condensation chemistry is used in the synthesis of SU5416 and sunitinib from oxindoles.[183,184] Ester hydrolysis would yield the key acid intermediate (*Z*)-**5**, which could be coupled to a suitably protected phenylenediamine mustard precursor **6** to produce amide **7**. Advancing **7** to **1** would proceed via alcohol deprotection and chlorination (**Route 1**, Figure 2.1(a)). Alternatively, the amide linkage could be installed earlier by coupling 2-nitrophenylacetic acid to the protected phenylenediamine mustard precursor **6** to afford advanced amide intermediate **8**. The alkene **7** would subsequently be generated using a Knoevenagel condensation with **8** and pyrrole **4** (or a protected derivative). Final alcohol deprotection and chlorination would deliver **1** (**Route 2**, Figure 2.1(b)).

Route 1 was the preferred strategy as it was potentially more general, allowing a multitude of anticancer cytotoxins to be easily appended to the late-stage acid intermediate (*Z*)-**5** via simple amide (or ester) couplings.

(a) **Route 1**

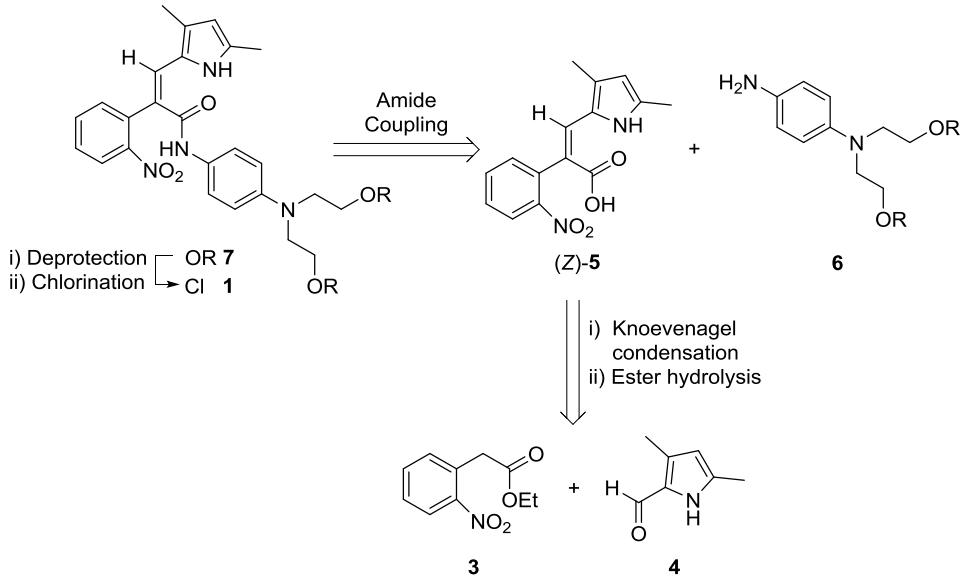

(b) **Route 2**

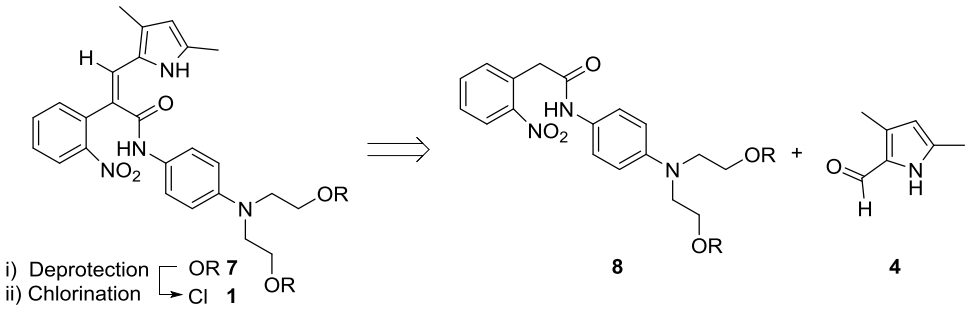

Figure 2.1. Retrosynthetic analysis for codrug **1**.

2.2 Discovery of a Novel Knoevenagel Condensation

Prior to commencing my PhD studies, preliminary synthetic explorations in the Kelso Lab had determined that a Knoevenagel condensation did not proceed directly between ethyl-2-(2-nitrophenyl) acetate **3** and unprotected 3,5-dimethyl-1*H*-pyrrole-2-carbaldehyde **4** under a variety of conditions. Failure of this reaction was attributed to low reactivity of the aldehyde in **4**. In order to increase electrophilicity of the aldehyde, the pyrrole nitrogen of **4** was protected with various electron withdrawing carbamates.

The ^{t}Bu, Et and Me carbamates of **4** were synthesised (by other students) from the requisite chloroformates and the potassium salt of **4** (generated via reaction of **4** with KH in THF at 0 ^{o}C) in good yields. The *N*-Me carbamate **9** (Scheme 2.1) proved to be effective in promoting the desired Knoevenagel condensation with ester **3**. Use of K_2CO_3 and 18-crown-6 as base in the presence of aldehyde **9** afforded the desired *cis* (*Z*)-**10** and *trans* (*E*)-**10** isomers in 46% and 30% yields, respectively (Scheme 2.1). Neither the Et nor ^{t}Bu-protected pyrroles afforded the alkenes under these conditions. The pyrrole *N*-carbamoyl group was fortuitously lost during the course of the reaction, meaning that the product did not require a separate *N*-deprotection step.

This preliminary finding suggested **Route 1** (Figure 2.1(a)) would be feasible, as ester hydrolysis of (*Z*)-**10** could provide the key carboxylic acid intermediate (*Z*)-**5**. The result suggested that an analogous Knoevenagel condensation using an amide instead of ester **3** might also be feasible, supporting exploration of **Route 2** (if needed).

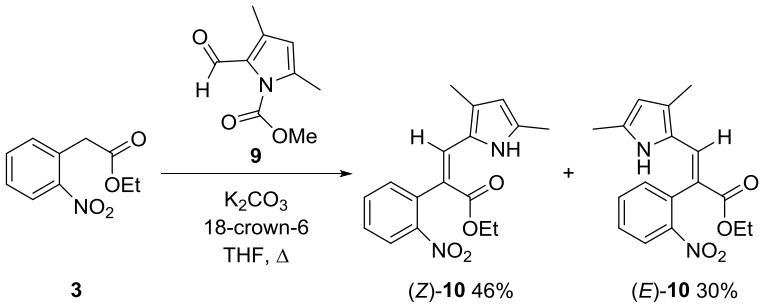

Scheme 2.1. Knoevenagel condensation developed earlier in the Kelso Lab.

Work by PhD student Pichit Sudta in the Kelso Lab showed that the carboxylic acid (*Z*)-**5** could be prepared using a 3-step sequence proceeding via allyl ester **12**. Previous efforts to produce (*Z*)-**5** via ester hydrolysis of (*Z*)-**10** (or the methyl ester) under acidic and basic conditions had failed, with only isomerisation between (*Z*)-**10** and (*E*)-**10** observed. Allyl ester **12** was formed in good yields by nucleophilic allylation of 2-

nitrophenylacetic acid **11** with allyl bromide and K_2CO_3 in acetone (74%), or via H_2SO_4-catalysed esterification of **11** with allyl alcohol (88%).

The newly discovered Knoevenagel condensation was found to work well between allyl ester **12**, providing *(Z)*-**13** and *(E)*-**13** in 41% and 33% yields, respectively. Deprotection of *(Z)*-**13** with 10 mol% $Pd(PPh_3)_4$ in the presence of morpholine (allyl cation scavenger) in THF provided (*Z*)-**5** in 84% yield, with no alkene isomerisation. An identical yield of (*E*)-**5** was obtained via deallylation of (*E*)-**12** under the same conditions.

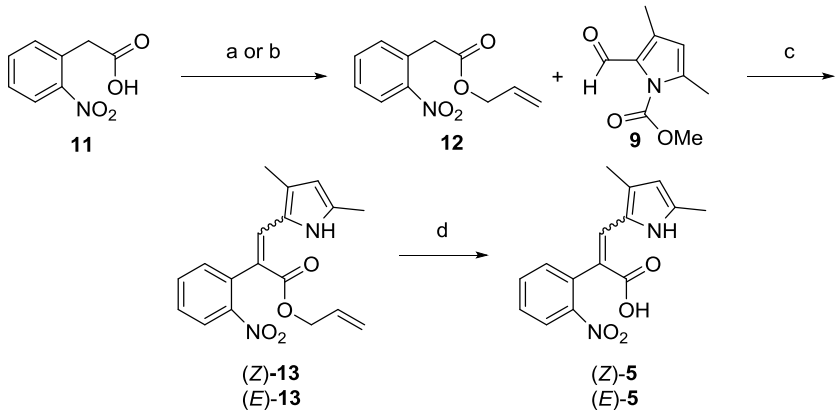

Scheme 2.2. Synthesis of key carboxylic acid intermediate (*Z*)-**5**. Reagents and conditions: a. K_2CO_3, allyl bromide, acetone, rt, 74%. b. allyl alcohol, cat. H_2SO_4, rt, 88%. c. **9** (1.0 mol eq.), K_2CO_3, 18-crown-6, THF, 65 ^oC, 14 h; (*Z*)-**13** 41%, (*E*)-**13** 33%. d. 10 mol% $Pd(PPh_3)_4$, morpholine, THF; (*Z*)-**5** 84% from (*Z*)-**13**, (*E*)-**5** 84% from (*E*)-**13**.

2.3 Conformation and Reactivity of Acid Intermediate 5

My attempts (during Honours) and attempts by other students in the Kelso Lab to perform alcohol and amine couplings with carboxylic acid intermediates (*Z*)-**5** and (*E*)-**5** all failed to give the desired *cis*- and *trans*-ester/amide products. The reactions instead produced the novel compound 5,7-dimethyl-2-(2-nitrophenyl)-3*H*-pyrrolizin-3-one) **14**,

arising through intramolecular cyclisation of the pyrrole nitrogen onto the activated carbonyl group (Figure 2.2(a)). It was suspected that cyclisation was being promoted by an intramolecular hydrogen bond between the pyrrole N-H of (*Z*)-**5** and the carbonyl oxygen. This H-bond could increase acidity of the pyrrole N-H and weaken the carbonyl C=O bond and stabilise the tetrahedral transition state leading to intramolecular ring closure under ester and amide coupling conditions.

As part of my PhD work, I repeated Pichit Sudta's synthesis of (*Z*)-**5** and was able to grow a crystal of the compound suitable for X-ray analysis. I also converted a sample of (*Z*)-**5** to 5,7-dimethyl-2-(2-nitrophenyl)-3*H*-pyrrolizin-3-one **14** and obtained a crystal of from Et_2O. The X-ray structure of **14** was solved by Tony Willis (ANU) and is shown in Figure 2.2(b). The structure showed that the 2-nitrophenyl ring was tilted 35.5^o relative to the plane of the 3*H*-pyrrolizin-3-one ring and that the NO_2 group was positioned close to the carbonyl oxygen. The distance between the carbonyl oxygen and the NO_2 nitrogen was 2.8 Å. This close proximity suggests a favourable interaction between the electronegative oxygen and electropositive NO_2 nitrogen.

(a)

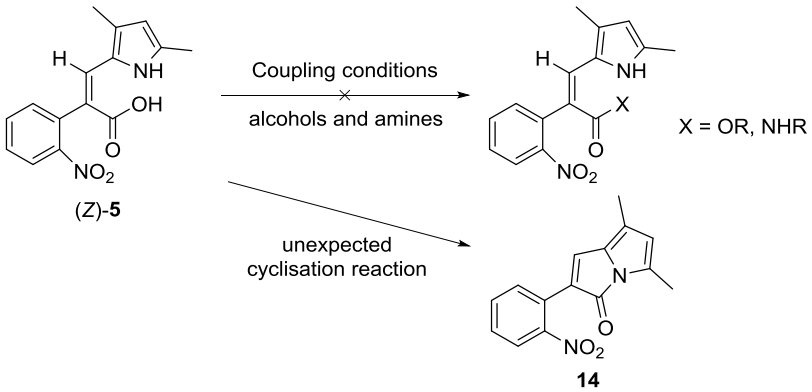

(b)

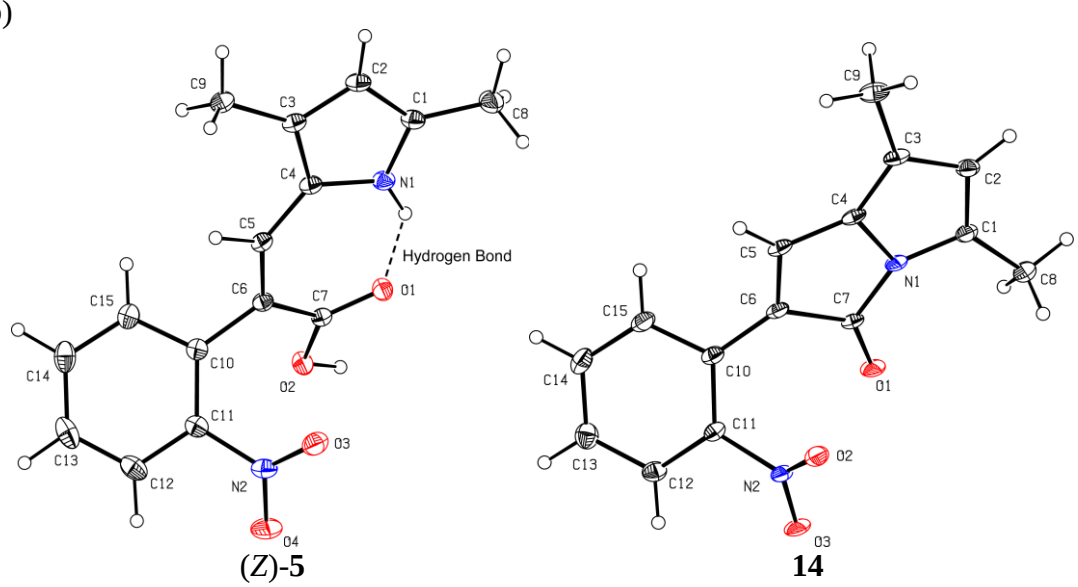

Figure 2.2. (a) Attempted syntheses of amide and ester derivatives of (*Z*)-**5** using standard coupling procedures resulted in formation of 3*H*-pyrrolizin-3-one **14** in good yields (70-88%). (b) X-ray crystal structures of (*Z*)-**5** and **14**. Anisotropic displacement ellipsoids show 30% probability levels. Hydrogen atoms are drawn as circles with small radii. Crystallographic data are provided in Chapter 6.1.1. Appendices 1(a) and 1(b).

The X-ray structure of (*Z*)-**5** confirmed the presence of the proposed H-bond stabilising a pseudo 7-membered ring. Evidence for the H-bond was also observed in the compound's ^{1}H NMR spectrum, where the pyrrole N-H signal for (*Z*)-**5** appeared far downfield at 11.87 ppm, whereas for (*E*)-**5** it was observed at 6.78 ppm (in $CDCl_3$). These characteristic chemical shifts were also observed in the ^{1}H NMR spectra of derivatives of **5**, as exemplified by allyl esters (*Z*)-**13** and (*E*)-**13**, where the pyrrole N-H appeared at 11.81 ppm and 6.75 ppm, respectively (Figure 2.3(a)). Single crystal X-ray structures of (*Z*)-**13** (previously obtained in the Kelso Lab) and *(E)*-**13** (obtained during my Honours) were solved by Tony Willis (ANU). These structures clearly showed the intramolecular H-bond was present in (*Z*)-**13** and absent in (*E*)-**13** (Figure 2.3(b)).

(a)

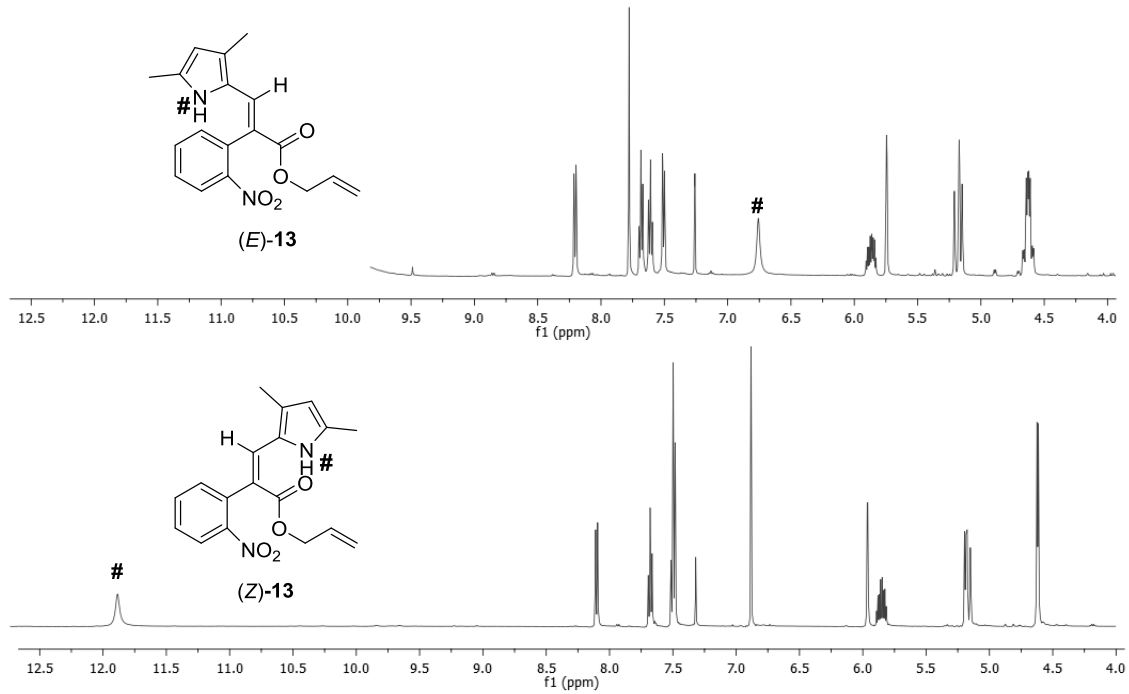

(b)

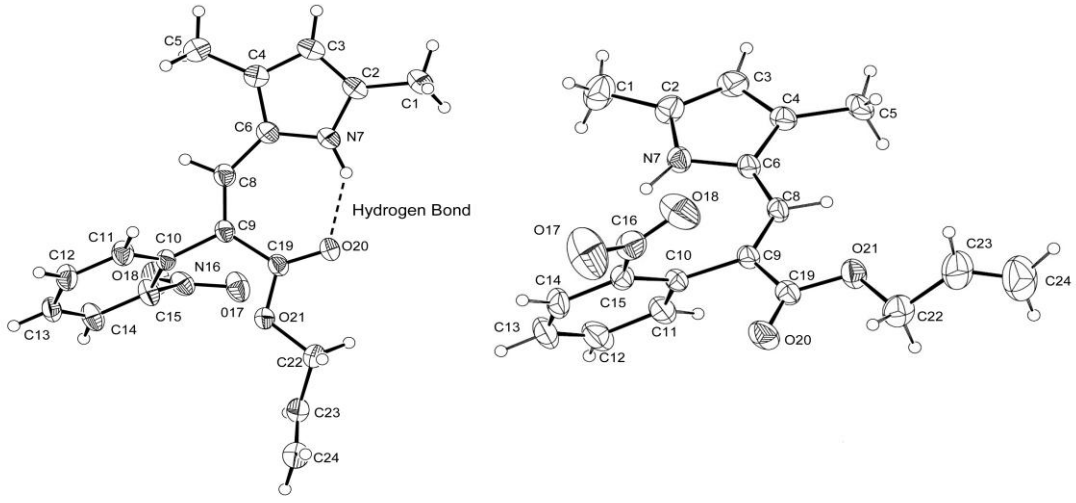

(*Z*)-**13** (*E*)-**13**

Figure 2.3. (a) ^{1}H NMR spectra highlighting the downfield chemical shifts of the pyrrole N-H signal in (*Z*)-**13** relative to (*E*)-**13**. (b) X-ray crystal structures of (*Z*)-**13** and (*E*)-**13** (solved by Tony Willis, ANU). Anisotropic displacement ellipsoids show 30% probability levels. Hydrogen atoms are drawn as circles with small radii. Crystallographic data for (*Z*)-**13** and (*E*)-**13** are provided in Chapter 6.1.1. Appendices 1(c) and 1(d).

Ester and amide couplings were also explored (by me, during Honours) with the *trans*-acid (*E*)-**5**. It was rationalised that (*E*)-**5** might not be susceptible to intramolecular cyclisation due to the unfavourable positioning of the pyrrole N-H *trans* to the carboxylic acid moiety and because it lacked the activating H-bond. If the desired couplings were found to proceed, it was envisaged that the *trans* products could be converted to the requisite *cis* isomers through alkene isomerisation. Under most of the couplings examined, however, the 3*H*-pyrrolizin-3-one **14** was again observed as the major product, suggesting that isomerisation of (*E*)-**5** to (*Z*)-**5** was facile under the reaction conditions investigated.

2.4 Indole-*N*-oxides 15 and 16

2.4.1 Discovery of 15 and 16

A notable change in the reactivity of *trans* acid (*E*)-**5** was observed during attempted couplings with HBTU and *N*,*N*-dimethyl-*p*-phenylenediamine (DMPD) in the absence of bases (Figure 2.4(a)). Bases were deliberately excluded from reactions to reduce base-promoted isomerisation of (*E*)-**5** to (*Z*)-**5** and subsequent 3*H*-pyrrolizin-3-one formation. The reactions did not produce the expected *trans*-amide product or 3*H*-pyrrolizin-3-one **14**, however, but instead formed a deep purple solid as the major product. A crystal of the compound was obtained from Et_2O/pet. spirit and submitted to Tony Willis (ANU) for X-ray analysis. The structure was solved as *(E)*-2-(3,5-dimethyl-1*H*-pyrrol-2-yl)-3-((4-(dimethylamino)phenyl)imino)-3*H*-indole 1-oxide **15** (Figure 2.4(b)). ^{1}H and ^{13}C NMR spectra (Chapter 6.2 Appendix 2) for **15** were consistent with the structure determined by X-ray analysis.

The reaction proceeded further to completion when *p*-phenylenediamine (PPD) was used in place of DMPD, providing a higher isolated yield (56%) of the dark purple solid **16**, (c.f. 40% **15** with DMPD).

(a)

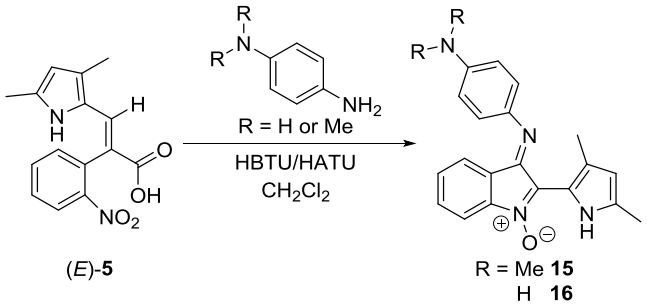

(b)

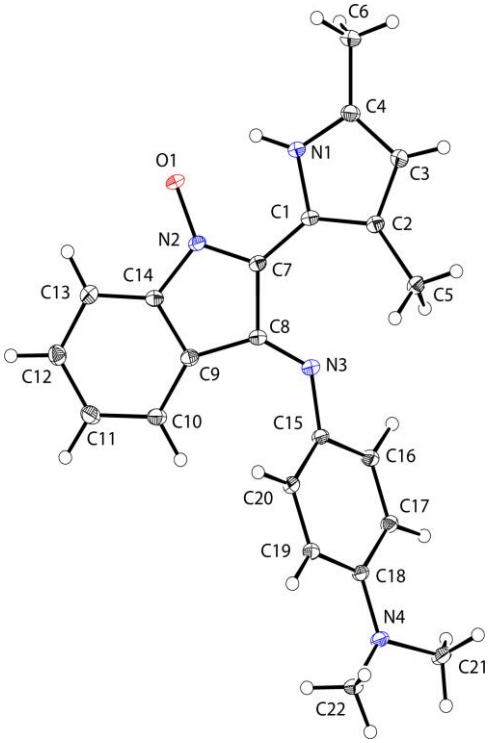

Figure 2.4. (a) Synthesis of **15** and **16** from (*E*)-**5**, (b) X-ray crystal structure of **15** (solved by Tony Willis, ANU). Anisotropic displacement ellipsoids show 30% probability levels. Hydrogen atoms are drawn as circles with small radii. Crystallographic data for **15** are provided in Chapter 6.1.1. Appendix 1(e).

2.4.2 Further Explorations with 15 and 16

Compound **16** was found to be unstable, producing two decomposition products soon after purification by silica gel column chromatography. The two products were (1) an intensely coloured violet solid and (2) PPD, suggesting that hydrolysis of **16** to the novel violet ketone derivative 2-(3,5-dimethyl-1*H*-pyrrol-2-yl)-3-oxo-3*H*-indole 1-oxide **17** (Figure 2.6(a)) had occurred. Acids (*E*)-**5** and (*Z*)-**5** were similarly observed to decompose over time, forming the same violet solid **17** and a second red amorphous solid which was characterised as the *trans*-alkene **18**. The reaction was apparently proceeding through a spontaneous decarboxylation followed by an electrocyclic reaction of an intermediate allene (Figure 2.5(a)).

NMR studies to monitor the spontaneous decompositions were performed by leaving (*Z*)-**5** in an NMR tube in $CDCl_3$ over a period of two weeks (Figure 2.5(b)). The ^1H NMR spectra shown in Figure 2.5(b) showed that **18** forms spontaneously from (*Z*)-**5**. Trace quantities of **17** were also observed, which could not be explained mechanistically.

(a)

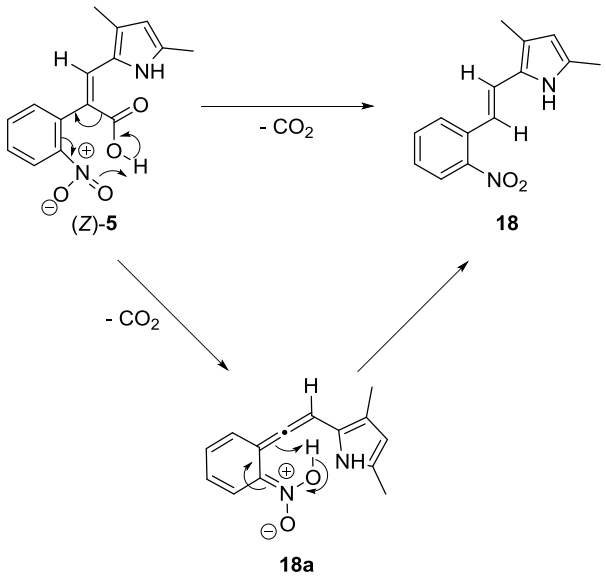

(b)

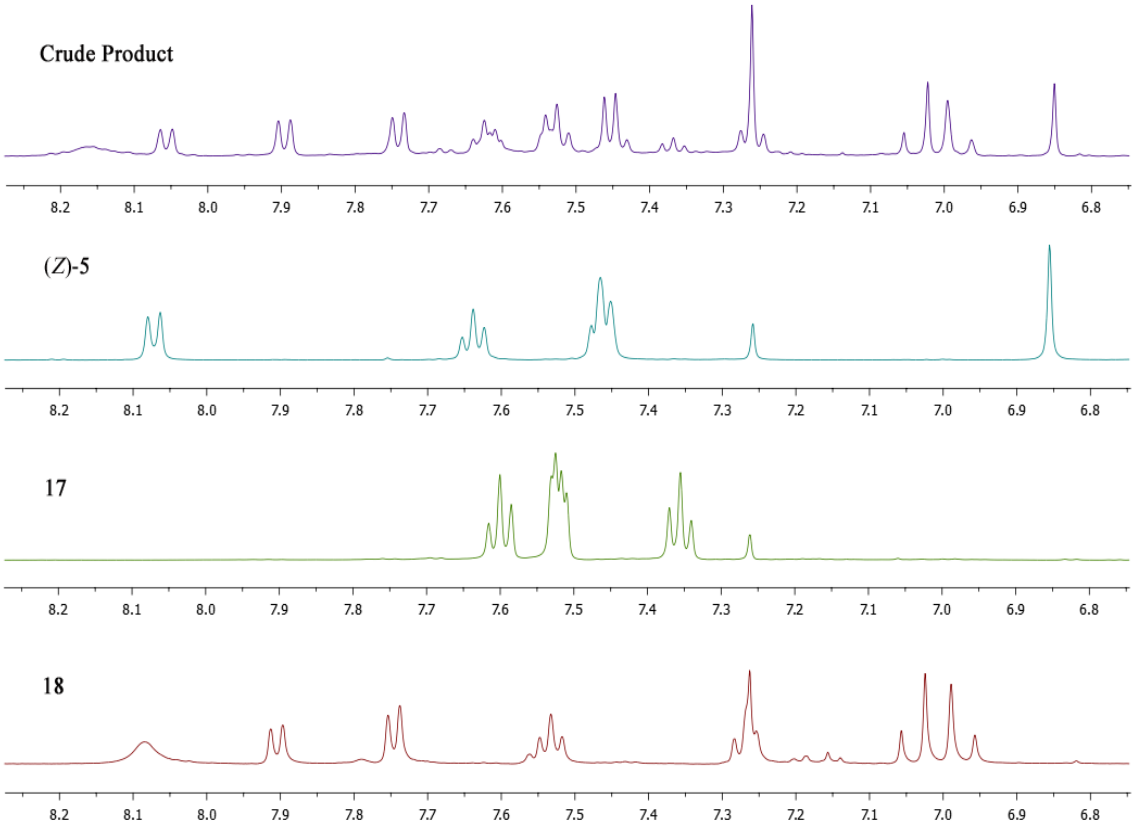

Figure 2.5. (a) Proposed mechanism for decomposition of (*Z*)-**5** to form **18** via allene **18a**. (b) Aromatic region of ^{1}H NMR spectra showing signals from the spontaneous decarboxylation of (*Z*)-**5** in $CDCl_3$ (Top). ^{1}H NMR spectra showing the equivalent chemical shift regions for pure samples of (*Z*)-**5**, **17** and **18**.

Attempts to deliberately hydrolyse **15** and **16** under acidic conditions (H_2SO_4 (cat.), THF) led to quantitative formation of ketone **17** (Figure 2.6(a)). A single crystal X-ray structure of **17** was solved by Tony Willis at ANU, confirming its structure (Figure 2.6(b)). ^{1}H and ^{13}C NMR, IR and HRMS were consistent with this structure. The imine **15** and ketone **17** shared similar UV-Vis spectra, with both showing absorption maxima around 350 nm and a broad maximum at 583 and 563 nm, respectively (Figure 2.6(c)).

The strong red-absorptions and intense violet colours were consistent with the extensive conjugation and delocalisation in the structures.

(a)

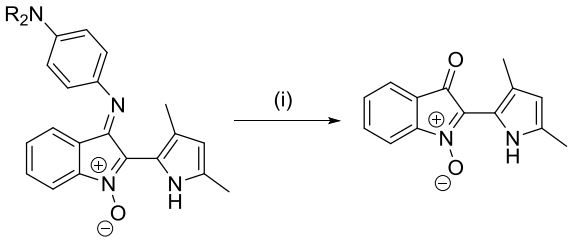

(b)

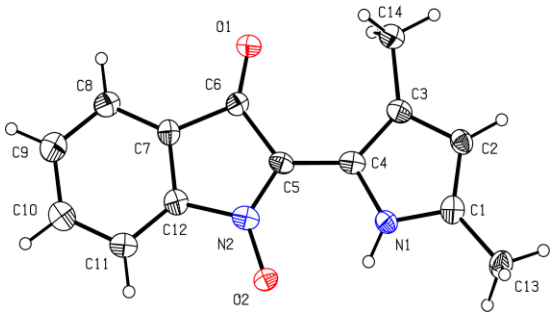

(c)

17

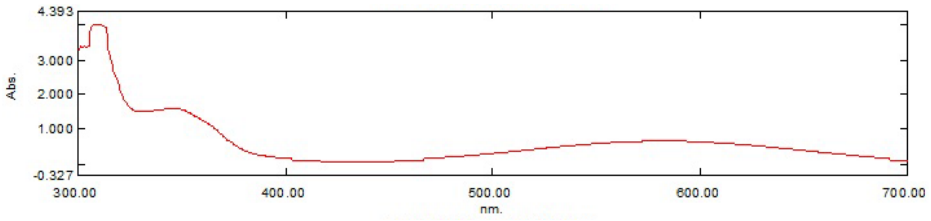

15

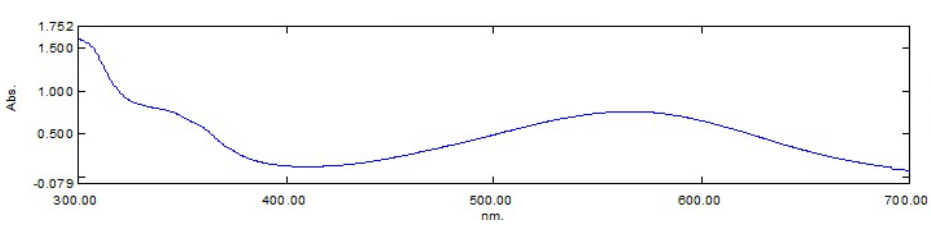

Figure 2.6. (a) Synthesis of the ketone **17**. Reagents and conditions: 1:1 1M HCl:THF, quant. (b) X-ray crystal structure of **17** (solved by Tony Willis, ANU). Anisotropic displacement ellipsoids show 30% probability levels. Hydrogen atoms are drawn as circles with small radii. Crystallographic data for **15** are provided in Chapter 6.1.1. Appendix 1(f). (c) UV-Vis spectra of imine **15** and ketone **17** in ethanol.

2.4.3 Proposed Mechanism for Formation of 15 and 16.

Further synthetic studies were undertaken to probe the reaction mechanisms leading to formation of **15** and **16**. Firstly, it was found that *cis*- and *trans*-carboxylic acids (*Z*)-**5** and (*E*)-**5** both worked equally well in the reaction. Facile *cis* to *trans* isomerisation promoted by electron donation from the pyrrole nitrogen into the carboxylic acid carbonyl and NO_2 groups would give the alkenic double bond significant single bond character, allowing facile rotation and isomerisation.

Introduction of TEMPO into the reaction at 10% or 100% by weight (relative to **5**) had no effect on the yield of **15** or **16**, suggesting that radicals were not involved in the mechanisms. Compounds **15** and **16** were not observed when replacing (*Z*)-**5** with pyrrolizin-3-one **14** or amides such as (*Z*)-**29** (see Table 2.1), eliminating these as intermediates. Addition of catalytic diisopropylethylamine (DIPEA) to reactions with HBTU, (*Z*)-**5** and *p*-phenylenediamines DMPD or PPD resulted in formation of 3*H*-pyrrolizin-3-one **14** as the major product. Use of the carbodiimide coupling reagent dicyclohexycarbodiimide (DCC) in base-free conditions yielded **14** as the only product.

The reaction proceeded more rapidly with additional mol eq. of HBTU or PPD. The reaction also proceeded well with the closely related coupling reagent 1-[Bis(dimethylamino)methylene]-1*H*-1,2,3-triazolo[4,5-b]pyridinium 3-oxide hexafluorophosphate) (HATU) and was indeed faster, completing in 30 min (c.f. 4 h with HBTU). No reaction was observed between the acids (*Z*)-**5** or (*E*)-**5** and HBTU or HATU in the absence of PPD or when PPD and the acids were combined in the absence of HBTU or HATU. In CH_2Cl_2, a very slow reaction was observed when HATU and PPD were added together, however. This reaction resulted in two new peaks at *m*/*z* 136 and 207 in the ESI^+ mass spectrum. Monitoring this reaction by ^1H NMR in d_6-DMSO

indicated formation of 2-(4-aminophenyl)-1,1,3,3-tetramethylguanidine **19** (Figure 2.7(a), MW = 206.29 g/mol). Its structure was subsequently confirmed by 2D NMR analysis and HRMS. 3*H*-[1,2,3]triazolo[4,5-b]pyridin-3-ol (HOAt, MW = 136.11 g/mol) was also formed in a 1:1 stoichiometric ratio in the reaction. Reactions of this type are supported by a literature precedent.[185] Peaks at *m*/*z* 207 and 136 were also observed in the ESI^+ mass spectrum of the crude reaction mixtures that formed **15** or **16** using HBTU or HATU, suggesting that the guanidinium species **19** was being formed in the reaction.

From a structural perspective, to form **16** from (*E*)-**5**, HATU and PPD, the alkenic β-carbon of (*E*)-**5** must attach to the NO_2 group's nitrogen atom and PPD must attach one of its nitrogen atoms to the α-carbon of (*E*)-**5**. This suggested that a pre-transformation to a resonance-stabilised nitrenium ion of PPD might be occurring. One possible mechanism for the formation of a nitrenium ion is shown in Figure 2.7(a). The oxygen atom of a second molecule of HATU could act as a nucleophile that attacks the guanidine carbon of protonated **19**. Elimination of tetramethylurea (TMU) would give the nitrenium derivative of PPD and reduced HATU. Peaks at 116 *m*/*z* (TMU) and 313 *m*/*z* (PPD-**19** adduct) were suggestive of this transformation.

A mechanism for the formation of **16** from (*E*)-**5**, PPD and HATU is proposed in Figure 2.7 (b). Formation of **19** from reaction of HATU with PPD occurs in step 1, which is followed by deprotonation of (*E*)-**5** to form the carboxylate anion and the protonated guanidininium form of **19** (step 2). Formation of the PPD+ nitrenium ion from **19** then occurs. An allene species **18a** is formed by decarboxylation of (*E*)-**5** (See Chapter 2.4.2, step 3). The nascent benzylic anion then attacks PPD+ (step 4). The resulting enamine triggers an intramolecular cyclisation (step 5) to form **16-H_2O**. Hydrogen atom transfer

followed by dehydration yield the final **16** (steps 6 and 7). While the mechanism is consistent with the available data, further experiments are needed to confirm it.

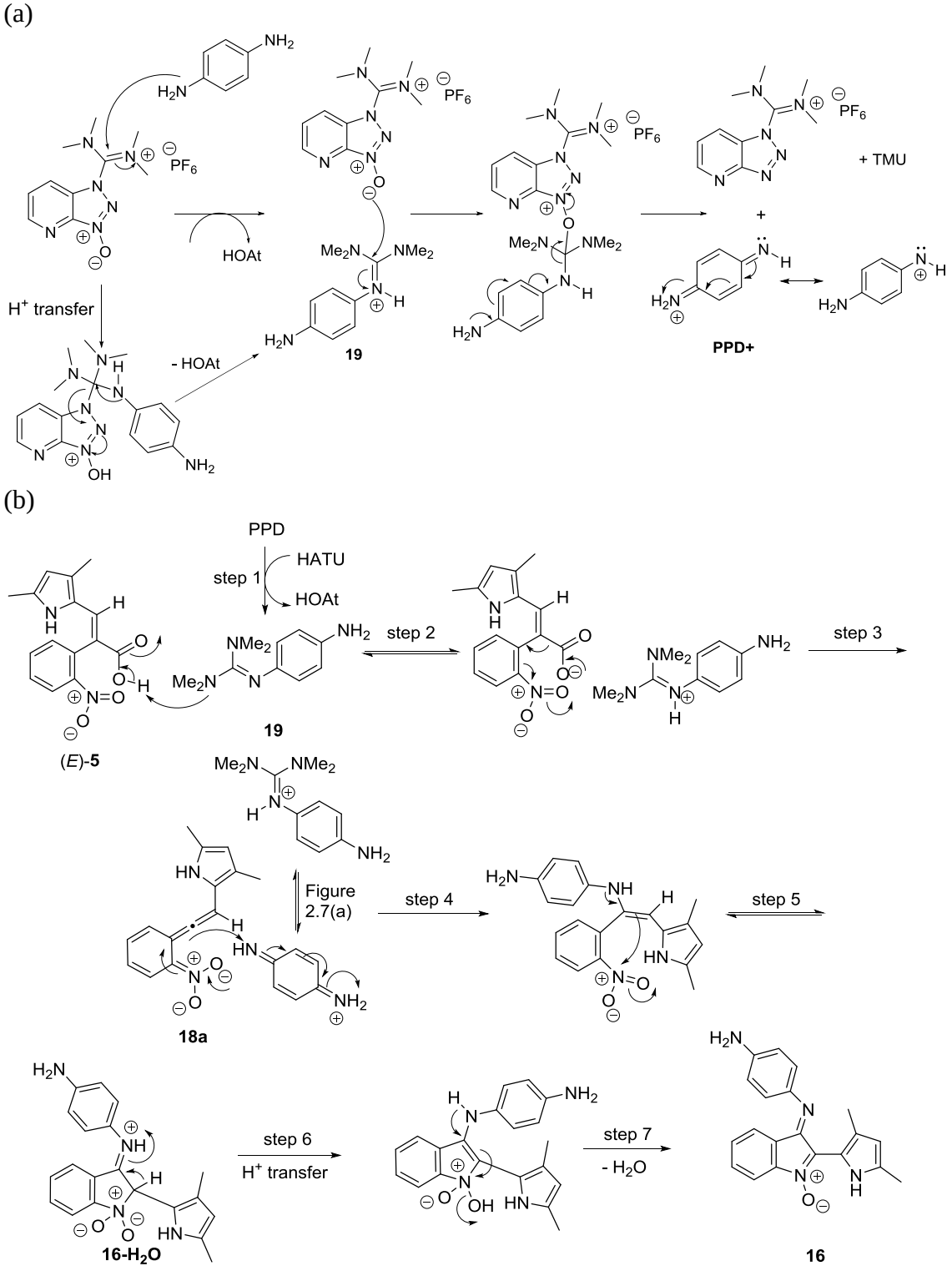

Figure 2.7. Proposed mechanism of formation of (a) nitrenium ion PPD+ from reaction of HATU with PPD and (b) **16** from reaction of (*E*)-**5**, PPD and HATU.

2.5 Antiplasmodial Activity of 17

A literature search revealed that ketone **17** was a novel analogue of indolone-*N*-oxides that have previously been shown to possess *in vitro* antibacterial, antifungal and antiplasmodial activity.[186–188] The broad antimicrobial properties of the class are attributed to generation of reactive oxygen species, although antiplasmodial activity was also attributed to a redox process in infected red blood cells (RBCs) that causes destabilisation of cells and parasite death.[186,187]

Reported analogues contained various aryl and alkyl groups at the position occupied by the 3,5-dimethylpyrrole in **17**, along with substituents on 6-membered ring of the indolone-*N*-oxide (Figure 2.8), synthesised using Sonogashira couplings between aryl alkynes and 2-nitrophenyl halides to form 2-nitrophenylalkyne derivatives that cyclised *in situ*.[186,187] The most potent antiplasmodial was 2-(4-(dimethylamino)phenyl)-5-methoxy-3-oxo-3*H*-indole 1-oxide **20**.[186,187] Compound **20** showed an IC_{50} of 1.7 nM against the 3D7 strain of *P. falciparum* (African, chloroquine-sensitive strain) and IC_{50} < 3 nM against the FcB1 (chloroquine-resistant) strain. It also had good selectivity, showing > 14,600-fold higher activity against the parasite than MCF-7 breast cancer cells.

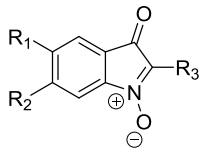

R_1 = OMe, OCH_2-OR_2, H
R_2 = OMe, OCH_2-OR_1, H
R_3 = aryl, alkyl

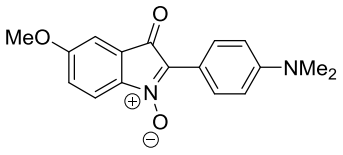

20

Figure 2.8. Reported indolone-*N*-oxides with antiplasmodial activity.[186–188]

Compound **17** was tested using the microdilution radioisotope technique against the K1 (multidrug resistant) strain of *P. falciparum* by collaborators at the National Center for

Genetic Engineering and Biotechnology (BIOTEC) Thailand, where it returned an IC_{50} = 381 nM.[189,190] Cytotoxicity of **17** against Vero cells was also determined using an Alamar blue viability assay,[191] where it showed CC_{50} = 58.4 μM, giving it a selectivity index of 153. As it was less potent and selective than compound **20**, and with literature already published on the indolone-*N*-oxide series, further biological investigations with **17** were not undertaken.

2.6 Substrate Scope of the Knoevenagel Condensation

With the divergent approach (**Route 1**) towards codrug **1** (i.e. via the carboxylic acid (*Z*)-**5**) no longer appearing feasible, attention was turned to **Route 2**, where the amide bond is formed first followed by the Knoevenagel condensation. Pursuing **Route 2** required confirmation that the Knoevenagel condensation could also be carried out with amides as well as esters. Model amides **23** and **24** were prepared by coupling 2-nitrophenylacetic acid to aniline and benzylamine in 95% and 94% yields, respectively, using HBTU as the coupling reagent. Both amides underwent the desired condensation with pyrrole aldehyde **9** to form the *cis*-alkenes (*Z*)-**29** and (*Z*)-**30** in 22% and 16% yields, respectively, using the standard conditions that had been developed. The analogous ethyl amide **22** and Knoevenagel product (*Z*)-**28** were prepared in 2012 by a Kelso Lab Honours student (Rhys Mitchell) in 21% yield.

It was noted that while the ester derivatives tended to form similar proportions of *cis* and *trans*-alkene products, the amides formed mostly the *cis* isomer. For example, use of ethyl ester **3** produced (*Z*)-**10** and (*E*)-**10** in 42% and 35% yields, respectively (Table 2.1, Entry 1). The methyl ester **21** produced (*Z*)-**27** and (*E*)-**27** in 36% and 40% yields (Table 2.1, Entry 2), while allyl ester **12** produced (*Z*)-**13** and (*E*)-**13** in 41% and 31%

yields, respectively (Table 2.1, Entry 3). In comparison, the ethylamide derivative **22** produced 21% of the *cis* product (*Z*)-**28** and none of the *trans* isomer (*E*)-**28** (Table 2.1, Entry 4). Similarly, the aniline and benzylamine derivatives **23** and **24** produced (*Z*)-**29** and (*Z*)-**30** in 22% and 16% yields, respectively, and less than 5% of (*E*)-**29** and (*E*)-**30** were produced and neither could be isolated in pure form (Table 2.1, Entries 5 and 6).

Rhys was also successful in synthesising ethyl ester derivatives where the 2-nitrophenyl moiety was replaced with phenyl or 2-chlorophenyl groups. The Knoevenagel condensation in these cases required use of the much stronger base LDA. Interestingly, the phenyl derivative **25** produced a 32% yield of the *trans*-phenyl analogue (*E*)-**31** and no *cis*-product (*Z*)-**31** (Table 2.1, Entry 7). A 41% yield of the *trans* 2-chlorophenyl product (*E*)-**32** was obtained from **26** with only 5% of (*Z*)-**32** being isolated (Table 2.1, Entry 8). A summary of all compounds prepared via the Knoevenagel condensation is provided in Table 2.1. Compounds re-synthesised by me during my PhD studies are indicated with an *. Compounds I synthesised for the first time during my PhD studies are indicated with a #. Full characterisation and experimental procedures are provided for the latter only, along with their associated intermediates.

Table 2.1. Summary of Knoevenagel condensations. Reagents and conditions: a. K_2CO_3, 18-crown-6, THF, reflux, 16 h; b. LDA, THF, -78 ^oC, 30 min.

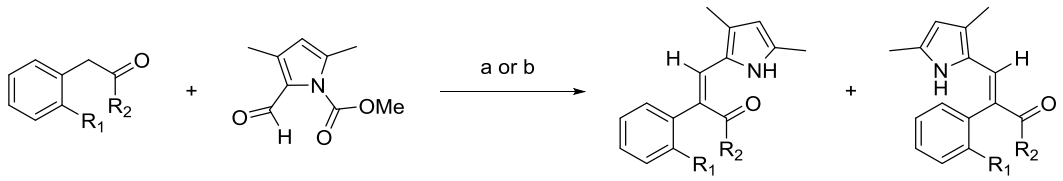

3, 12, 21-26 **9** (*Z*)-**10, 13, 27-32** (*E*)-**10, 13, 27-32**

Entry	Phenylacetic ester[B]/amide[C]	R_1	R_2	Reaction Conditions	Product, yield %	Product, yield %
1	**3**	NO_2	OEt	a	(*Z*)-**10**, 42*	(*E*)-**10**, 35*
2	**21**	NO_2	OMe	a	(*Z*)-**27**, 36*	(*E*)-**27**, 40*
3	**12**	NO_2	OAll	a	(*Z*)-**13,** 41*	(*E*)-**13**, 33*
4	**22**	NO_2	NHEt	a	(*Z*)-**28**, 21	(*E*)-**28**, 0[A]
5	**23**	NO_2	NHPh	a	(*Z*)-**29**, 22[#]	(*E*)-**29**, <5[A,#]
6	**24**	NO_2	NHBn	a	(*Z*)-**30**, 16[#]	(*E*)-**30**, <5[A,#]
7	**25**	H	OEt	b	(*Z*)-**31**, 0	(*E*)-**31**, 32
8	**26**	Cl	OEt	b	(*Z*)-**32**, 5	(*E*)-**32**, 41

[A]Compound could not be isolated in pure form
[B]Esters **3**, **21**, **25-26** were synthesised by refluxing the phenylacetic acids in the requisite alcohol (as solvent) with catalytic H_2SO_4.
[C]Amides **22-24** were synthesised by coupling 2-nitrophenylacetic acid to the requisite amines using standard amide coupling conditions (HBTU/DIPEA, CH_2Cl_2).

2.7 Anti-Angiogenic Properties of Alkene Products

When designing codrug **1**, it was reasoned that the presence of the attached cytotoxin should render the pro-angiogenesis inhibitor moiety (based on SU5416 **2**) inactive due to the added steric bulk. Lack of the oxindole portion of SU5416 was also expected to

ablate angiogenesis inhibition as all published SAR studies with SU5416, sunitinib and related analogues retained this key moiety.[134] These hypotheses were examined by testing the antiangiogenic activity of the model *cis* and *trans* derivatives of **10, 13** and **27-32** obtained from the Knoevenagel condensations. The Et and Me esters (*Z*)-**10** and (*Z*)-**27** had been shown to be angiogenesis inhibitors in preliminary experiments at the start of my PhD studies but none of the other derivatives had been tested.

Compounds were examined using a rat aortic ring angiogenesis assay in the lab of Prof. Chris Parish at the John Curtin School of Medicine (ANU) by a research assistant Anna Bezos.[192] In this model, 1 mm sections from female rat aortas are suspended in a fibrin gel matrix and exposed to growth media. The aortic sections form new blood vessel sprouts over 5 days, which are scored manually as the % field of view (F.O.V.) occupied under a light microscope. Inhibitors of angiogenesis produce a quantifiable reduction in the F.O.V. occupied by the sprouting blood vessels. Figure 2.9 provides a summary of this assay.

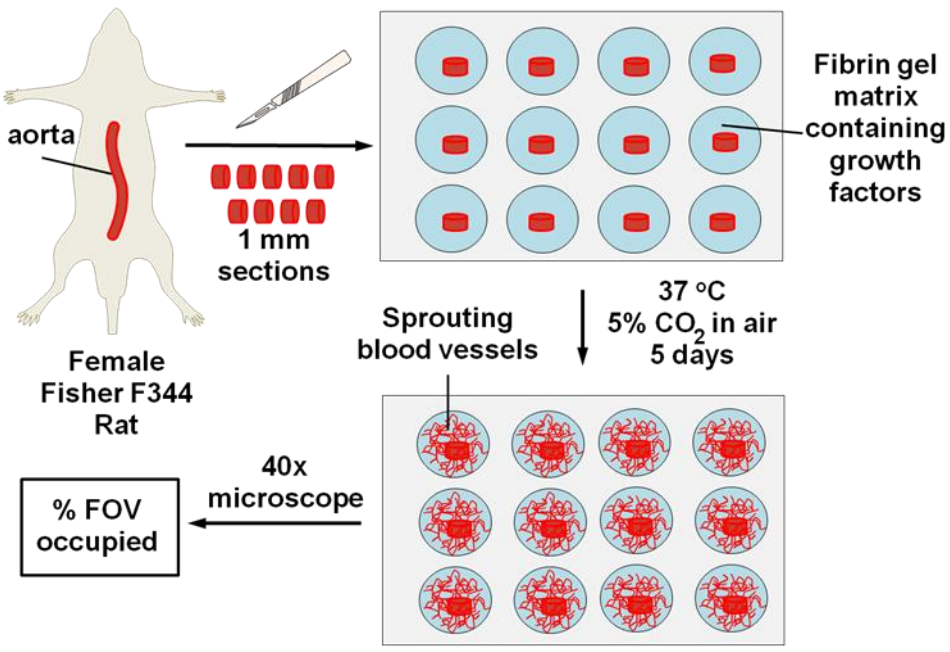

Figure 2.9. Summary of rat aortic ring angiogenesis inhibition assay performed by Anna Bezos at the John Curtin School of Medicine (ANU).

Two positive controls PI-88 and SU5416 were included in the assays. PI-88 is a highly sulfated oligosaccharide-based angiogenesis inhibitor that underwent Phase III clinical trials as a treatment following cancer resection in patients with hepatitis virus-related hepatocellular carcinoma.[193] At 100 µg/mL, PI-88 reduced F.O.V. occupancy to 39.2%. SU5416 (synthesised by me using the literature method)[184] produced significantly higher inhibition of angiogenesis at 10 µg/mL (F.O.V. occupancy 9.7%) than at 100 µg/mL (F.O.V. occupancy 30.6%), while 61.4% F.O.V. occupancy was observed at 1 µg/mL. Small crystals observed in wells containing 100 µg/mL SU5416 **2** suggested that the poor dose dependency may have been due to low solubility of the compound in the assay medium.

Et and Me esters (*Z*)-**10**, (*E*)-**10**, (*Z*)-**27**, and (*E*)-**27** were found to completely inhibit angiogenesis at 100 µg/mL. At 10 µg/mL, (*E*)-**10** continued to show complete inhibition, whereas the other three esters all showed significantly diminished effects at this concentration. At 1 µg/mL the four esters showed either minimal effects (< 20% difference relative to negative control) or no activity. Surprisingly, the *cis*-allyl ester (*Z*)-**13** showed the same level of inhibition at both 100 and 10 µg/mL (F.O.V. occupancy 28.3 and 29.3%, respectively) but no activity at 1 µg/mL. For the *trans*-allyl ester (*E*)-**13**, strong activity was observed at 100 µg/mL (F.O.V. occupancy 8.3 %), but this activity was completely ablated at 10 µg/mL. It was concluded that (*E*)-**10** was the most active angiogenesis inhibitor of the 2-nitrophenylacetic ester series.

The c*is*-ethylamide (*Z*)-**28** showed reduced effects (F.O.V. occupancy 51.7% at 100 µg/mL, inactive at 10 µg/mL) relative to (*Z*)-**10**, confirming that directly substituting the

ester group for an amide is detrimental to activity. Observing that phenyl and benzyl amides (*Z*)-**29** and (*Z*)-**30** were inactive at 100 µg/mL supported this conclusion. These results also implied that **1** should be a poor angiogenesis inhibitor because it also incorporated an amide linkage.

Removal of the NO_2 group from the phenyl ring was found to completely abolish activity (i.e. (*E*)-**31** v. (*E*)-**10**). Interestingly, replacing the NO_2 group with Cl had no effect on activity at 100 µg/mL, with both (*E*)-**32** and (*E*)-**32** completely inhibiting angiogenesis. At 10 µg/mL, however, (*E*)-**32** showed no activity. Results are summarised in Figure 2.10.

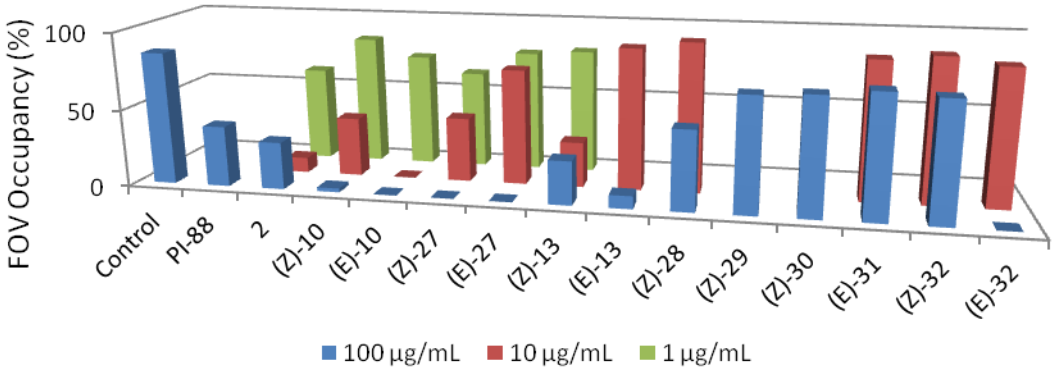

Figure 2.10. Rat aortic ring angiogenesis inhibition assay. Inhibition of angiogenesis by compounds **10**, **13** and **27-32** relative to negative control (no compound) and positive controls PI-88 (100 µg/mL) and SU5416 **2**. Negative control (no compound) showed 85.7% F.O.V. occupancy. Data represent the mean F.O.V. occupancy (%) generated from at least six replicate cultures of each test compound at each concentration.

2.8 Optimisation of Knoevenagel Condensations with Aryl Amides

The Knoevenagel condensation conditions used in the preparation of esters **10**, **13** and **27** employed 1.0 mol eq. of 2-nitrophenylacetate ester, 1.5 mol eq. of K_2CO_3, 0.5 mol eq. of 18-crown-6 and 1.0 mol eq. of pyrrole aldehyde **9**. These reactions were typically stirred for 12-16 hours at 65-75 ^oC in dry THF. Initial attempts using these conditions to synthesise amides **29** and **30** revealed the need for scrupulously anhydrous conditions and the importance of reaction times. Knoevenagel condensations to produce esters **10**, **13** and **27** could be left heating beyond completion of the reaction and were not affected by small changes in the reaction protocol. On the other hand, the amides produced intractable mixtures without freshly prepared, scrupulously dried reactants, reagents and solvents, and required strict adherence to the protocol with careful monitoring. The reactions were low yielding and the *trans* products were generally unable to be isolated in pure form (by column chromatography). Several coloured side products were also formed that were not observed in the ester-based reactions, making purification by column chromatography difficult. A study was undertaken to examine the side products formed during the Knoevenagel condensation between pyrrole aldehyde **9** and anilide **23** to form (*Z*)-**29**. Importantly, this study aimed to identify conditions that could be transferred to the synthesis of codrug **1** via **Route 2** (Figure 2.1).

Parameters varied during the optimisation study included the solvent, base and reaction times (Table 2.2). All reactions were carried out using 1.5 mol eq. of the indicated oven-dried potassium salts (as base), 1.0 mol eq. of 2-(2-nitrophenyl)-*N*-phenylacetamide **23** and 1.0 mol eq. of 18-crown-6. Reactions were stirred at 65 ^oC in freshly distilled dry solvent under a N_2 atmosphere. After 1.0 hour, a solution containing 1.0 mol eq. of aldehyde **9** in the same solvent was added dropwise to the stirred mixture under N_2. The reactions were monitored by TLC (8:2 pet. spirit:acetone) until complete consumption of aldehyde **9** was observed. Reactions were then quenched by addition of water and the

solvent removed under reduced pressure. The remaining aqueous mixture was extracted with 50 mL of Et_2O and washed with saturated $NaHCO_3$ solution and brine. The organic layers were combined and dried over $MgSO_4$ and evaporated to dryness. The crude residues were purified by column chromatography and the products isolated and identified (where possible).

When performing column chromatography, a slow gradient from 100% pet. spirit to 8:2 pet. spirit:acetone (without pressure) yielded a fast eluting non-polar product **33**. Compound **33** was a yellow oil that showed *m/z* 315 by ESI-MS. After 7 h only trace **33** was isolated by column chromatography but its yield increased to 3% after 10 h and 15% after 14 h (Table 2.2, Entries 1-3).

The non-polar compound was characterised and unambiguously identified as the *N*-phenyl analogue of SU5416 **33**, apparently formed via intramolecular cyclisation of the amide nitrogen onto the phenyl ring carbon bearing the nitro group and loss of HNO_2 (Figure 2.11). While uncommon, intramolecular cyclisation of amides onto aryl nitro groups has been reported in the literature.[194,195] This was an interesting result as *N*-aryloxindoles are typically made by transition-metal catalysed reactions between aryl halides and the oxindole NH. While not examined here, exploration of this chemistry might reveal a general method for preparing *N*-aryloxindoles. Based on this observation, a corresponding product was predicted to form (confirmed, see Chapter 3.2.4) during Knoevenagel condensations between **8** and **9** to produce **7** enroute to **1** via **Route 2**.

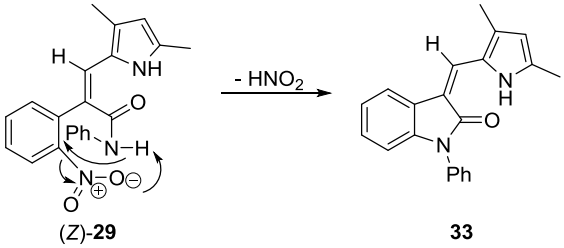

(*Z*)-**29** **33**

Figure 2.11. Postulated mechanism for the formation of **33** from (*Z*)-**29**.

A second product identified in the reactions was the *N*-deprotected pyrrole aldehyde **4**, which was isolated in 9% yield after 7 h, 11% after 10 h and 28% after 14 h (Table 2.2, Entries 1-3). Compound **4** presented problems during purification as it streaked on silica gel columns and contaminated fractions containing the *cis*-product (*Z*)-**29**. Compound (*Z*)-**29** was obtained in 28% yield after 7 h and 38% after 10 h (Table 2.2, Entries 1-2). After 14 h, (*Z*)-**31** was difficult to separate from compound **4**, providing only 22% of pure material (Table 2.2, Entry 3). Remaining starting materials (i.e. pyrrole aldehyde **9** and amide **23**) co-eluted from the column. The *trans* product (*E*)-**29** eluted very slowly from the column and it was difficult to separate from the streaking amide **23**. The best column chromatography protocol for purification of (*Z*)-**29** and (*E*)-**29** involved use of a slow gradient from 100% pet.spirit to 8:2 pet. spirit:acetone without application of pressure and over a period of 5 h.

Conditions for the synthesis of (*Z*)-**29** and (*E*)-**29** that enabled acceptable purification by column chromatography involved using 1.0 mol eq. of **23** and **9**, 1.5 mol eq. of K_2CO_3 and 1.0 mol eq. of 18-crown-6, with THF as solvent and a reaction time of 10 h at 65 ^{o}C (Table 2.2, Entry 2). Use of K_3PO_4 and KO^{t}Bu as bases (Table 2.2, Entries 9 and 11) increased the rate of decarbamoylation of **9** to **4** (39% and 48% with K_3PO_4 and KO^{t}Bu, respectively). Yields of (*Z*)-**29** and (*E*)-**29** were also reduced to 18% and 7%, respectively, with K_3PO_4. No yield of (*Z*)-**29** or (*E*)-**29** was obtained with KO^{t}Bu. Yields of *N*-phenyl SU5416 **33** increased from 3% with K_2CO_3 to 5% with K_3PO_4 and 31% with KO^{t}Bu, suggesting that stronger bases assist its formation.

Alternative solvents were examined. Et_2O (Table 2.2, Entry 5) produced similar yields with 34% of (*Z*)-**29** formed (c.f. 38% in THF) and 29% of (*E*)-**29** (c.f. 26% in THF). A

20% yield of *N*-deprotected pyrrole aldehyde **4** was also produced (c.f. 3% in THF). CH_2Cl_2 (Table 2.2, Entry 4) resulted in lower yields of the products (18% yield of (*Z*)-**29** and 10% of (*E*)-**29**) as did $^{i}Pr_2O$ (25% (*Z*)-**29**, 19% (*E*)-**29**. Table 2.2, Entry 8). ^{t}BuOMe produced slightly lower yields compared to THF, (37% and 20% yields of (*Z*)-**29** and (*E*)-**29**, respectively), although the yield of **33** was increased to 40% (Table 2.2, Entry 7). Surprisingly, use of 1,4-dioxane failed to produce any (*Z*)-**29** or (*E*)-**29** (Table 2.2, Entry 6).

Table 2.2. Optimisation of Knoevenagel condensation to produce (*Z*)-**29**, (*E*)-**29** and **33**. Reagents and conditions: a. base, 18-crown-6, solvent, reflux.

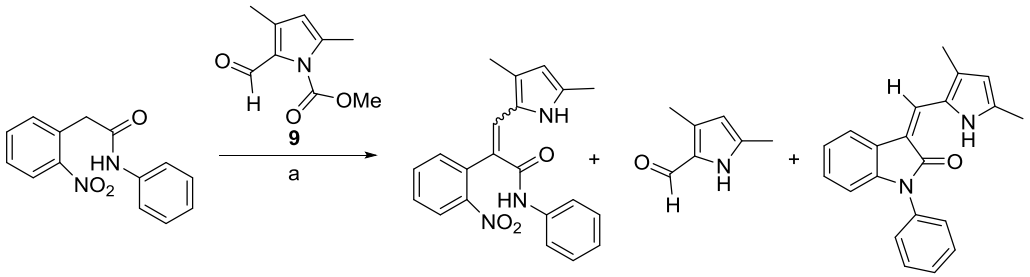

23 *(Z)*-**29** *(E)*-**29** **4** **33**

				Yield %			
Entry	Base	Solvent	Time (h)	*(Z)*-**29**	*(E)*-**29**	**4**	**33**
1	K_2CO_3	THF	7	28	14	9	< 1
2	K_2CO_3	THF	10	38	26	11	3
3	K_2CO_3	THF	14	22	< 5*	28	15
4	K_2CO_3	CH_2Cl_2	10	18	10	32	5
5	K_2CO_3	Et_2O	10	34	29	20	3
6	K_2CO_3	1,4-Dioxane	10	NO REACTION			
7	K_2CO_3	^{t}BuOMe	10	37	20	2	40
8	K_2CO_3	$^{i}Pr_2O$	10	25	19	26	10
9	K_3PO_4	THF	10	18	7	39	5
10	K_3PO_4	^{t}BuOMe	10	12	10	20	10

11	KOtBu	THF	10	0	0	48	31

*Could not be isolated in pure form.

Reactions were carried out by dissolving 0.2 g of **23** in 10 mL of dry solvent in a three-neck roundbottom flask along with 1.5 mol eq. of base and 1.0 mol eq. of 18-crown-6. Reactions were stirred at reflux for 1 h before adding 1.0 mol eq. of **9** in 3 mL of dry solvent dropwise under N_2 and stirring at reflux.

2.9 Summary and Future Directions

Work in this chapter showed that **Route 2** (Figure 2.1) showed promise as a way of accessing codrug **1** due to the successful Knoevenagel condensation between 2-(2-nitrophenyl)acetanilide **23** and pyrrole aldehyde **9**. Failure of the key acid intermediate (*Z*)-**5** to undergo ester and amide couplings ruled out further investigation of **Route 1**. A new class of angiogenesis inhibitors was produced using the novel Knoevenagel chemistry and several highly coloured reaction products were isolated and structurally characterised. These products had characteristic colours and it was thought that this feature might facilitate identification of more complicated byproducts produced when the reaction was attempted during the synthesis of **1** (Figure 2.12).

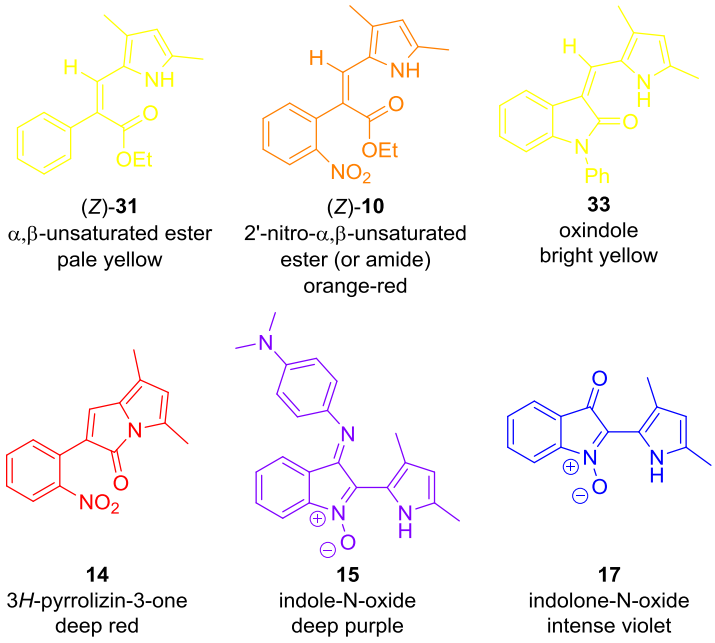

Figure 2.12. Coloured compounds synthesised in this Chapter.

Indole-*N*-oxides **15-18** were deep purple to violet in colour, whereas oxindoles **2** and **33** were yellow solids. Cyclisation to the 3*H*-pyrrolizin-3-one **14** produced a deep red crystalline solid, while the target α,β-unsaturated amide (*Z*)-**29** and ester (*Z*)-**10** were bright orange-red solids. Placing a hydrogen or chloride atom at the *ortho* position in place of the NO_2 group (i.e. (*E*)-**32** and (*Z*)-**32)**, led to solids with a pale yellow colour. These transformations were all accompanied by characteristic shifts in polarity by TLC analysis and diagnostic changes in ^{1}H and ^{13}C NMR spectra.

The scope and utility of these reactions could be explored in the future. For example, if successfully translated into a more general scheme, the synthesis of oxindoles such as **33** from 2-nitrophenylacetate derivatives would appear to be a more substituent-neutral reaction compared to the typical Fischer indole synthesis with late-stage decoration. This reaction would allow early substitution at the usually unreactive 5- and 6-positions as well as alkyl or aryl substituents at the nitrogen which would typically require strong base and unfavourable *N*-alkylation or transition-metal catalysis.

Exploration of the indole-*N*-oxide forming reactions (Chapter 2.4) to produce other intensely coloured products like **15** and **16** could be quite interesting. While **17** proved to be only a moderate antiplasmodial, the synthetic pathway to this indolone-*N*-oxide was novel. A three-step sequence from 2-nitrophenylacetic acid using a Perkin reaction followed by decarboxylative cyclisation (Chapter 2.4) and hydrolysis of the imine might provide indolone-*N*-oxides that are difficult to synthesise by other methods (Figure 2.13).

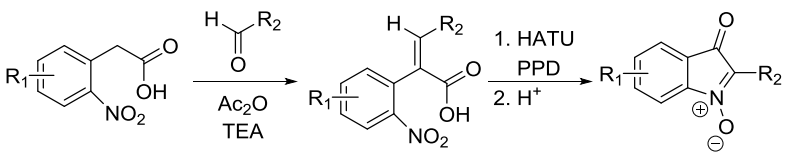

Figure 2.13. Proposed sequence to indolone-*N*-oxides from 2-nitrophenylacetic acid.

The reaction mechanism described in Chapter 2.4.3 presented much novel chemistry, although the mechanism was not unambiguously confirmed in this Thesis. Further confirmation of the mechanism could be obtained by trapping the nitrenium ion PPD+ or guanidine **19** with nucleophiles. Trapping of the 2-(2-nitrophenyl)-allene species with other electrophiles might also be informative. The *trans*-alkene **18** resulting from spontaneous decarboxylation of **5** may also provide similar reactivity in the presence of strong base. The utility of the novel 3*H*-pyrrolizin-3-one class of compounds, exemplified here by compound **14**, was examined in detail in Chapter 4.

Chapter 3

Synthesis of Codrug 1

and Proof-of-Concept Reduction

Reactions

3.1 Strategy (a)

Work in Chapter 2 identified **Route 2** as a promising way to access codrug **1** following confirmation of a successful Knoevenagel reaction between 2-(2-nitrophenyl)acetanilide **23** and *N*-protected pyrrole aldehyde **9** to produce (*Z*)-**29**. **Route 2** required preparation of a suitably *O*-protected amide intermediate **8**, which could undergo the Knoevenagel reaction with pyrrole aldehyde **9**. Two strategies towards **8** were considered (Scheme 3.1). In Strategy (a), the diethanolamine **35** (or its acid salt) could be prepared and then coupled with 2-nitrophenylacetic acid to give **34**. Protection of the alcohols could be performed before or after amide formation giving **8**. Strategy (b) would start by coupling *p*-phenylenediamine to 2-nitrophenylacetic acid to give amide **36**. Bis-*N*-alkylation of **36** with a 2-haloethanol would give **34** and after *o*-protection intermediate **8**.

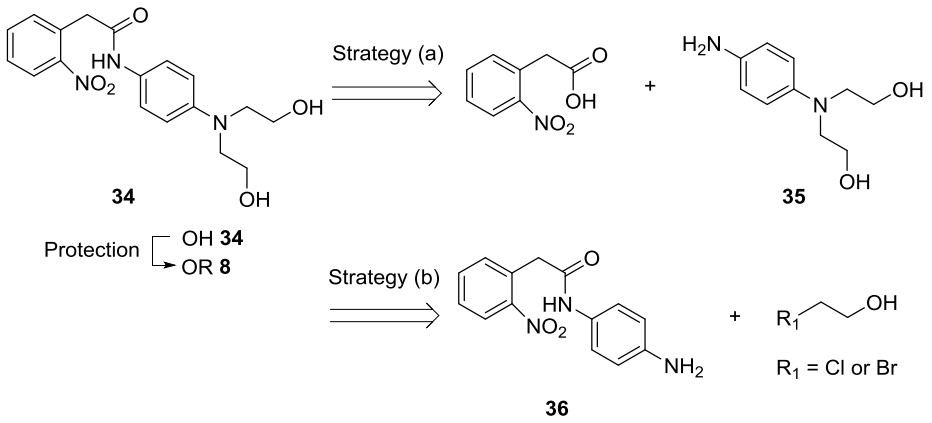

Scheme 3.1. Retrosynthetic analysis for key amide intermediate **8**.

Strategy (a) was preferred for several reasons. Firstly, synthesis of intermediate **35** had been previously described in the literature.[196] Secondly, the diethanolamine moiety could be introduced using reliable nucleophilic aromatic substitution chemistry (i.e. using 1-fluoro-4-nitrobenzene, thus avoiding the aryl amine bis-alkylation reaction required in Strategy (b). These reactions are often complicated by inefficient formation

of mixtures of primary, secondary and tertiary amines as well as quaternary ammonium salts which are difficult to separate.

In pursuing strategy (a), the first step involved forming the *p*-nitro-bis-ethanolamine derivative **37** (Scheme 3.2). 1-Fluoro-4-nitrobenzene was reacted with freshly distilled diethanolamine in DMSO at reflux, as per Ferlin et al.[196] The high aqueous solubility of the product **37** made isolation from DMSO very difficult. The reaction was subsequently repeated neat to avoid this complication, which resulted in a 77% yield of the desired yellow solid after recrystallisation from MeOH/H_2O (Lit. 96%).[196]

According to Ferlin et al., the free base form of *N*,*N*-bis-ethanolamino-*p*-phenylenediamine **35** can be isolated in EtOAc after $SnCl_2.2H_2O$-mediated NO_2 reduction with careful *p*H control.[196] While conversion of **37** to **35** appeared to be complete (monitored by TLC, 100% EtOAc), only a small amount of **35** was obtained in the EtOAc extract, even with careful *p*H monitoring. The small quantity of free base **35** obtained quickly decomposed into a black tar. The same article suggested that the more stable HCl salt could be obtained by addition of methanolic HCl to the free base, followed by evaporation. It was found, however, that the acid salt of **35** also degraded quickly and could not be obtained in useful quantities.

These challenges triggered investigations into an alternative procedure, where the NO_2 to NH_2 reduction was performed with H_2/Pd/C in order to simplify the workup. The reduction of **37** was carried out in methanol until TLC showed consumption of starting material. The mixture was then filtered through celite and concentrated *in vacuo*. The residue was redissolved in CH_2Cl_2 and immediately added to a solution of 2-nitrophenylacetic acid in CH_2Cl_2, which had been pre-activated to the HOBt ester with HBTU and DIPEA. This procedure failed to yield any of the desired amide **34**.

The H_2/Pd reduction was repeated in DMF and again went to completion. The mixture was filtered through celite directly into a pre-activated solution of the 2-nitrophenylacetic acid HOBt ester in DMF. This reaction also failed to yield any of the amide, suggesting that the phenylenediamine derivative was either insufficiently nucleophilic or was decomposing too rapidly to undergo amide coupling.

In an attempt to increase stability, **37** was bis-*O*-TBDMS-protected using standard literature conditions to produce derivative **38** in 72% yield (Lit. 95%).[197] The reduction reactions described above were each repeated with **38** in attempts to synthesise the TBDMS-protected amide **8** via amine **39**. While the reduction reactions with **38** appeared by TLC to produce **39**, subsequent coupling reactions using HBTU as the coupling reagent failed to yield any **8**. Additional attempts with 2-nitrophenylacyl chloride were similarly unsuccessful. At this point Strategy (a) was abandoned.

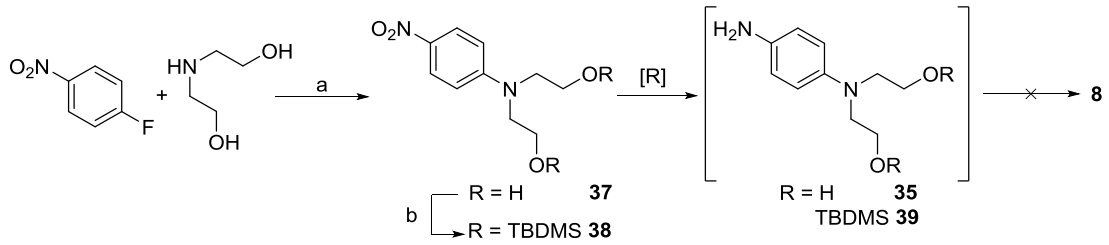

Scheme 3.2. Unsuccessful synthesis of key amide intermediate **8** using Strategy (a). Reagents and conditions: a. neat, reflux, 77%;[196] b. TBDMSCl, imidazole, CH_2Cl_2, 72%.[197]

3.2 Strategy (b)

3.2.1 Formation of amide 36

Difficulties encountered with Strategy (a) shifted the focus towards Strategy (b). The first step of this approach involved coupling 2-nitrophenylacetic acid to *p*-phenylenediamine. This previously unreported reaction was attempted under standard

HBTU/DIPEA coupling conditions at room temperature in CH_2Cl_2. Several gram scale reactions were completed where the mol eq. of various reactants/reagents were modified (Table 3.1). The highest yield of **36** (75%) was obtained with 1.0 mol eq. 2-nitrophenylacetic acid, 1.1 mole eq. of freshly recrystallised (EtOH) *p*-phenylenediamine, 1.1 mol eq. HBTU and 2.2 mol eq. DIPEA (Table 3.1, Entry 1). Increased equivalents of *p*-phenylenediamine reduced the yield of **36**.

Table 3.1. Optimisation of 2-nitrophenylacetic acid couplings with PPD to form **36**.

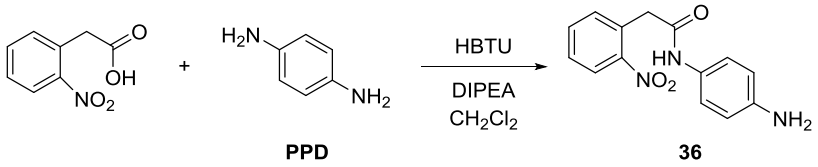

PPD **36**

Entry	acid, g	PPD g, mol eq.	HBTU g, mol eq.	DIPEA mL, mol eq.	**36**, %
1	5.07	3.33, 1.1	11.69, 1.1	10.7, 2.2	75
2	5.01	4.07, 1.4	10.60, 1.0	15.1, 3.1	67
3	3.97	5.11, 2.1	8.75, 1.1	9.2, 2.4	43
4	0.90	1.63, 3.0	2.11, 1.1	2.8, 3.2	40
5	0.20	0.48, 4.0	0.46, 1.1	0.5, 2.6	39

3.2.2 Bis-*N*-alkylation of 36

The next step in Strategy (b) involved formation of the diethanolamine derivative **34**, which required bis-*N*-alkylation of **36** with 2 eq. of a 2-haloethanol. K_2CO_3 was used as the base and 2-bromoethanol as both reagent and solvent. Test reactions were performed on a 20 mg scale under a variety of conditions (Table 3.2) with the highest yield being 67%. The reaction conditions were then increased to multigram scale where similar yields were obtained (Table 3.2 Entries 2 and 2a). The reactions generally required 4

days at 50 ^{o}C to consume the starting material. Temperatures above 50 ^{o}C resulted in intractable mixtures. Addition of 2-butanone as a co-solvent reduced the yield to 25% and resulted in the formation of a black sludge. Switching to 2-chloroethanol and addition of catalytic NaI (*in situ* iodination, i.e. Finkelstein reaction) failed to improve the yield (Table 3.2, Entries 3,4 and 7).

Table 3.2. Optimisation of bis-alkylation reaction conditions to produce **34**.

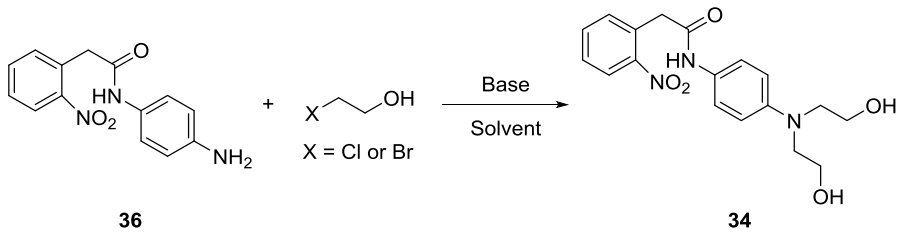

36 **34**

Entry	**36**, g	2-haloethanol X, mL	Base, g	Additive	Solvent	**34** yield, %
1	0.02	Br, 1.0	-	-	Neat	NR
2	0.02	Br, 1.0	K_2CO_3, 0.03	-	Neat	67
2a	1.90	Br, 15	K_2CO_3, 1.75	-	Neat	67
3	0.02	Br, 1.0	K_2CO_3, 0.03	NaI	Neat	53
4	0.02	Cl, 1.0	K_2CO_3, 0.03	NaI	Neat	4
5	0.02	Br, 1.0	-	-	2-butanone	NR
6	0.02	Br, 1.0	K_2CO_3, 0.03	-	2-butanone	25*
7	0.02	Br, 1.0	K_2CO_3, 0.04	NaI	2-butanone	21*

*Starting material was not completely consumed.

Amide **34** was subjected to the Knoevenagel reaction with aldehyde **9** under the optimised conditions (Chapter 2.8) but none of the desired alkene product (*Z*)-**7** was formed. It was observed that **9** underwent substantial *N*-deprotection to **4** during the reaction, suggesting that the nucleophilic diethanolamine hydroxyl groups might be causing problems.

3.2.3 Bis-silyl protection of 34

Two protecting groups were considered for the hydroxyl groups of **34**. Acetyl protection was investigated first, with bis-acetylation being achieved using acetic anhydride in pyridine. While the protection reaction was successful (72% yield), the subsequent Knoevenagel condensation with the bis-acetyl-protected diol was unsuccessful, producing only intractable mixtures containing many coloured products.

Bis-silylation of **34** with TBDMSCl to form **8** was examined next. Standard conditions using imidazole as a nucleophilic base/catalyst were explored in both DMF and CH_2Cl_2. Faster and more complete reactions were observed in CH_2Cl_2 (2 h, 86% yield c.f. 6 h, 72% yield in DMF). The reaction was successfully scaled up, with an 85% yield of **8** from 5 g of starting material **34**.

Table 3.3. Bis-silyl protection of **34** with TBDMSCl to form **8**.

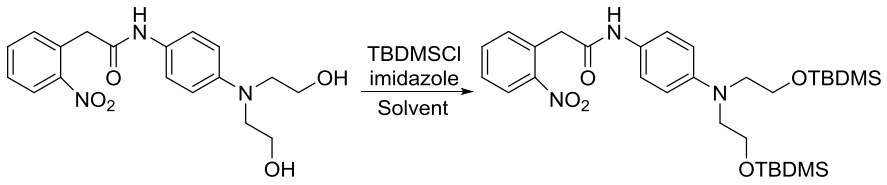

34 **8**

Entry	**34**, g	TBDMSCl g, mol eq.	Imidazole g, mol eq.	Solvent	Time, h	**8** yield, %
1	5.00	7.50, 3.6	8.10, 8.6	CH_2Cl_2	2.0	85
2	1.40	2.05, 3.5	2.34, 8.8	CH_2Cl_2	2.0	86
3	0.03	0.05, 4.0	0.06, 10.6	DMF	6.0	72

3.2.4 Knoevenagel Condensations with 8

With the efficient formation of TBDMS-protected amide **8** established on multigram scale, attention was next turned to the Knoevenagel condensation reaction between **8** and pyrrole aldehyde **9**. Solvents, bases, reaction times and techniques that had been tested previously on the aniline derivative **23** (Chapter 2.8) were used to guide the choice of conditions to explore. Several different reactions were examined but the standard conditions that had been previously optimised using K_2CO_3, 18-crown-6 in THF at 65 ^oC, and with the pyrrole aldehyde **9** added last after the reaction had reached 65 ^oC, were again found to be the best for this Knoevenagel reaction. The highest yields obtained of (*Z*)-**7** and (*E*)-**7** were 41% and 22%, respectively (Table 3.4, Entry 5).

The condensation reaction had to be carefully monitored as with the aniline amide **23** (See Chapter 2.6). *N*-aryloxindole **41** was formed as predicted, but stopping the reaction after 12 h limited its production such that it could only be isolated in trace amounts.

Table 3.4. Optimisation of Knoevenagel reaction to produce (*Z*)-**7** and (*E*)-**7** from **8**.

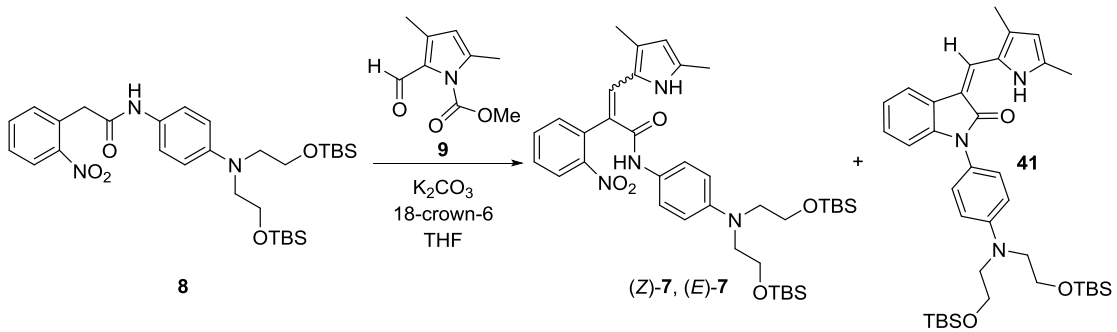

Entry	**8**, g	**9** g, mol eq.	K_2CO_3 g, mol eq.	18-Crown-6 g, mol eq.	Time, h	(*Z*)-**7**, (*E*)-**7** yield, %
1	1.13	0.35, 1.0	0.40, 1.5	0.53, 1.0	16	20, 10
2	2.00	0.60, 1.0	0.94, 2.0	0.97, 1.1	14	33, 28
3	2.98	1.10, 1.2	1.39, 2.0	1.01, 0.8	14	20, 11
4	1.00	0.36, 1.2	0.46, 2.0	0.35, 0.8	11	20, 17

5	1.15	0.47, 1.3	0.37, 1.35	0.67, 1.3	12	41, 22
6	1.08	0.57, 1.7	0.88, 3.5	0.64, 1.3	12	16, 15
7	0.77	0.23, 1.0	0.29, 1.6	0.42, 1.2	12	28, 20
8	0.41	0.22, 1.7	0.29, 3.0	0.39, 2.1	12	15, 10

3.2.5 Isomerisation Reactions with (*E*)-7

A series of isomerisation reactions were investigated with (*E*)-**7** in an attempt to increase the yield of (*Z*)-**7** but encouraging results were not obtained. The *trans*-alkene (*E*)-**7** could be partially isomerised using catalytic H_2SO_4 in THF, producing a 19% yield of the desired (*Z*)-**7** with 62% recovery of (*E*)-**7**. Base-promoted isomerisation using TEA or DIPEA was not successful, instead producing the oxindole derivative **41** as the major product.

3.2.6 Desilylation of (*Z*)-7

The next step in the synthesis of **1** involved deprotection of the two TBS ethers of (*Z*)-**7**. Desilylation reactions are often carried out using TBAF, a fluoride source that is soluble in organic solvents. Initial attempts using TBAF in THF at room temperature or at 0 ^{o}C were unsuccessful, resulting in mixtures of coloured products and decomposed starting material. It was suspected that the basicity of the fluoride ions might be causing problems.

Glacial acetic acid (1:5 v/v) was subsequently added to the TBAF/THF solutions to buffer the fluoride ion. These conditions resulted in clean conversions at room temperature to the bis-ethanolamine product (*Z*)-**42** in 85% yield after column chromatography. The reaction produced consistent results up to 0.5 g scale.

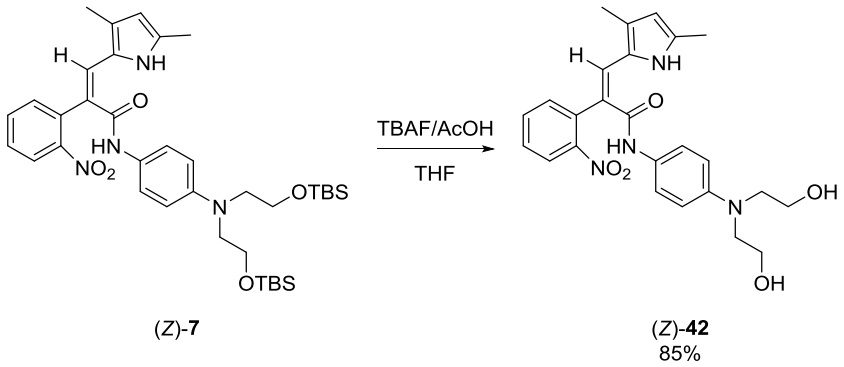

(*Z*)-**7** (*Z*)-**42** 85%

Scheme 3.3. Desilylation of (*Z*)-**7** afforded (*Z*)-**42** in 85% yield.

3.2.7 Bis-Chlorination of (*Z*)-42 to Produce Target Codrug (*Z*)-1

Several alternative groups could be considered for inclusion in the mustard arms of the codrug (*Z*)-**1**. Literature examples include use of chlorides, bromides or mesylates as leaving groups, or combinations of these. For example, evofosfamide utilises a bromophosphoramidite mustard,[171] busulfan a dimesyl mustard[198] and chlorambucil a dichloro mustard.[53]

A two-step process involving mesylation followed by halogen displacement was pursued in the first instance. Mesylation was achieved under standard conditions (MsCl, TEA in CH_2Cl_2), affording 86% isolated yield of the dimesyl product (*Z*)-**43** (500 mg scale). The compound proved to be unstable, however, and underwent polymerisation to a black tar, even when dried and stored at -20 ^oC under Ar. In subsequent halogenations attempts, mesylation reactions were quickly diluted in CH_2Cl_2 after completion, washed with saturated $NaHCO_3$ and brine and evaporated to dryness. The crude product was purified on a short (~7 cm) silica gel column using EtOAc as eluent and the freshly prepared bis-mesylate was dried under vacuum before being taken up in minimal DMF and treated with an excess of LiCl or LiBr. The reactions were stirred at 75 ^oC until the starting material was consumed (as observed by TLC analysis, 1:1 EtOAc:pet. spirit) and the product purified by column chromatography.

When halogenation reactions were performed on (*Z*)-**43** with lithium bromide, the desired dibrominated product was not detected. Using LiCl in DMF, however, the target compound (*Z*)-**1** was formed in 92% yield. Gratifyingly, it proved to be an air stable compound at room temperature. (*E*)-**1** was also isolated from the chlorination reactions, although it proved to be less stable than (*Z*)-**1**. Both (*Z*)-**1** and (*E*)-**1** were able to be fully characterised. A summary of the halogenation results is shown in Scheme 3.4.

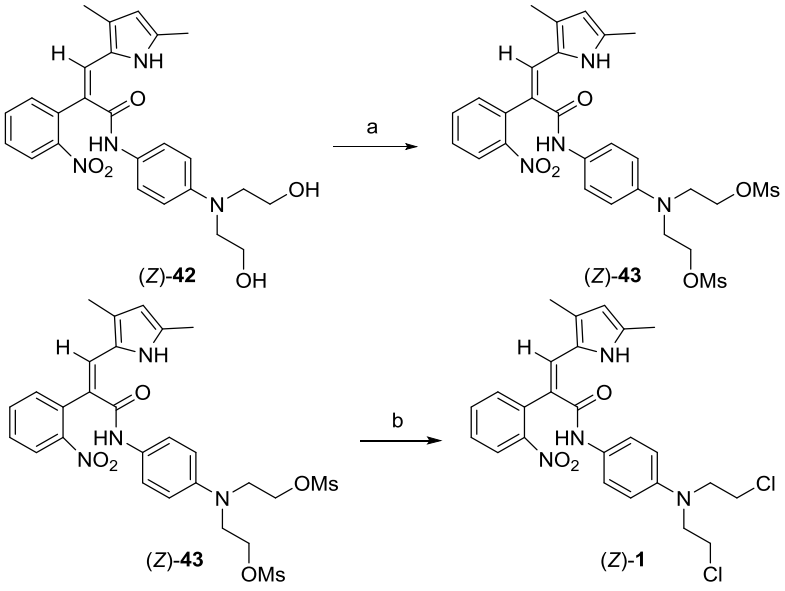

Scheme 3.4. Two-step procedure for the formation of (Z)-**1** from (Z)-**42** via mesylation followed by chlorination. Reagents and conditions: a. MsCl, TEA, CH_2Cl_2, 86%; b. LiCl (excess), DMF, 75 ^oC, 92%.

3.3 Proof-of-Concept Reduction Reactions

For the codrug (*Z*)-**1** to provide dual-action tumour killing *in vivo* it is necessary for the nitro group to spontaneously cyclise onto the amide carbonyl following bioreduction to the aniline, releasing SU5416 **2** and the phenylenediamine mustard (Figure 1.20). To probe this process, chemical reductions of the nitro group were investigated under three different conditions, including: (a) 10.0 mol eq. Fe^0 in 2:3:2 glacial acetic acid:EtOH:water with ultrasonication,[199] (b) 3.0 mol eq. $FeCl_3.6H_2O$ with 10.0 mol eq.

Zn in 1:1 DMF:water,[200] and (c) 2.0 mol eq. $NaBH_4$ with 10% w/w Pd/C in 2:1 MeOH:water. [201] These reactions were chosen for their mild conditions and because they were tolerant of alkenes, esters and amides.

If the proof-of-concept reductions were successful, nitro reduction to the amine (or hydroxylamine) would need to occur and be followed by spontaneous cyclisation, yielding SU5416 **2** (or *N*-hydroxy-SU5416 **2**-OH), which is also a potent inhibitor of VEGFR-2.[202] The reactions were monitored by TLC analysis and quenched immediately after the starting material had been consumed by filtering the reactions through celite. Reactions were conducted on 20 mg scale and the isolated yields of both **2** and **2**-OH were determined after purification by column chromatography. Yields of the phenylenediamine mustard were not obtained due to the compound's instability.

Ethyl ester (*Z*)-**10** was investigated as a model substrate for the reduction reactions by Pichit Sudta earlier in the Kelso Lab. **2** was identified as the major product under each of the three conditions. Fe^0 reduction yielded 81% of **2**, $FeCl_3$/Zn reduction produced 70% of **2**, along with 21% of **2**-OH, while $NaBH_4$ / Pd/C produced 72% of **2** and no **2**-OH (Figure 3.1).

Reductions were also investigated with the anilide derivative (*Z*)-**29**, which contained an aryl amide moiety like (*Z*)-**1** (reactions were performed by me as part of my PhD). Under the three reduction conditions, (*Z*)-**29** formed the desired cyclised products, although the ratios of **2** and **2**-OH were different to those observed with (*Z*)-**10**. Fe^0 reduction yielded 32% of **2** and 35% of **2**-OH, $FeCl_3$/Zn reduction produced 58% of **2** and 15% of **2**-OH, while $NaBH_4$ / Pd/C produced 20% yield of **2** and 56% of **2**-OH (Figure 3.1). Overall, the yield of cyclised products was similar to (*Z*)-**10**, but the proportion of **2**-OH formed was generally higher.

After results with (*Z*)-**29** confirmed that spontaneous cyclisation could occur for aryl amides, the same reduction reactions were conducted with (*Z*)-**1**. Excitingly, all three reactions produced the desired cyclised SU5416 products, with the Fe^0 reaction yielding 51% of **2** and 28% of **2**-OH, the $FeCl_3$/Zn reduction 50% of **2** and 24% of **2**-OH, with $NaBH_4$ / Pd/C 59% of **2** was obtained along with 21% of **2**-OH (Figure 3.1, (*Z*)-**1**). These successful reductive cyclisations with (*Z*)-**1** provided chemical proof-of-concept for the potential dual-activity of the compound *in vivo*, supporting further investigations of its biological activity as a hypoxia-activated tumour-targeted codrug.

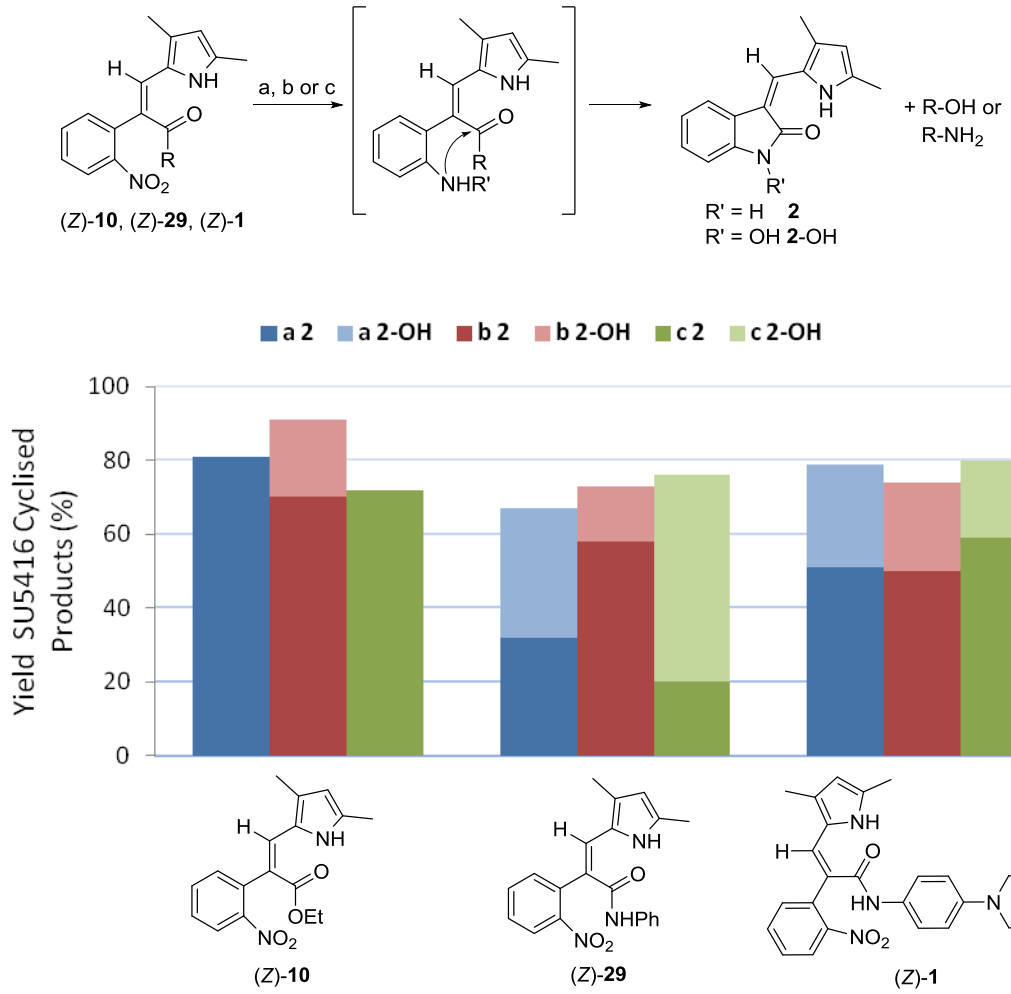

Figure 3.1. Summary of proof-of-concept chemical reduction reactions carried out with (*Z*)-**10**, (*Z*)-**29** and (*Z*)-**1**. Isolated yields of SU5416 cyclised products **2** and **2**-OH are shown. Reduction conditions: a. Fe/CH_3COOH (blue), b. Zn/$FeCl_3$ (red), c. Pd-C/$NaBH_4$ (green).

3.4 Conclusions and Future Directions

Work in this Chapter led to the successful synthesis of a prototype anti-tumour hypoxia-activated codrug (*Z*)-**1**. A summary of the successful synthesis is provided in Scheme 3.5. Overall, the route developed is satisfactory for producing useful quantities of (*Z*)-**1**, where the overall yield of 12% would be expected to give ~3 g of pure (*Z*)-**1** over 7 steps from 10 g of 2-nitrophenylacetic acid.

While the yields of steps (a) and (b) were moderate (71% and 70%, respectively), they were consistent on a multigram scale and the reactions were operationally simple. Recrystallisation from EtOH was successful for both **36** and **34** and no further purification was required. The aryl amine alkylation (b) was one shortcoming in the synthesis, taking at least 4 days to complete. Each of the other 6 steps was completed in less than 15 hours. Alternative reaction conditions, such as use of microwave heating, use of other sources of ethanolamine such as oxirane[203] or ethylene carbonate[204] or the use of a Buchwald-Hartwig aryl cross coupling reaction[205] to produce the key aryl amine moiety from a *p*-halo derivative of amide (*Z*)-**29** could be explored. TBDMS protection in Step (c) was a facile reaction, with recrystallisation from pet. spirit yielding 86% of pure **8** after only 2.0 hours.

The Knoevenagel reaction (d) was the lowest yielding step, producing 41% of (Z)-**7** when performed on 0.5 g scale. Unfortunately, isomerisation of pure (*E*)-**7** to (*Z*)-**7** was not high yielding, although further explorations are certainly recommended. (Z)-**7** was also difficult to purify, requiring careful column chromatography to isolate it from the many streaking reactants and side products. Forming the alkene earlier in the synthesis using **Route 1** would have been preferred, but problems with the acid (*Z*)-**5** precluded this. New chemistry, which forms a higher yield of the desired isomer (*Z*)-**7** from **8** would improve the final yield of (*Z*)-**1** significantly.

Steps (e) to (g) all proceeded well, providing 67% yield of pure (*Z*)-**1** over 3 steps from (*Z*)-**7** with little isomerisation. Gratifyingly, (*Z*)-**1** was an air stable solid at room temperature. While column chromatography steps were utilised here after each step simple extractions may be sufficient to advance the material through before a final chromatography step on (*Z*)-**1**.

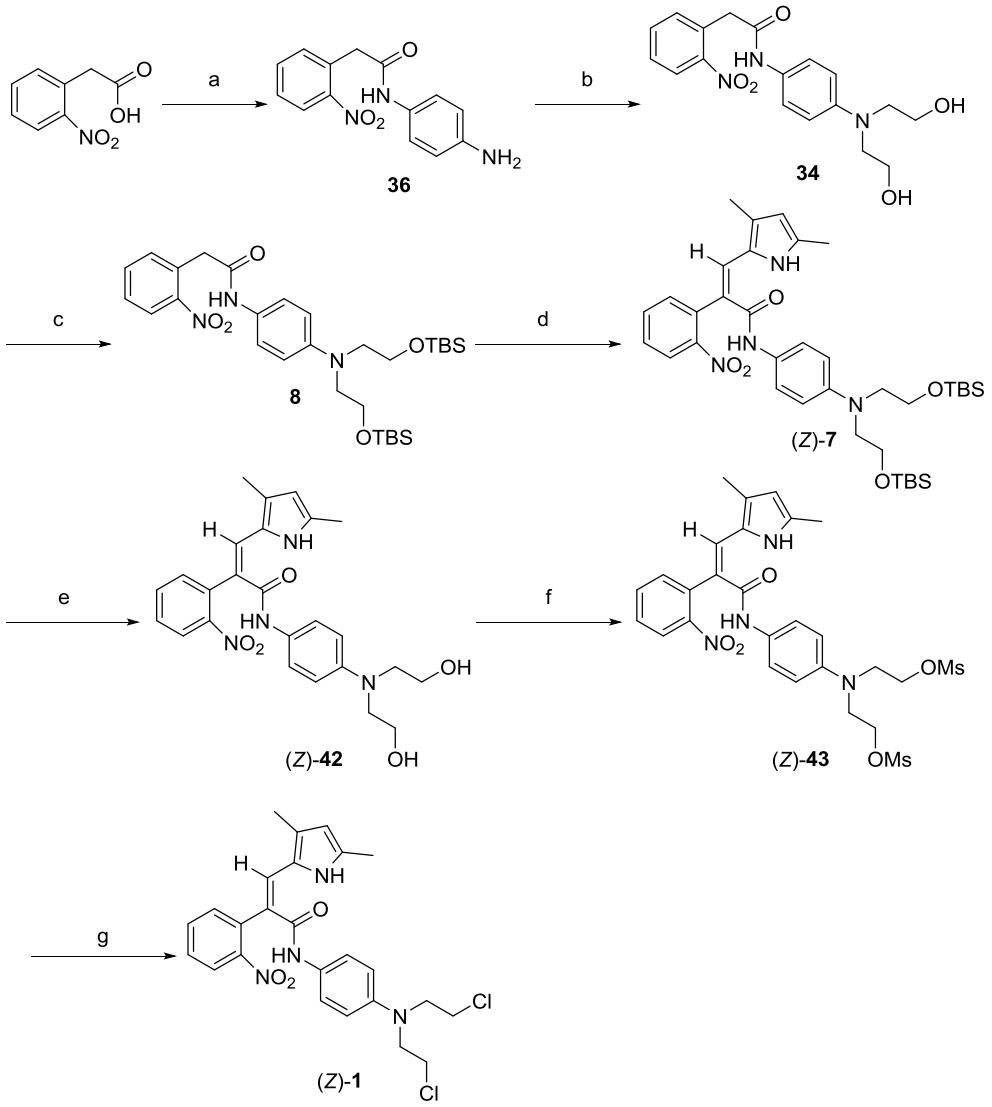

Scheme 3.5. Summary of the successful synthesis of (*Z*)-**1**. Reagents and conditions; a. *p*-phenylenediamine, HBTU, DIPEA, CH_2Cl_2, rt, 4 h, 71%; b. 2-bromoethanol, K_2CO_3, 50 ^oC, 5 days, 70%; c. TBDMSCl, imidazole, CH_2Cl_2, rt, 2 h, 86%; d. **9**, K_2CO_3, 18-crown-6, THF, 65 ^oC, 12 h, (*Z*)-**7** 41%, [+ (*E*)-**7** 22%]; e. 5:1 1.0M TBAF (in THF):AcOH, 0 ^oC to rt, 4 h, 85%; f. MsCl, TEA, CH_2Cl_2, 0 ^oC to rt, 1 h, 86%; g. LiCl (excess), DMF, 75 ^oC, (*Z*)-**1** 92%.

(*Z*)-**1** was shown to produce SU5416 **2** and N-hydroxy-SU5416 **2**-OH upon chemical reduction under standard aryl nitro reduction conditions. This was a key milestone in developing (*Z*)-**1** as it supports proof-of-concept for the dual-action scaffold. This

success suggests that (*Z*)-**1** has potential for hypoxia-selective activation *in vivo* and these investigations are the logical next step. The development of evofosfamide provides a blueprint of experiments for further study here.[167,171] The first experiments on (*Z*)-**1** should confirm selective activation in cell culture by hypoxic tumour cells. A simple protocol would be to perform two cell viability studies with (*Z*)-**1** present, one under normoxic conditions and another with initial incubation under a low concentration of O_2 to activate the scaffold.[171] Hypoxia-selectivity could be further quantified by performing these studies with increasing O_2 gas concentration, which should lower activation of (*Z*)-**1**.[167] These experiments would give a hypoxic-cell selectivity index which could be used to guide further studies on the scaffold.

Other experiments on (*Z*)-**1** would explore its metabolic and plasma stability. These properties could easily be determined with commercially available human/mouse liver microsomes (hLM/mLM) and standard plasma stability assays. Metabolites identified could be used to guide modifications to the structure of (*Z*)-**1** to reduce metabolism. Extensive SAR obtained during the development of sunitinib would provide guidance for predicting the effects of modifications to the aryl NO_2 portion of (*Z*)-**1**.[206,207]

The compound could also be modified to incorporate alternative alcohol or amine containing cytotoxins via ester or amide linkages. The Kelso Lab is currently targeting codrug **45**, incorporating the antimetabolite 5-fluorodeoxyuridine (Floxuridine) as a cytotoxin, linked via a primary alcohol (Figure 3.2).

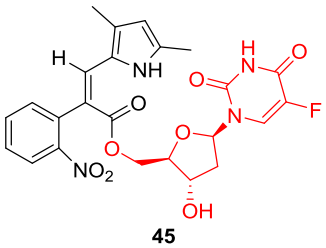

45

Figure 3.2. Structure of codrug **45** currently being pursued in the Kelso Lab.

Chapter 4

Synthesis and Evaluation of 2-Aryl-3*H*-Pyrrolizin-3-ones as Angiogenesis Inhibitors

4.1 Introduction

3*H*-Pyrrolizin-3-one **14** was the major product formed during attempted coupling reactions between (*Z*)-**5** or (*E*)-**5** and several amines and alcohols (Chapter 2.3). Couplings with HBTU/HATU and DIPEA, DCC/EDCI with or without DMAP in a variety of solvents all produced **14** and failed to yield any of the coupled amides/esters. It was proposed that heightened acidity of the pyrrole N-H, arising from its intramolecular H-bond to the carbonyl oxygen, was promoting deprotonation in the presence of DIPEA or carbodiimide coupling reagents and the resulting pyrrolate anion was cyclising onto the activated acid (Chapter 2.3; Figure 4.1(a)). Electron donation from the pyrrole nitrogen into the electron withdrawing 2-nitrophenyl and carboxylate moieties could increase single bond character of the alkenic double bond of (*E*)-**5**, promoting bond rotation and isomerisation from (*E*)-**5** to (*Z*)-**5**, thus facilitating its transformation to **14** under coupling conditions (Chapter 2.4.2; Figure 4.1(b)). Trace quantities of **14** were usually observed during Knoevenagel condensations of 2-nitrophenylacetate allyl ester **12** with pyrrole aldehyde **9** (Chapter 2.2).

(a)

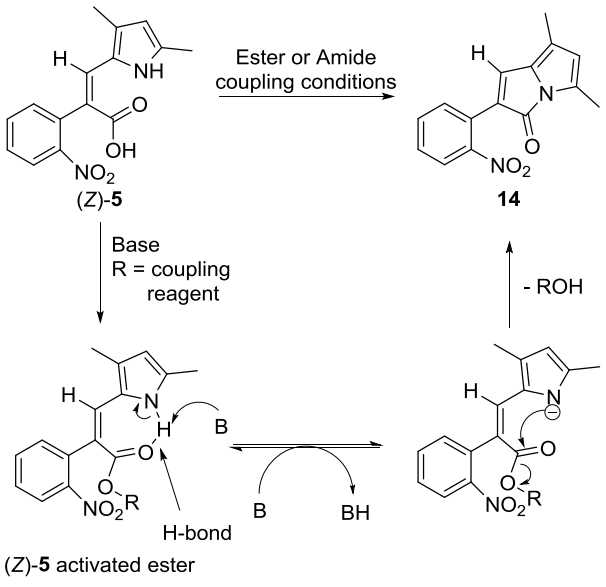

(b)

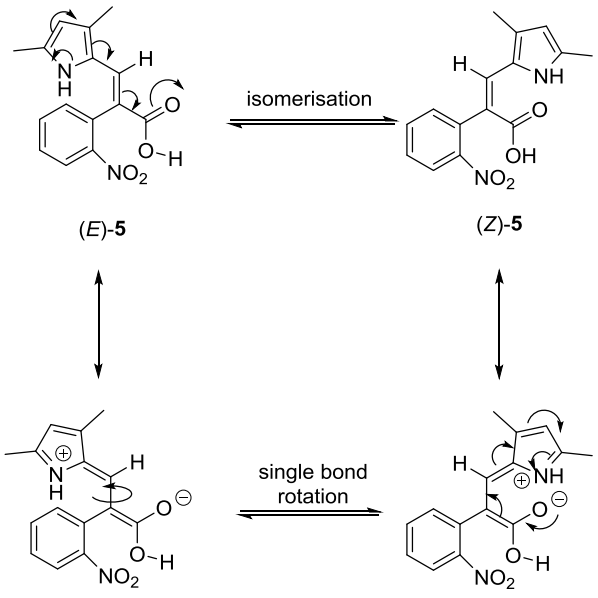

Figure 4.1. (a) Mechanism of formation of 3*H*-pyrrolizin-3-one **14** from (*Z*)-**5** under amide/ester coupling conditions. (b) Explanation for facile isomerisation of (*E*)-**5** to (*Z*)-**5**, which allowed formation of **14** from (*E*)-**5**.

Few 3*H*-pyrrolizin-3-ones have been described in the literature and there is little known about their chemistry or biological activity. A SciFinder Scholar structure search on the 3*H*-pyrrolizin-3-one core returned 277 references (11/06/15). Many of these described tricyclic pyrrolo-indolones, pyrrolo-isoindolones, tetracyclic isoindolo-indolones and other polycyclic heterocycles, rather than simple 3*H*-pyrrolizin-3-ones.[208,209] Several of the structures are marine natural products or their derivatives (Figure 4.2).[210]

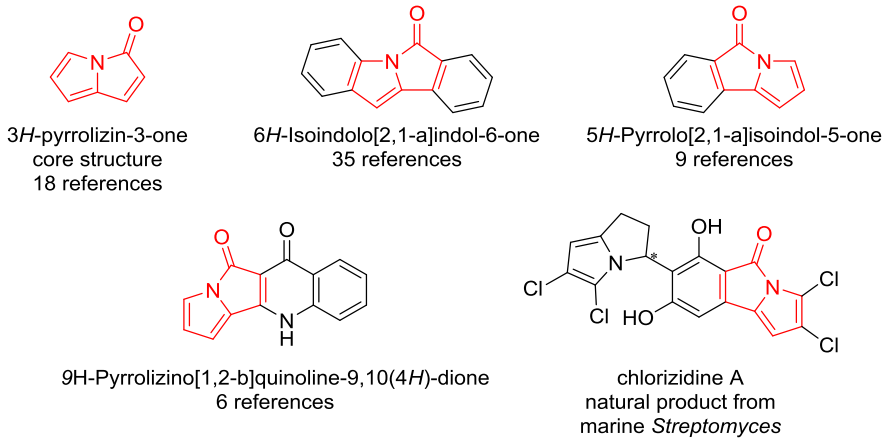

Figure 4.2. 3*H*-pyrrolizin-3-one-containing structures returned from a SciFinder Scholar search.

McNab et al reported the synthesis of an acetoxymethyl-3*H*-pyrrolizin-3-one in 2 steps. The first involved reacting 3-acetoxymethyl-pyrrole-2-carboxaldehyde **46** with Meldrum's acid to form condensation product **47**. Flash vacuum pyrolysis (FVP) of **47** at 600 ^{o}C then produced the 3H-pyrrolizin-3-one **48** (Scheme 4.1).[211–213] FVP requires specialised glassware, high vacuum and high temperatures to carry out reactions. Similar syntheses have been developed by McNab to access other 3*H*-pyrrolizin-3-ones.[213–216]

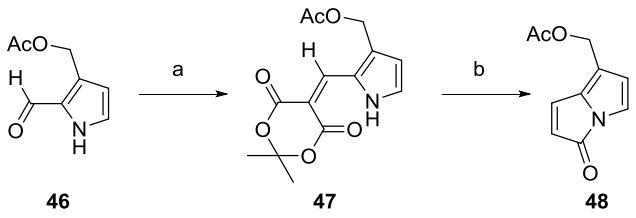

Scheme 4.1. Synthesis of (3-oxo-3H-pyrrolizin-7-yl)methyl acetate **48**.[213] Reagents and conditions: a. Meldrum's acid, piperidinium acetate, 60%; b. FVP 600 ^{o}C, 90%.

4.2 Development of a Divergent Synthesis of 3*H*-Pyrrolizin-3-ones

Discovery of the novel class of angiogenesis inhibitors in Chapter 2 demonstrated that the indolin-2-one ring system of sunitinib and SU5416 was not essential for activity.[217] 3*H*-pyrrolizin-3-ones carrying a pendant aryl ring at the 2-position retain many of the structural features of SU5416 and it was hypothesised that they may also exhibit anti-angiogenic properties. This hypothesis led to exploration of the structure activity relationships of the class as angiogenesis inhibitors.

The synthetic route that had serendipitously led to formation of 3*H*-pyrrolizin-3-one **14** was a four-step process that involved: (1) esterification of 2-nitrophenylacetic acid **11** with allyl alcohol to form **12**, (2) Knoevenagel condensation between **12** and pyrrole aldehyde **9** to form (*Z*)-**13** (with significant formation of (*E*)-**13**), (3) de-allylation of the *cis*-product (*Z*)-**13** with $Pd(PPh_3)_4$ and (4) ring closing acylation of the pyrrole nitrogen under amide coupling conditions. Steps 2-4 required column chromatography to isolate the pure products. This route was considered too long and inefficient for a structure-activity exploration of the anti-angiogenic properties of 2-aryl-3*H*-pyrrolizin-3-ones. A shorter, more divergent approach capable of providing rapid access to multiple 2-aryl-3*H*-pyrrolizin-3-one analogues was desired.

It was proposed that divergent access to the scaffold might be achievable through a one-pot procedure from pyrrole aldehyde **4** and the many commercially available ring-substituted phenylacetic acids. It had already been established that the K^+ salt of aldehyde **4**, generated using KH, was cleanly acylated with chloroformates (Chapter 2.2). We hypothesised that this salt would also react with phenylacetic acids, which had been pre-activated with amide coupling reagents. A procedure was conceived wherein a phenylacetic acid analogue was activated with coupling reagent in one flask and the K^+

salt of **4** generated in a separate flask. Mixing of the two flasks would trigger a cascade of reactions, starting with pyrrole-*N*-acylation, to give intermediate **49** (Scheme 4.2). Abstraction of a benzylic proton under the basic reaction conditions (excess KH) would then trigger an intramolecular Knoevenagel condensation, leading to formation of 3*H*-pyrrolizin-3-ones.

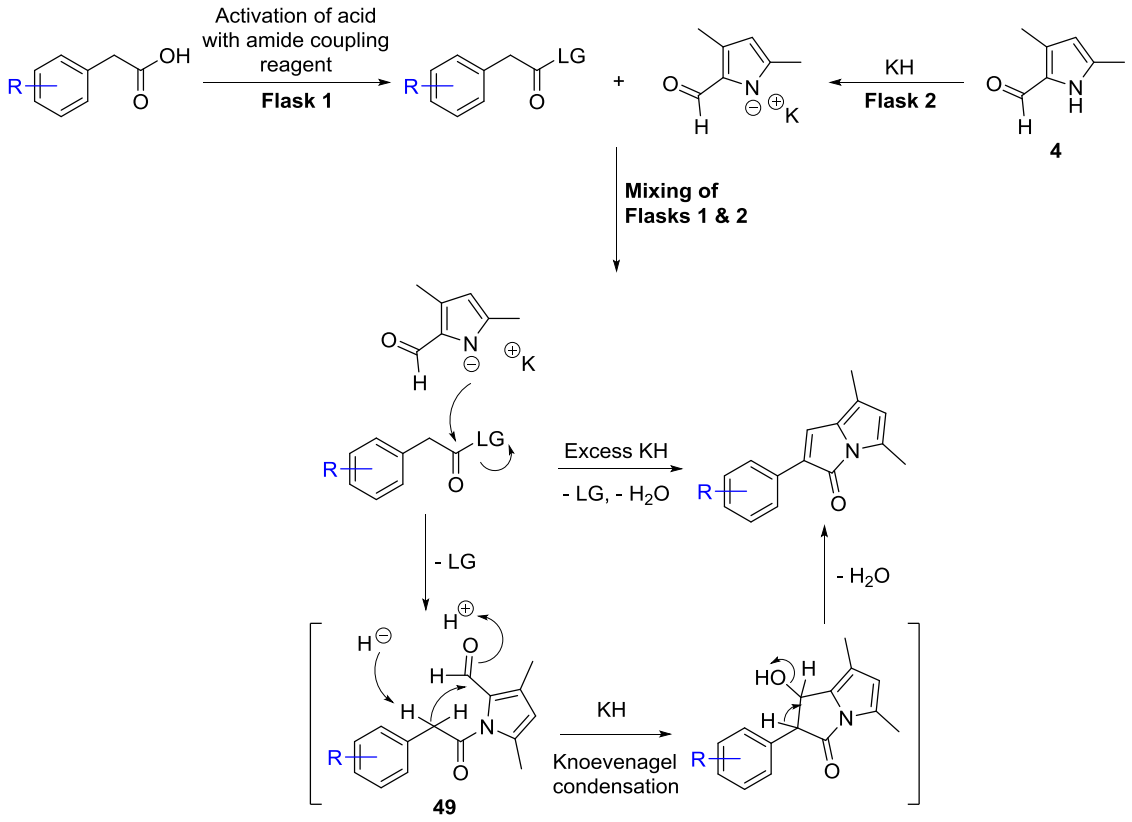

Scheme 4.2. Proposed one-step divergent synthesis of 2-aryl-3*H*-pyrrolizin-3-ones carrying substituents on the phenyl ring. LG = Leaving Group.

The procedure was initially explored using unsubstituted phenylacetic acid **50**, activated as the acid chloride, HOBt ester or carbodiimide derivative in CH_2Cl_2. The potassium salt of **4** was generated using 1.1 mol eq. of KH in THF. Reactions using carbodiimide coupling reagent DCC with 10% w/w 4-(dimethylamino)pyridine (DMAP) produced 24% of the desired dark red 3*H*-pyrrolizin-3-one **51**. Replacing KH with 1.1 mol eq. of

KO^tBu reduced the yield to 18% (Table 4.1 entries 1 and 2). Use of the carbodiimide reagent EDCI produced **51** in 17% yield (Table 4.1, Entry 3).

Activation of **50** to the HOBt ester with HBTU/DIPEA showed more promise (37% yield, Table 4.1, Entry 4) and was explored further. Substitution of HBTU with HATU reduced the yield to 23%. The HOBt ester was formed using standard amide coupling conditions, where 2 mol eq. of DIPEA and 1 mol eq. of HBTU were used and stirred at RT in CH_2Cl_2. The potassium salt of pyrrole **4** was formed separately using 1.1 mol eq. of KH at 0 ^oC in THF. Rapid addition of the HOBt ester solution to the pyrrolate solution led to formation of the desired product **51**. It was noted that slower addition or reverse addition resulted in slower reactions and lower yields.

Exploration of the number of mol eq. of KH present in the reaction was studied in the Kelso lab by a German exchange student Claudia Ries in 2012. She identified that 2.0 mol eq produced the highest yield of **51** (48%, Table 4.1, Entry 6). Under these conditions, 1.0 mol eq. of KH was generating the potassium salt of **4** and the second 1.0 mol eq. was presumably acting to trigger the Knoevenagel condensation after mixing the two flasks and following pyrrole *N*-acylation. Changing from 2.0 mol eq. of KH to 2.0 mol eq. of potassium hexamethyldisilazane (KHMDS) or KO^tBu under the conditions identified by Claudia reduced the yield to 38% in both cases (Table 4.1, Entries 7 and 8). Use of phenylacetyl chloride in place of the activated ester of **50** resulted in a 32% yield of **51**. The yield, however, was not reproducible and the reactions were much less convenient to carry out.

It appeared that the yield was approaching a maximum of only 50%. One reason for this may have been the presence of the conjugate acid of DIPEA (formed during HOBt ester formation in Flask 1). It is likely that a significant portion of hydride was being lost as

H_2 gas through deprotonation of DIPEA.H^+. This would leave less than 1.0 mol eq. of hydride available for the intramolecular Knoevenagel reaction, thereby reducing the yield.

Table 4.1. Reactions and conditions explored for the one-pot synthesis of 3*H*-pyrrolizin-3-one **51**.

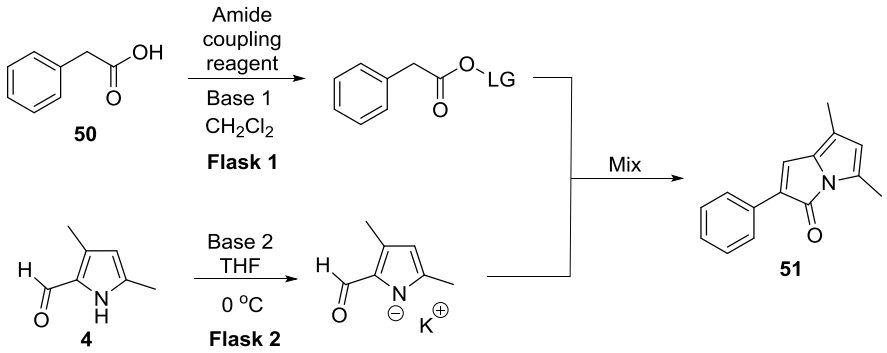

Entry	Coupling Reagent*	Base 1 (mol. eq)[#]	Base 2 (mol. eq)[+]	Yield **51** (%)
1	DCC	DMAP (0.1)	KH (1.1)	24
2	DCC	DMAP (0.1)	KO^{t}Bu (1.1)	18
3	EDCI	DMAP (0.1)	KH (1.1)	17
4	HBTU	DIPEA (2.0)	KH (1.1)	37
5	HATU	DIPEA (2.0)	KH (1.1)	23
6	HBTU	DIPEA (2.0)	KH (2.0)	48
7	HBTU	DIPEA (2.0)	KHMDS (2.0)	38
8	HBTU	DIPEA (2.0)	KO^{t}Bu (2.0)	38

* Reactions were carried out using 1.0 mol eq. of phenylacetic acid **50** with 1.1 mol eq. of amide coupling reagent at RT and Base 1 and 1.0 mol eq. of pyrrole aldehyde **4** with Base 2 in THF at 0 ^{o}C.
[#] relative to **4**
[+] relative to **4**

The highest yield obtained for **51** was 48% using 1.1 mol eq. HBTU and 2.0 mol eq. DIPEA to activate 1.0 mol eq. phenylacetic acid **50** to the HOBt ester in Flask 1, and 2.0 mol eq. of KH to activate 1.0 mol eq. pyrrole aldehyde **4** to its potassium salt in

Flask 2, before pouring Flask 1 into Flask 2 in one portion. Yield improvements may be possible through use of an alternative activation process in Flask 1 that does not produce DIPEA.H^+ (e.g. use of hydride as base), although this was not explored. Nevertheless, the reaction was suitable for the synthesis of small quantities of pure 2-aryl-3*H*-pyrrolizin-3-ones for the SAR study. Accordingly, analogues carrying substituents at the phenyl *ortho*, *meta* and *para* positions were pursued using this chemistry with pyrrole aldehyde **4** and commercially acquired, ring-substituted phenylacetic acids.

4.3. Synthesis of 2-Aryl-3*H*-Pyrrolizin-3-one Analogues

Mono-substituted fluorophenyl (**52**-**54**), chlorophenyl (**55**-**57**), bromophenyl (**58**-**60**), tolyl (**61**-**63**), methoxyphenyl (**64**-**66**), and nitrophenyl acetic acids (**11**, **67**-**68**) were acquired from Sigma Aldrich and submitted to the optimised procedure (Table 4.2). The reactions and product purification proceeded smoothly in most cases. The reactions were generally complete in less than 4 hours, after which they were evaporated to dryness, taken up in Et_2O and washed with saturated sodium bicarbonate and brine, before being dried over anhydrous $MgSO_4$ and concentrated. The crude products were purified by silica gel column chromatography using mixtures of pet. spirit and acetone as eluents. Visualisation of the products was possible during column chromatography due to their deep red or maroon colour, simplifying the procedure.

The reactions were performed on 200-500 mg scale and the yields obtained were between 4% and 48%. Phenylacetic acids with larger *ortho*-substituents provided the lowest yields of 2-aryl-3*H*-pyrrolizin-3-ones (e.g. *o*-bromophenyl **75** 13%, *o*-chlorophenyl **72** 16% and *o*-tolyl **78** 21%; c.f. *o*-fluorophenyl **69** 37%, Table 4.2) This

may have been due to steric hindrance hampering the Knoevenagel reaction at the neighbouring benzylic position. *Meta*-substituted products were obtained in the highest yields (e.g. *m*-fluorophenyl **70** 37%, *m*-chlorophenyl **72** 35% and *m*-bromophenyl **76** 44%; Table 4.2). *Para*-substituted products were also produced in reasonable yields (e.g. *p*-fluorophenyl **71**, *p*-chlorophenyl **74** and *p*-bromophenyl **77** were synthesised in 38%, 30% and 34% yields, respectively; Table 4.2).

Electron-withdrawing substituents that increased acidity at the benzyl position resulted in lower yields (e.g. 28% and 4% yield for *o*-nitro **14** and *p*-nitro **85**, respectively). Electron donating substituents appeared to favour the reaction. *o*-Methoxyphenyl derivative **81** was the second highest yielding *ortho*-substituted 3*H*-pyrrolizin-3-one at 45% (Table 4.2. Entry 14). One possible explanation for these results is that activated acids with more acidic benzylic protons favoured neutralisation of the potassium pyrrolate salt over acylation.

Table 4.2. Synthesis of 2-aryl-3*H*-pyrrolizin-3-ones.

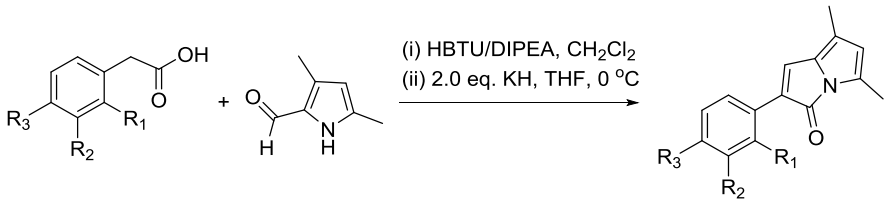

11, 50, 52-68 **4** **14, 51, 69-85**

Entry	Phenylacetic acid	R_1	R_2	R_3	Product	Yield, %
1	**50**	H	H	H	**51**	48
2	**52**	F	H	H	**69**	37
3	**53**	H	F	H	**70**	37
4	**54**	H	H	F	**71**	38
5	**55**	Cl	H	H	**72**	16
6	**56**	H	Cl	H	**73**	35
7	**57**	H	H	Cl	**74**	30
8	**58**	Br	H	H	**75**	13
9	**59**	H	Br	H	**76**	44
10	**60**	H	H	Br	**77**	34
11	**61**	Me	H	H	**78**	21
12	**62**	H	Me	H	**79**	41
13	**63**	H	H	Me	**80**	37
14	**64**	OMe	H	H	**81**	33
15	**65**	H	OMe	H	**82**	45
16	**66**	H	H	OMe	**83**	30
17	**11**	NO_2	H	H	**14**	28
18	**67**	H	NO_2	H	**84**	15
19	**68**	H	H	NO_2	**85**	4

4.4 Biological Assessment of Mono-Substituted 2-Aryl-3*H*-pyrrolizin-3-ones

4.4.1 HUVEC Tube Formation Assay

Anti-angiogenesis activity of the nineteen 3*H*-pyrrolizin-3-ones was examined using a semi-quantitative, cell-based endothelial tube formation assay with human umbilical vein endothelial cells (HUVECs).[218] HUVECs extracted from umbilical veins are commonly used for models of angiogenesis as they are easy to culture and sensitive to growth factors, such as EGF and FGF. Matrix-cultured HUVECs differentiate in response to growth factors, becoming elongated and motile and able to self-organise into capillary-like structures over a period of 2-12 hours. This process is disrupted by small molecule RTK inhibitors of angiogenesis, making it a convenient model for measurements of angiogenesis inhibition.[219] Representative time-lapse images showing various stages of pro-angiogenic tube formation by EA.hy926 cells (HUVEC/A549 hybrid cell line) are shown in Figure 4.3.[218]

Quantification of angiogenesis and the inhibitory effects of compounds uses the method reported by Aranda et al.[218] An image of the cells is captured and the cells are tallied and categorised as ellipsoid (i.e. undifferentiated, Figure 4.3. Image 1), sprouting (i.e. differentiating, Figure 4.3, Image 2) or connected to other cells (Figure 4.3, Images 3 and 4). The total number of closed polyhedra (Figure 4.3, Images 5 and 6) are also counted, along with 'complex meshes', which are polyhedra containing walls more than 2 cells thick (Figure 4.3, Images 7 and 8).

The numerator of an equation is calculated by summing the number of sprouting cells and the number of connected cells multiplied by a factor of 2 and the number of polygons multiplied by a factor of 3. The denominator of the equation is the total number of cells, including undifferentiated cells.[218] Finally, a correction factor is added

to account for ‘complex meshes’, which represent extensive angiogenesis. A score of 0 is added for no complex meshes, 1 for at least one polyhedra with walls of 2-4 cells thick or 2 for at least one polyhedra with walls of 4+ cells thick.

Assays were conducted with adherent HUVEC cells (C-003-5C, Life Technologies), cultured according to the manufacturer’s specifications in 75 cm^3 flasks and utilised between passages 2-4. Tube formation was monitored in Geltrex matrix (Life Technologies) according to manufacturer’s specifications in standard flat-bottomed plates using a 24 well format. The cells were seeded at 3.5–4.5× 10^4 cells per Geltrex-coated well and incubated for 2 hours at 37 ^oC in 5% CO_2/air. Compounds were solubilised in DMSO to form stock solutions at 100 µM. Aliquots were added to each well to give a final concentration of 10 µM with 1% DMSO. After 8 hours, the media was removed and replaced with sterile PBS buffer prior to imaging by light microscopy. Three to six images were taken and scored for each well over two independent assays, giving a total of 6-10 counts for each compound. 1% DMSO was used as a negative control (vehicle) and 10 µM sunitinib as a positive control (inhibition). Angiogenesis was indicated by the angiogenesis score relative to the negative control (vehicle) i.e. a low angiogenesis score indicates a potent inhibitor of angiogenesis.

(a)

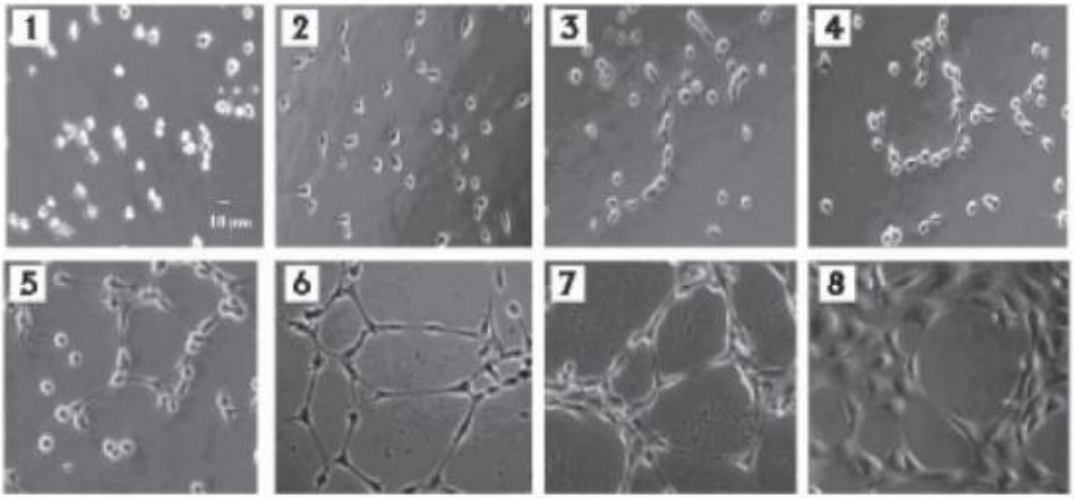

(b)

$$Score = (0, 1\ or\ 2) + \frac{[(sprouting\ cells)1 + (connected\ cells)2 + (polygons)3]}{total\ cell\ count}$$

Figure 4.3. (a) Representative images of EA.hy926 cells during the angiogenic tube formation process.[218] (b) Equation used to calculate angiogenesis score.[218]

The assay showed that the original ortho-NO_2-substituted analogue **14** was the most potent angiogenesis inhibitor and that most other substitutions were not well-tolerated. Compound **14** produced a score that was 29.7% ± 4.1 of the angiogenesis score observed with vehicle at 10 μM and 74.0% ± 12.6 of the vehicle score at 1 μM. The next most potent compounds were the unsubstituted phenyl derivative **51** (68.4% ± 6.6 of vehicle) and 2-fluorophenyl **69** (67.2% ± 6.2 of vehicle). The *o*-methoxyphenyl **81**, *o*-bromophenyl **75** and *o*-tolyl **78** analogues produced modest reductions in angiogenesis. All other derivatives were essentially inactive. The positive control sunitinib totally arrested angiogenesis at 10 μM under the assay conditions.

(a)

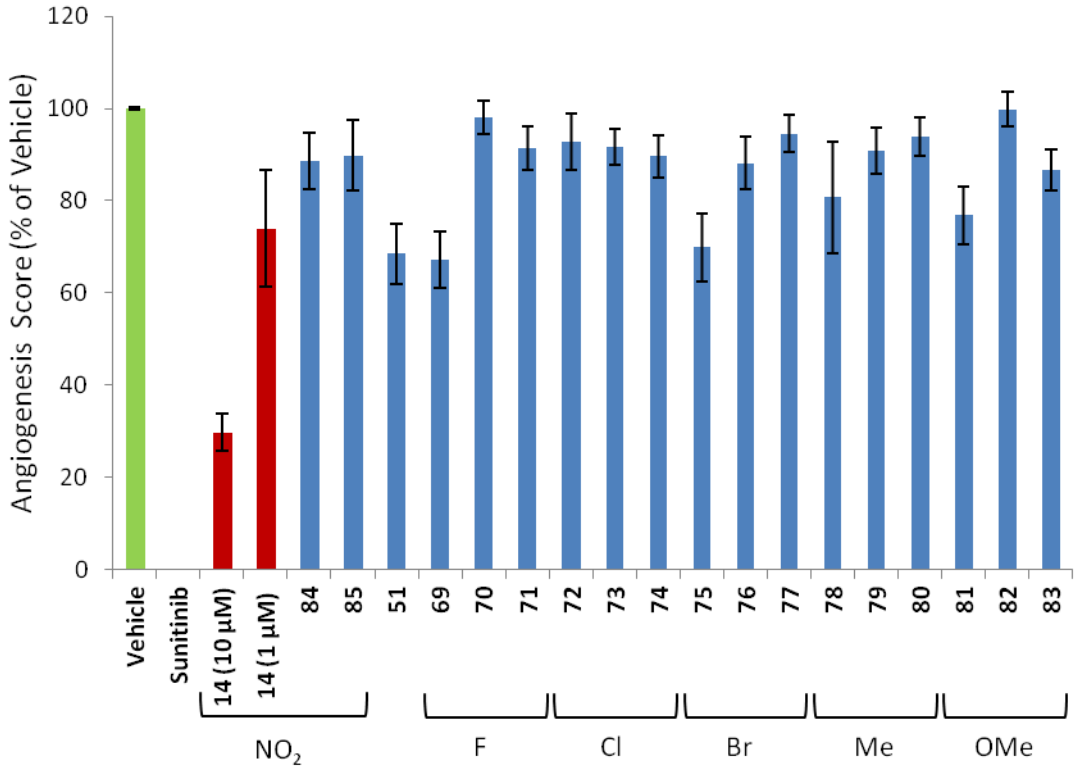

(b)

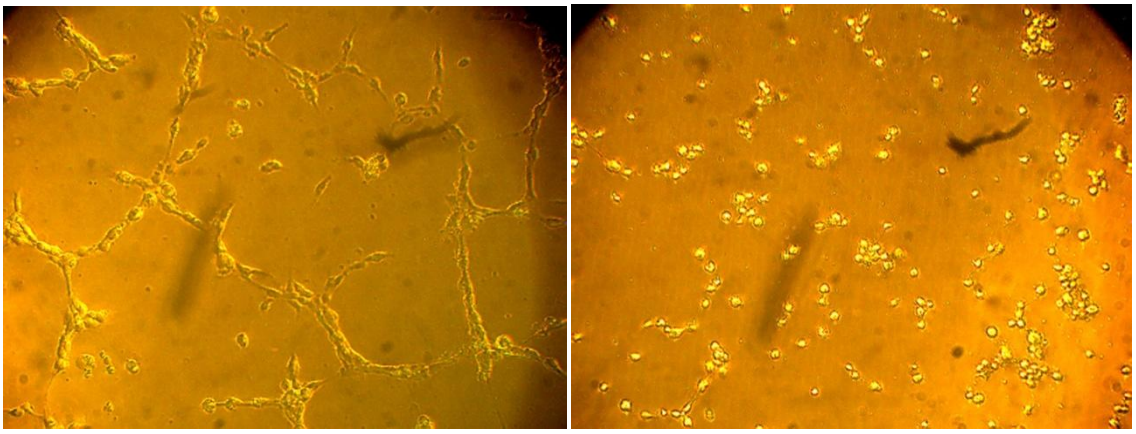

Figure 4.4. (a). Inhibition angiogenesis in an endothelial tube formation assay by 2-aryl-3*H*-pyrrolizin-3-one derivatives and controls. Compounds were present at 10 µM. Data for **14**, the most potent compound, is shown in red and is also provided at 1 µM. (b) Representative images showing degree of angiogenesis evident with the 2-fluorophenyl analogue **69** (left) and the more potent inhibitor **14** (right, both compounds present at 10 µM).

4.4.2. Rat Aortic Ring Angiogenesis Assay

The two most potent angiogenesis inhibitors 2-(2-nitrophenyl)-3*H*-pyrrolizin-3-one **14** and 2-phenyl-3*H*-pyrrolizin-3-one **51** were submitted to the more physiologically relevant (though more expensive and labour intensive) rat aortic ring angiogenesis assay to confirm their angiogenesis inhibition activities (see Chapter 2.7 for assay details).

Compound **14** showed a similar inhibitory potency to the SU5416 in the assay, producing 4% F.O.V. occupancy at 10 µg/mL (c.f. 10% for SU5416 at 10 µg/mL). Compound **14** also showed a dose-dependent response, producing 1% F.O.V. occupancy at 100 µg/mL. The unsubstituted phenyl derivative **51** potently inhibited angiogenesis at 10 µg/mL (12% F.O.V. occupancy) but solubility issues similar to those of SU5416 **2** (see Chapter 2.7) appeared to interfere with its activity at the higher concentration of 100 µg/mL (21% F.O.V. occupancy). These results corroborated those observed in the endothelial tube formation assay, confirming that **14** and **51** are new anti-angiogenic leads.

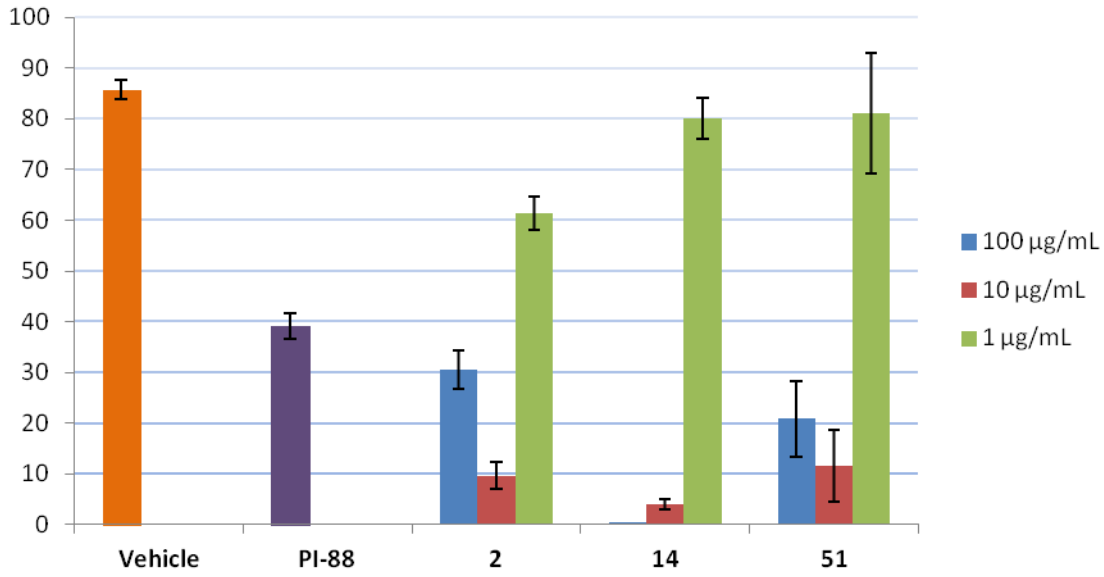

Figure 4.5. Rat aortic ring angiogenesis inhibition assay.

4.5 Conclusions and Future Directions

The chemistry and biological activity of the serendipitously discovered 2-aryl-3*H*-pyrrolizin-3-one **14** and related analogues was investigated in this chapter. The crystal structure of **14** was determined by X-ray analysis, revealing a preferred orientation where the carbonyl oxygen makes a favourable interaction with the NO_2 nitrogen (Chapter 2.3). The 2-nitrophenyl-3*H*-pyrrolizin-3-one **14** was shown to be a potent inhibitor of angiogenesis in both the endothelial tube formation assay (29.7% of vehicle angiogenesis at 10 μM) and the rat aortic ring angiogenesis assay (4% F.O.V. occupancy at 10 μg/mL).

A divergent synthesis of analogues of **14** was developed using commercially available mono-substituted phenylacetic acids and pyrrole aldehyde **4**. While usable quantities of all analogues were obtained there is much scope for improving the yields. Eighteen analogues of **14** were synthesised and tested for anti-angiogenic properties in the endothelial tube formation assay. Compound **14**, the ortho-fluoro compound **69** and unsubstituted phenyl derivative **51** showed the strongest inhibition of angiogenesis, while the other analogues were essentially inactive. Based on the results from this assay, compounds **14** and **51** were advanced to the more sophisticated and physiologically relevant rat aortic ring angiogenesis assay to confirm their anti-angiogenic properties. Both compounds showed strong inhibitory effects in this assay, confirming that 2-aryl-3*H*-pyrrolizin-3-ones represent a new class of angiogenesis inhibitors.

There are several biochemical pathways that affect angiogenesis. Screening **14** and **51** against a panel of angiogenesis-modulating RTKs would shine light on the specific target(s) of the compounds. X-ray or docking studies with the compounds with any

inhibited receptors would be vital for supporting lead optimisation studies. Key receptors to test against would be the VEGFR and EGFR families of RTKs.

Very little is known about the chemistry of 2-aryl-3*H*-pyrrolizin-3-ones like **14** and **51**. Derivatisation at the β-alkene position could be interesting for continuing angiogenesis inhibitor development since modifications at the phenyl ring appeared to be poorly tolerated. Work from the McNab lab identified reactivity at this position, suggesting it may be possible to introduce nucleophiles directly onto **14** and **51**.[215] Introducing a stereocentre in this manner would generate interesting SAR information.

Chapter 5

Experimental

5.1 General

Reagents and solvents were used without further purification unless otherwise stated. Dichloromethane (CH_2Cl_2), dimethylformamide (DMF), toluene and diethyl ether (Et_2O) were used directly from a PureSolv Solvent purification system. THF was purified by drying over KOH before distillation from sodium benzophenone ketyl. Compounds were weighed using a Sartorius Extend 220g or OHaus Adventurer balance. Solvents were removed under reduced pressure (*in vacuo*) at rt - 40 ^{o}C using a Heidolph or Büchi rotary evaporator with Vacuubrand pumps. Solvent residues were removed *in vacuo* using a Javac Vector RD-90 double stage high vacuum pump. Analytical thin layer chromatography (TLC) analysis was performed using Merck 0.2 mm silica gel 60 F254 coated aluminium plates. Compounds were visualised on TLC plates under UV light (254 nm). Column chromatography was performed on Merck silica gel 60 (230-400 mesh). Low resolution electrospray (ESI) mass spectra were obtained using a Shimadzu LCMS-2010EV spectrometer. ESI High Resolution Mass Spectra (HRMS) were obtained on a Xevo QToF mass spectrometer with perfluorokerosene as internal standard. Fourier-Transform Infrared (FTIR) spectra were obtained using a Shimadzu IRAffinity-1 spectrometer with a MIRacle 10 accessory. ^{1}H, ^{13}C and two-dimensional (2D) NMR experiments were performed using a Varian Inova 500 MHz or Varian Premium Shielded 500 MHz spectrometer at 25 ^{o}C. Chemical shifts are reported as δ (ppm) relative to internal TMS (^{1}H) or solvent (^{13}C) unless stated otherwise. The abbreviations s = singlet, d = doublet, t = triplet, q = quartet, dd = doublet of doublets, m = multiplet and br s = broad singlet are used throughout.

5.2 Compound Characterisation

(E)-2-(3,5-dimethyl-1H-pyrrol-2-yl)-3-((4-(dimethylamino)phenyl)imino)-3H-indole 1-oxide **15**

To a solution of (*E*)-**5** (201 mg, 0.70 mmol) in CH_2Cl_2 (10 mL) was added HATU (372 mg, 0.98 mmol). The solution was stirred at room temperature for 5 minutes before adding *N*,*N*-dimethyl-*p*-phenylenediamine (DMPD, 95.3 mg, 0.70 mmol) in one portion. The reaction was then stirred at room temperature and monitored by TLC analysis (3:7 EtOAc:pet. spirit). After 3 h, the mixture was extracted with EtOAc (3 x 25 mL) and the combined organic phase washed with brine (2 x 25 mL), dried over anhydrous $MgSO_4$ and concentrated. The residue was purified by column chromatography (100% pet. spirit to 8:2 pet. spirit:EtOAc) to give **15** (100 mg, 40% yield) as a dark purple solid. Use of the same procedure with (*Z*)-**5** resulted in similar yields of **15**.

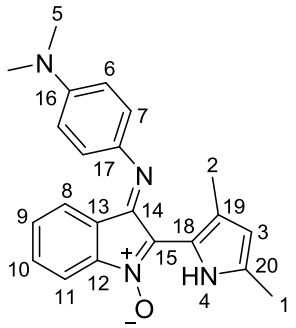

15

M.P. 146-148 ^{o}C. ^{1}H NMR ($CDCl_3$, 500 MHz): δ 2.33 (s, 3H, H_1), 2.51 (s, 3H, H_2), 3.04 (s, 6H, H_5), 5.96 (d, 1H, *J* = 3.0 Hz, H_3), 6.80 (d, 2H, *J* = 8.5 Hz, H_6), 7.05 (d, 2H, *J* = 9.0 Hz, H_7), 7.08 (t, 1H, *J* = 7.5, H_9), 7.12 (d, 1H, *J* = 7.5, H_8), 7.45 (t, 1H, *J* = 7.5 Hz, H_{10}), 7.63 (d, 1H, *J* = 7.5 Hz, H_{11}), 11.86 (s (br), 1H, H_4). ^{13}C NMR ($CDCl_3$, 126 MHz): δ 13.5 (C_1), 16.5 (C_2), 40.7 (C_5), 112.6 (C_6), 112.7 (C_{15}), 112.9 (C_{11}), 113.7 (C_3), 117.0 (C_{18}), 119.0 (C_{13}), 121.5 (C_7), 123.7 (C_8), 128.0 (C_9), 128.5 (C_{19}), 131.8 (C_{10}), 132.3 (C_{20}), 139.3 (C_{17}), 147.9 (C_{12}), 149.2 (C_{16}), 154.8 (C_{14}). HRMS-ESI: *m/z* calcd for $C_{22}H_{23}N_4O$ [$M+H^+$] 359.1872; observed 359.1868. FTIR: neat (cm^{-1}) 2920, 2340, 1730, 1595, 1521, 1448, 1350, 1277, 1205, 1185, 1117.

(E)-3-((4-aminophenyl)imino)-2-(3,5-dimethyl-1H-pyrrol-2-yl)-3H-indole 1-oxide **16**

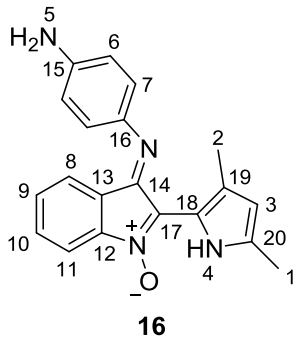

16

Use of *p*-phenylenediamine in place of *N*,*N*-dimethyl-*p*-phenylenediamine in the procedure described for producing **15** afforded **16** (56% yield) as a dark amorphous solid. ^{1}H NMR* ($CDCl_3$, 500 MHz): δ 2.32 (s, 3H, H_1), 2.51 (s, 3H, H_2), 3.70 (v. br, 2H, H_5), 5.95 (s, 1H, H_3), 6.76 (d, 2H, *J* = 8.5 Hz, H_6), 6.90 (d, 2H, *J* = 8.5 Hz, H_7), 6.95 (d, 1H, *J* = 7.5 Hz, H_8), 7.05 (t, 1H, *J* = 7.5 Hz, H_9), 7.43 (t, 1H, *J* = 7.5 Hz, H_{10}), 7.60 (d, 1H, *J* = 7.5 Hz, H_{11}), 11.79 (br s, 1H, H_4). ^{13}C NMR ($CDCl_3$, 126 MHz): δ 13.4 (C_1), 16.4 (C_2), 113.0 (C_{11}), 113.8 (C_3), 115.6 (C_6), 117.0 (C_{18}), 118.8 (C_{13}), 120.69 (C_7), 124.1 (C_8), 127.7 (C_9), 128.8 (C_{19}), 132.0 (C_{10}), 132.6 (C_{20}), 134.1 (C_{17}), 141.4 (C_{16}), 144.7 (C_{15}), 148.0 (C_{12}), 156.1 (C_{14}). HRMS-ESI: *m/z* calcd for $C_{20}H_{19}N_4O$ [$M+H^+$] 331.1553; observed 331.1551. * NMR peaks were taken from an impure sample due to the compound's instability. Melting point and coherent FTIR data could not be obtained due to the compound's instability.

2-(3,5-dimethyl-1H-pyrrol-2-yl)-3-oxo-3H-indole 1-oxide **17**

To a solution of 0.05 g **15** or **16** (0.14 mmol or 0.15 mmol, respectively) in THF (2 mL) was added 2 mL of 1 M HCl. The reaction was stirred at rt and monitored by TLC analysis (7:3 pet. spirit:EtOAc). After 30 minutes, the mixture was extracted with EtOAc (2 x 25 mL). The combined organic phase was washed with saturated $NaHCO_3$ (2 x 30 mL) and brine (2 x 30 mL), dried anhydrous $MgSO_4$ and concentrated to give **17** (quantitative) as a deep violet solid.

M.P. 158-160 ^{o}C. ^{1}H NMR ($CDCl_3$, 500 MHz): δ 2.32 (s, 3H, H_1), 2.50 (s, 3H, H_2), 5.97 (s, 1H, H_3), 7.36 (t, 1H, *J* = 7.5 Hz, H_6), 7.52 (m, 2H, $H_{5,8}$), 7.60 (t, 1H, *J* = 7.5 Hz, H_7),

11.64 (br s, 1H, H_4). ^{13}C NMR ($CDCl_3$, 126 MHz): δ 13.5 (C_1), 15.0 (C_2), 112.8 (C_8), 114.4 (C_3), 117.1 (C_{13}), 121.9 (C_5), 122.4 (C_{10}), 129.0 (C_6), 129.3 (C_{14}), 129.7 (C_{12}), 133.6 (C_{15}), 135.2 (C_7), 148.8 (C_9), 185.3 (C_{11}). HRMS-ESI: *m/z* calcd for $C_{14}H_{13}N_2O_2$ $[M+H^+]$ 241.0972; observed 241.0972. FTIR: neat (cm^{-1}) 3281, 2918, 1727, 1576, 1522, 1461, 1458, 1370, 1329, 1265, 1208, 1117, 1065.

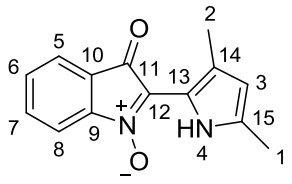

17

*(E)-3,5-dimethyl-2-(2-nitrostyryl)-1H-pyrrole **18***

Compound **18** was isolated as a trace product from the reactions used to produce **16** and by rt storage of (*Z*)-**5** in $CDCl_3$ over 2 weeks.

M.P. and FTIR not recorded due to scarcity and lack of purity of product. ^1H NMR ($CDCl_3$, 500 MHz): δ 2.16 (s, 3H, H_1), 2.29 (s, 3H, H_2), 5.79 (s, 1H, H_3), 6.97 (d, 1H, *J* = 16.1 Hz, H_5), 7.04 (d, 1H, *J* = 16.1 Hz, H_6), 7.27 (t, 1H, *J* = 7.5 Hz, H_9), 7.53 (t, 1H, *J* = 7.5 Hz, H_8), 7.74 (d, 1H, *J* = 8.0 Hz, H_7), 7.90 (d, 1H, *J* = 8.0 Hz, H_{10}). ^{13}C NMR ($CDCl_3$, 126 MHz): δ 11.1 (C_1), 13.2 (C_2), 110.3 (C_3), 113.0 (C_6), 122.2 (C_5), 123.3 (C_{13}), 123.9 (C_{15}), 125.0 (C_{10}), 125.6 (C_{14}), 126.2 (C_9), 126.7 (C_7), 131.1 (C_{12}), 132.83 (C_8), 133.8 (C_{11}). HRMS-ESI: *m/z* calcd for $C_{14}H_{15}N_2O_2$ $[M+H^+]$ 243.1128; observed 243.1131.

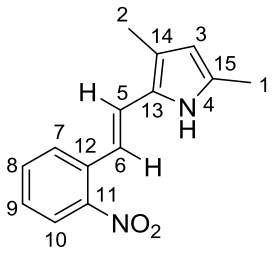

18

*(Z)- and (E)-3-(3,5-dimethyl-1H-pyrrol-2-yl)-2-(2-nitrophenyl)-N-phenylacrylamide (Z)-**29** and (E)-**29***

To a dry round-bottom flask under N_2 was added 2-(2-nitrophenyl)-N-phenylacetamide **23** (1.104 g, 4.31 mmol), oven-dried anhydrous K_2CO_3 (0.893 g, 6.46 mmol), 18-

crown-6 (1.139 g, 4.31 mmol) and dry THF (20 mL). After stirring at 70 ^{o}C for 1 h a brown to dark blue solution appeared. 1-methoxycarbonyl-5-dimethyl-1*H*-pyrrole-2-carboxaldehyde **9** (0.820 g, 4.52 mmol. Prepared as per Sudta, et al.)[217] dissolved in dry THF (8 mL) was added dropwise over 15 minutes and the mixture stirred at 70 ^{o}C for a further 10 h. The reaction was quenched with water (30 mL) and evaporated to dryness. The residues were taken up in EtOAc (50 mL) and washed with saturated $NaHCO_3$ (2 x 50 mL) and brine (2 x 50 mL), dried over anhydrous $MgSO_4$ and concentrated. The crude product was purified by silica gel column chromatography (100% pet. spirit to 8:2 pet. spirit:acetone) to provide (*Z*)-**29** (0.591 g, 38% yield) as an orange-red solid, (*E*)-**29** (0.405, 26% yield) as a red oil and trace quantities of *N*-phenyl-SU5416 **33** (typically 2-5% yield).

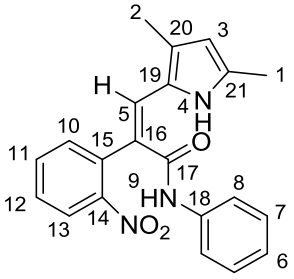

(*Z*)-**29**

(*Z*)-**29**. Red crystalline solid. M.P. 177-179 ^{o}C. ^{1}H NMR ($CDCl_3$, 500 MHz): δ 2.12 (s, 3H, H_1), 2.32 (s, 3H, H_2), 5.86 (s, 1H, H_3), 6.56 (s, 1H, H_5), 6.87 (br s, 1H, H_9), 7.12 (t, 1H, J = 7.5 Hz, H_6), 7.32 (t, 2H, J = 7.5 Hz, H_7), 7.37 (t, 2H, J = 7.5 Hz, H_8), 7.56 (t, 1H, J = 8.0 Hz, H_{12}), 7.60 (d, 1H, J = 8.0 Hz, H_{10}), 7.71 (t, 1H, J = 8.0 Hz, H_{11}), 8.03 (d, 1H, J = 8.0 Hz, H_{13}), 12.00 (br s, 1H, H_4). ^{13}C NMR ($CDCl_3$, 126 MHz): δ 11.4 (C_1), 13.6 (C_2), 111.1 (C_3), 115.6 (C_{16}), 121.4 (C_8), 124.1 (C_{18}), 124.9 (C_6, C_{13}), 129.0 (C_7), 129.1 (C_{12}), 130.1 (C_{19}), 133.48 (C_{11}), 133.52 (C_{10}), 133.8 (C_{20}), 135.8 (C_{15}), 137.4 (C_{21}), 149.7 (C_{14}), 166.2 (C_{17}). HRMS-ESI: *m/z* calcd for $C_{21}H_{20}N_3O_3$ [M+H^{+}] 362.1499; observed 362.1501. FTIR: neat (cm^{-1}) 3400, 1650, 1595, 1592, 1518, 1498, 1436, 1362, 1352, 1318, 1229, 1188, 1151, 1004.

(*E*)-**29**. Red oil. ^{1}H NMR* ($CDCl_3$, 500 MHz): δ 1.92 (s, 3H, H_1), 2.13 (s, 3H, H_2), 5.70 (s, 1H, H_3), 6.47 (br s, 1H, H_9), 7.04 (t, 1H, J = 7.0 Hz, H_6), 7.14 (br s, 1H, H_4), 7.24 (t, 2H, J = 7.5 Hz, H_7), 7.43 (d, 2H, J = 8.0 Hz, H_8), 7.57 (d, 1H, J = 7.5 Hz, H_{10}), 7.68 (s, 1H, H_5), 7.75 (t, 1H, J = 7.5 Hz, H_{11}), 7.66 (m, 1H, H_{12}), 8.13 (d, 1H, J = 8.0 Hz, H_{13}). ^{13}C NMR ($CDCl_3$, 126 MHz): δ 11.2 (C_1), 13.1 (C_2), 110.6 (C_3), 118.9 (C_{16}), 120.4 (C_8), 123.3 (C_{19}), 124.1 (C_6), 125.1 (C_5), 125.4 (C_{13}), 128.7 (C_7), 129.6 (C_{20}), 130.3 (C_{12}), 131.5 (C_{15}), 133.5 (C_{21}), 133.8 (C_{10}), 134.3 (C_{11}), 138.0 (C_{18}), 149.4 (C_{14}), 165.0 (C_{17}). HRMS-ESI: *m/z* calcd for $C_{21}H_{20}N_3O_3$ [M+H$^+$] 362.1499; observed 362.1503. *Peaks obtained from impure sample.

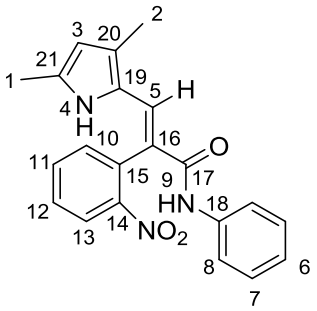

(*E*)-**29**

33. Yellow oil. ^{1}H NMR ($CDCl_3$, 500 MHz): δ 2.33 (s, 3H, H_2), 2.36 (s, 3H, H_1), 5.98 (s, 1H, H_3), 6.83 (m, 1H , H_{12}), 7.11 (m, 2H, H_{10}/H_{11}), 7.43 (t, 1H, J = 7.5 Hz, H_6), 7.45 (d, 2H, J = 7.0 Hz, H_8), 7.50 (s, 1H, H_5), 7.57 (m, 3H, H_7/H_9), 13.06 (br s, 1H, H_4). ^{13}C NMR ($CDCl_3$, 126 MHz): δ 11.7 (C_1), 13.9 (C_2), 109.0 (C_{12}), 111.2 (C_{15}), 112.8 (C_3), 117.1 (C_9), 122.0 (C_{10}), 123.7 (C_5), 125.4 (C_{11}), 125.6 (C_{14}), 127.1 (C_8), 127.1 (C_{18}), 127.9 (C_6), 129.6 (C_7), 132.8 (C_{19}), 135.1 (C_{17}), 137.2 (C_{20}), 139.7 (C_{13}), 168.0 (C_{16}). HRMS-ESI: *m/z* calcd for $C_{21}H_{19}N_2O$ [M+H$^+$] 315.1492; observed 315.1497.

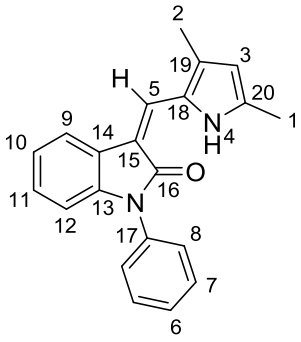

33

*(Z)- and (E)-N-benzyl-3-(3,5-dimethyl-1H-pyrrol-2-yl)-2-(2-nitrophenyl)acrylamide (Z)-**30** and (E)-**30**.*

Protocol as per **29**, using 2-(2-nitrophenyl)-*N*-benzylacetamide **24** in place of **23**.

(*Z*)-**30**. 16% yield, red crystalline solid. M.P. 140-142 ^{o}C. ^{1}H NMR ($CDCl_3$, 500 MHz): δ 2.09 (s, 3H, H_1), 2.31 (s, 3H, H_2), 4.50 (d, 2H, *J* = 6.0 Hz, H_9), 5.50 (br s, 1H, H_{10}), 5.83 (s, 1H, H_3), 6.48 (s, 1H, H_5), 7.20 (d, 2H, *J* = 8.0 Hz, H_8), 7.22 (m, 1H, *J* = 7.0 Hz, H_6), 7.28 (t, 2H, *J* = 7.5 Hz, H_7), 7.47 (m, 1H, *J* = 8.0 Hz. H_{13}), 7.49 (m, 1H, *J* = 6.5 Hz, H_{11}), 7.61 (t, 1H, *J* = 7.5 Hz, H_{12}), 7.94 (d, 1H, *J* = 8.5 Hz, H_{14}), 12.21 (br s, 1H, H_4). ^{13}C NMR ($CDCl_3$, 126 MHz): δ 11.3 (C_1), 13.6 (C_2), 43.9 (C_9), 110.7 (C_3), 115.8 (C_{17}), 124.0 (C_{20}), 124.7 (C_{14}), 127.33 (C_8), 127.34 (C_6), 128.3 (C_5), 128.6 (C_7), 128.9 (C_{13}), 129.2 (C_{21}), 133.1 (C_{22}), 133.3 (C_{12}), 133.4 (C_{11}), 136.0 (C_{16}), 138.0 (C_{19}), 149.5 (C_{15}), 167.6 (C_{18}). HRMS-ESI: *m/z* calcd for $C_{22}H_{22}N_3O_3$ [M+H$^+$] 376.1656; observed 376.1667. FTIR: neat (cm^{-1}) 3435, 1643, 1570, 1543, 1507, 1453, 1362, 1341, 1316, 1237, 1217, 1150.

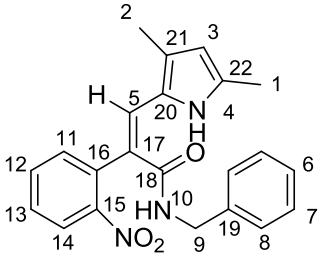

(*Z*)-**30**

(*E*)-**30**. < 5%, red amorphous solid (impure). ^{1}H NMR ($CDCl_3$, 500 MHz): δ 1.92 (s, 3H, H_1), 2.15 (s, 3H, H_2), 4.46 (d, 2H, *J* = 6.0 Hz, H_9), 5.50 (br s, 1H, H_{10}), 5.69 (s, 1H, H_3), 6.36 (br s, 1H, H_4), 7.20-7.33 (m, 5H, $H_{8\text{-}10}$), 7.54 (d, 1H, *J* = 7.0 Hz, H_{11}), 7.67 (m, 2H, $H_{5,13}$), 7.74 (t, 1H, *J* = 7.5 Hz, H_{12}), 8.14 (d, 1H, *J* = 8.5 Hz, H_{14}). Note: owing to impurities, the chemical shift of the pyrrolic N-H signal could not be assigned unambiguously. ^{13}C NMR ($CDCl_3$, 126 MHz): δ 11.3 (C_2), 13.1 (C_1), 43.9 (C_9), 110.4 (C_3), 118.6 (C_{17}), 123.3 (C_{20}), 124.9 (C_5), 125.4 (C_{14}), 127-129 ($C_{6\text{-}8}$), 129.2 (C_{21}), 130.1 (C_{13}), 132.0

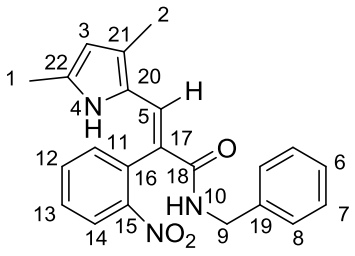

(*E*)-**30**

(C_{16}), 132.9 (C_{22}), 133.4 (C_{12}), 133.8 (C_{11}), 138.0 (C_{19}), 149.7 (C_{15}), 166.7 (C_{18}). Melting point and coherent FTIR not obtained due to impurity. HRMS-ESI: *m/z* calcd for $C_{22}H_{22}N_3O_3$ [$M+H^+$] 376.1656; observed 376.1677.

N,N-bis(2-hydroxyethyl)-4-nitroaniline **37**

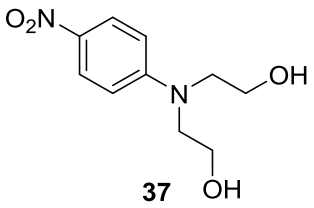

37

p-Fluoronitrobenzene (1.250 g, 8.86 mmol) and freshly distilled diethanolamine (0.767 g, 7.30 mmol) were added to a roundbottom flask under N_2. The reaction was stirred at 100 ^oC for 12 h, until consumption of starting material was observed by TLC analysis (EtOAc). The crude reaction mixture was diluted in EtOAc (50 mL) and washed with saturated $NaHCO_3$ (3 x 50 mL) and brine (3 x 50 mL). The organic layer was concentrated *in vacuo* and then recrystallised from MeOH/water to give **37** (1.27 g, 77% yield) as a yellow crystalline solid. Spectroscopic data for **37** were in accordance with the literature.[220]

N,N-bis(2-((tert-butyldimethylsilyl)oxy)ethyl)-4-nitroaniline **38**

TBDMSCl (80.0 mg, 0.53 mmol) and imidazole (78.4 mg, 1.15 mmol) were added to a roundbottom flask and stirred for 5 min in CH_2Cl_2 (5 mL). To the stirring solution was then added a solution containing *N,N*-bis(2-hydroxyethyl)-4-nitroaniline **37** (50.0 mg, 0.22 mmol) CH_2Cl_2 (5 mL) over 5 minutes. The reaction was stirred for 20 h, monitored by TLC analysis (EtOAc). The reaction was diluted with CH_2Cl_2 (20 mL) and cooled to -18 ^oC for 1 h. The precipitate was filtered off and the filtrated collected and added to a separating funnel. The organic phase was washed with saturated $NaHCO_3$ (5 x 25 mL) and brine (3 x 25 mL). The organic phase was then concentrated

and the residue purified by silica gel column chromatography (1:1 EtOAc:pet. spirit) to give **38** (72.8 mg, 72% yield) as a dark yellow crystalline product. Spectroscopic data were in accordance with the literature.[197]

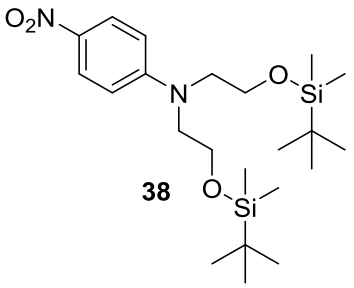

38

N-(4-aminophenyl)-2-(2-nitrophenyl)acetamide **36**

2-nitrophenylacetic acid (5.065 g, 28.0 mmol), *p*-phenylenediamine (3.333 g, 30.8 mmol) and HBTU (11.694 g, 30.8 mmol) were stirred in a roundbottom flask with CH_2Cl_2 (50 mL) under N_2 at 0^o C. DIPEA (10.7 mL, 61.4 mmol) was then added dropwise over 5 minutes to the stirring solution and the reaction allowed to warm to rt and stirred for 4 h with monitoring by TLC (EtOAc). The reaction was diluted with CH_2Cl_2 (100 mL), added to a separating funnel and extracted with 1 M hydrochloric acid (3 x 50 mL). The combined aqueous acidic phase was washed with CH_2Cl_2 (3 x 50 mL), removing a white precipitate. The combined acidic aqueous phase was neutralised using 1 M sodium hydroxide resulting in an off-white precipitate. The solid was filtered, washed with cold water and dried *in vacuo* afford **36** (5.70 g, 75% yield) as an off-white solid. Product purity could be increased by recrystallisation from hot EtOH. While compound **36** is commercially available (e.g. Aurora Building Blocks), no characterisation data have been reported in the literature.

M.P. 174-176 ^{o}C. ^{1}H NMR (d_6-DMSO, 500 MHz): δ 4.03 (s, 2H, H_5), 4.82 (s, 2H, H_1), 6.48 (d, 2H, J = 9.0 Hz, H_2), 7.16 (d, 2H, J = 9.0 Hz, H_3), 7.53 (m, 2H, $H_{6,8}$), 7.68 (t, 1H, J = 7.5 Hz, H_7), 8.01 (d, 1H, J = 8.0 Hz, H_9), 8.75 (s,

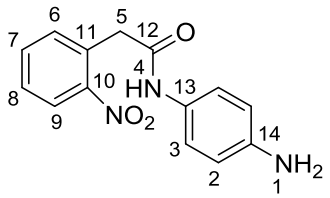

36

1H, H_4). ^{13}C NMR (d_6-DMSO, 126 MHz): δ 40.7 (C_5), 113.8 (C_2), 120.9 (C_3), 124.5 (C_9), 128.2 ($C_{8,13}$), 130.9 (C_{11}), 133.4 (C_6), 133.5 (C_7), 144.8 (C_{14}), 149.2 (C_{10}), 166.4 (C_{12}). HRMS-ESI: *m/z* calcd for $C_{14}H_{14}N_3O_3$ $[M+H^+]$ 272.1031; observed 272.1035. FTIR: neat (cm^{-1}) 3344, 1684, 1517, 1424, 1410, 1357, 1307, 1275, 1237, 1175.

N-(4-(bis(2-hydroxyethyl)amino)phenyl)-2-(2-nitrophenyl)acetamide **34**

N-(4-aminophenyl)-2-(2-nitrophenyl)acetamide **36** (1.902 g, 7.01 mmol) was added to a roundbottom flask along with anhydrous K_2CO_3 (1.750 g, 12.7 mmol) under N_2. 2-bromoethanol (15 mL) was added and the reaction mixture stirred at 50 ^oC for 5 days, or until complete consumption of starting material was observed by TLC analysis (EtOAc). The reaction mixture was concentrated and the residue taken up in EtOAc (50 mL). The organic phase was washed with brine (3 x 50 mL), dried over anhydrous $MgSO_4$ and evaporated to dryness. The crude residue was recrystallised from hot EtOH to afford **34** (1.69 g, 67% yield) as a pale yellow solid.

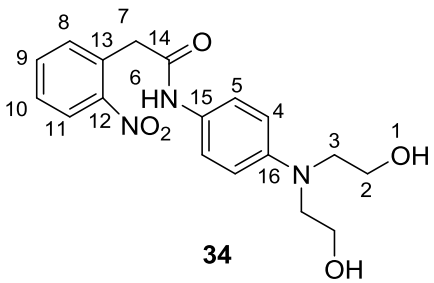

34

M.P. 134-136 ^oC. ^1H NMR (d_6-DMSO, 500 MHz): δ 3.35 (t, 4H, J = 6.5 Hz, H_3), 3.50 (q, 4H, J = 6.5 Hz, H_2), 4.04 (s, 2H, H_7), 4.69 (t, 2H, J = 5.5 Hz, H_1), 6.60 (d, 2H, J = 9.0 Hz, H_4), 7.29 (d, 2H, J = 9.0 Hz, H_5), 7.53 (m, 2H, $H_{8,9}$), 7.68 (t, 1H, J = 7.5 Hz, H_{10}), 8.02 (d, 1H, J = 8.0 Hz, H_{11}), 9.82 (s, 1H, H_6). ^{13}C NMR (d_6-DMSO, 126 MHz): δ 40.0 (C_7), 53.7 (C_3), 58.5 (C_2), 111.6 (C_4), 121.2 (C_5), 124.8 (C_{11}), 128.1 (C_{15}), 128.5 (C_{10}), 131.2 (C_{13}), 133.7 (C_8), 133.8 (C_9), 144.7 (C_{16}), 149.5 (C_{12}), 166.8 (C_{14}). HRMS-ESI: *m/z* calcd for $C_{18}H_{22}N_3O_5$ $[M+H^+]$ 360.1554; observed 360.1559. FTIR: neat (cm^{-1}) 3276, 1653, 1559, 1539, 1517, 1507, 1340, 1261, 1180, 1074, 1049.

N-(4-(bis(2-((tert-butyldimethylsilyl)oxy)ethyl)amino)phenyl)-2-(2-nitrophenyl)acetamide **8**

To to a roundbottom flask was added *N*-(4-(bis(2-hydroxyethyl)amino)phenyl)-2-(2-nitrophenyl)acetamide **34** (1.400 g, 3.90 mmol), TBDMSCl (2.046 g, 13.6 mmol) and imidazole (2.3369 g, 34.3 mmol), along with CH_2Cl_2 (30 mL). The reaction was stirred at rt for 2 h or until complete consumption of starting material was observed by TLC analysis (7:3 pet. spirit:EtOAc). The reaction was diluted with CH_2Cl_2 (50 mL) and cooled to -18 ^oC for 2 h. The precipitated solids were removed by gravity filtration and the filtrate added to a separating funnel. The organic phase was washed with saturated $NaHCO_3$ (5 x 50 mL) and brine (2 x 50 mL), dried over anhydrous $MgSO_4$ and concentrated. The crude residue was recrystallised from pet. spirit (-18 ^oC, overnight) to afford **8** (1.96 g, 86% yield) as orange crystals.

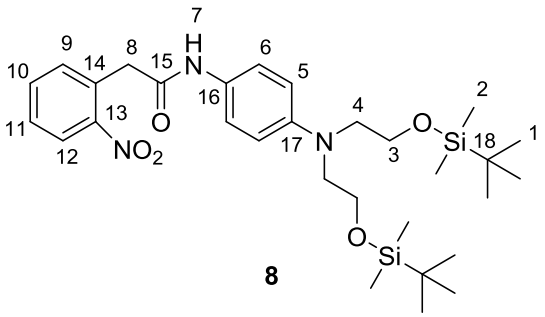

8

M.P. 118-119 ^oC. ^1H NMR ($CDCl_3$ 500 MHz): δ 0.02 (s, 12H, H_2), 0.88 (s, 18H, H_1), 3.46 (t, 4H, J = 6.5 Hz, H_4), 3.71 (t, 4H, J = 6.5 Hz, H_3), 3.96 (s, 2H, H_8), 6.60 (d, 2H, J = 9.0 Hz, H_5), 7.27 (d, 2H, J = 9.0 Hz, H_6), 7.45 (t, 1H, J = 7.5 Hz, H_{11}), 7.56 (br s, 1H, H_7), 7.57 (d, 1H, J = 7.5 Hz, H_9), 7.61 (t, 1H, J = 7.5 Hz, H_{10}), 8.04 (d, 1H, J = 8.0 Hz, H_{12}). ^{13}C NMR ($CDCl_3$, 126 MHz): -5.4 (C_2), 18.2 (C_{18}), 25.9 (C_1), 41.6 (C_8), 53.7 (C_4), 60.3 (C_3), 111.6 (C_5), 122.1 (C_6), 125.1 (C_{12}), 126.5 (C_{16}), 128.4 (C_{11}), 130.4 (C_{14}), 133.4 (C_9), 133.6 (C_{10}), 145.3 (C_{17}), 148.9 (C_{13}), 166.7 (C_{15}). HRMS-ESI: *m/z* calcd for $C_{30}H_{50}N_3O_5Si_2$ [$M+H^+$] 588.3284; observed 588.3289. FTIR: neat (cm^{-1}) 2950, 1682, 1653, 1528, 1517, 1343, 1254, 1238, 1194, 1131, 1100, 1071, 929, 899, 836, 812.

(Z)- and (E)-N-(4-(bis(2-((tert-butyldimethylsilyl)oxy)ethyl)amino)phenyl)-3-(3,5-dimethyl-1H-pyrrol-2-yl)-2-(2-nitrophenyl)acrylamide (*Z*)-**7** *and* (*E*)-**7**

N-(4-(bis(2-((tert-butyldimethylsilyl)oxy)ethyl)amino)phenyl)-2-(2-nitrophenyl)acetamide **8** (1.150 g, 1.96 mmol), oven-dried anhydrous K_2CO_3 (0.366 g, 2.65 mmol) and 18-crown-6 (0.6657 g, 2.52 mmol) were added to a three-necked roundbottom flask and dissolved in 15 mL of THF under N_2. The reaction was stirred at 65 ^oC for 1 h giving a brown to light blue coloured solution. 1-methoxycarbonyl-5-dimethyl-1*H*-pyrrole-2-carboxaldehyde **9** (0.4650 g, 2.57 mmol) in dry THF (10 mL) was then added dropwise over 15 minutes to the stirring solution. The reaction was heated at 65 ^oC for a further 12 h. After quenching with water, the reaction was extracted with EtOAc (2 x 50 mL) and the combined organic phase washed with saturated $NaHCO_3$ (2 x 50 mL) and brine (2 x 50 mL), dried over anhydrous $MgSO_4$ and concentrated. The crude residue was purified by silica gel column chromatography (100% pet. spirit to 8:2 pet. spirit:EtOAc) affording (*Z*)-**7** (0.56 g, 41% yield) as a red amorphous solid and (*E*)-**7** (0.30 g, 22% yield) as a red oil, along with trace amounts of the *N*-arylindolin-2-one **41**.

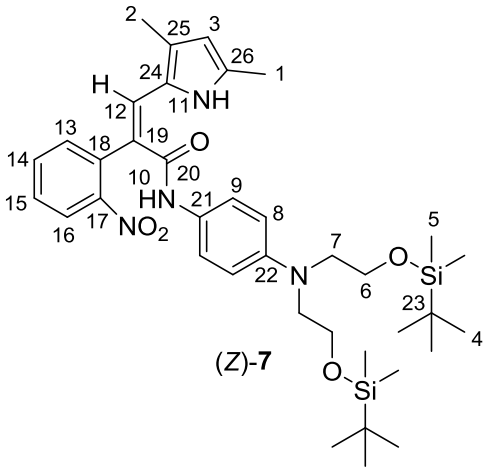

(*Z*)-**7**

(*Z*)-**7**. M.P. 174-176 ^oC. ^1H NMR ($CDCl_3$, 500 MHz): δ 0.03 (s, 12H, H_5), 0.88 (s, 18H, H_4), 2.10 (s, 3H, H_2), 2.28 (s, 3H, H_1), 3.46 (t, 4H, *J* = 6.5 Hz, H_7), 3.71 (t, 4H, *J* = 6.5 Hz, H_6), 5.82 (s, 1H, H_3), 6.51 (s, 1H, H_{12}), 6.61 (d, 2H, *J* = 9.0 Hz, H_8), 6.66 (s, 1H, H_{10}), 7.13 (d, 2H, *J* = 9.0 Hz, H_9), 7.55 (t, 1H, *J* = 8.0 Hz, H_{15}), 7.59 (d, 1H, *J* = 7.5 Hz, H_{13}), 7.68 (t, 1H, *J* = 8.0 Hz, H_{14}), 8.01 (d, 1H, *J* = 8.0 Hz, H_{16}),

12.08 (br s, 1H, H_{11}). ^{13}C NMR ($CDCl_3$, 126 MHz): δ -5.4 (C_5), 11.4 (C_2), 13.6 (C_1), 18.3 (C_{23}), 25.9 (C_4), 53.7 (C_7), 60.2 (C_6), 110.8 (C_3), 111.6 (C_8), 116.2 (C_{19}), 124.2 ($C_{24,}$ C_9), 124.8 (C_{16}), 125.7 (C_{21}), 128.6 (C_{12}), 128.9 (C_{15}), 129.4 (C_{25}), 133.4 (C_{26}), 133.4 (C_{14}), 133.5 (C_{13}), 136.2 (C_{18}), 145.9 (C_{22}), 149.6 (C_{17}), 166.3 (C_{20}). HRMS-ESI: *m/z* calcd for $C_{37}H_{57}N_4O_5Si_2$ [M+H^+] 693.3862; observed 693.3861. FTIR: neat (cm^{-1}) 3313, 2928, 1654, 1612, 1595, 1514, 1379, 1360, 1322, 1289, 1250, 1095, 1054, 833, 810.

(*E*)-**7**. Red oil. ^1H NMR ($CDCl_3$, 500 MHz): δ -0.02 (s, 12H, H_5), 0.85 (s, 18H, H_4), 2.22 (s, 3H, H_2), 2.26 (s, 3H, H_1), 3.41 (t, 4H, *J* = 6.4 Hz, H_7), 3.67 (t, 4H, *J* = 6.4 Hz, H_6), 3.90 (br s, 1H, H_{10}), 5.79 (s, 1H, H_3), 6.53 (d, 2H, *J* = 9.0 Hz, H_8), 7.23 (d, 2H, *J* = 9.0 Hz, H_9), 7.34 (t, 1H, *J* = 8.0 Hz, H_{15}), 7.43 (d, 1H, *J* = 7.0 Hz, H_{13}), 7.49 (t, 1H, *J* = 7.0 Hz, H_{14}), 7.95 (d, 1H, *J* = 8.0 Hz, H_{16}), 8.03 (br s, 1H, H_{11}). ^{13}C NMR ($CDCl_3$, 126 MHz): δ -5.5 (C_5), 12.9 ($C_{1,2}$), 18.1 (C_{23}), 25.8 (C_4), 53.6 (C_7), 60.2 (C_6), 111.5 (C_8), 111.9 (C_3), 122.0 ($C_{9,12}$), 124.8 (C_{16}), 126.7 (C_{19}), 126.8 (C_{21}), 128.1 (C_{15}), 128.6 (C_{25}), 130.5 (C_{26}), 131.3 (C_{24}), 133.3 ($C_{13,14}$), 138.8 (C_{18}), 145.0 (C_{22}), 148.8 (C_{17}), 167.0 (C_{20}). HRMS-ESI: *m/z* calcd for $C_{37}H_{57}N_4O_5Si_2$ [M+H^+] 693.3862; observed 693.3860.

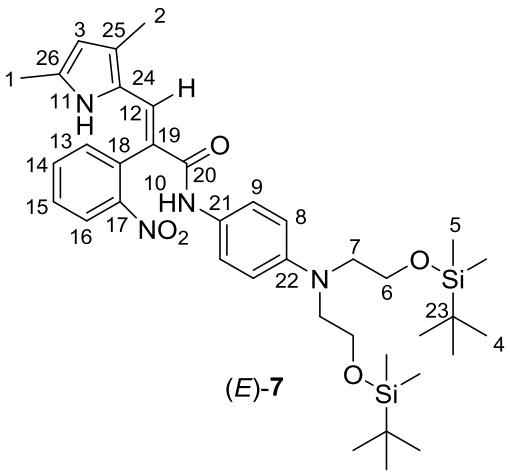

(*E*)-**7**

(Z)-1-(4-(bis(2-((tert-butyldimethylsilyl)oxy)ethyl)amino)phenyl)-3-((3,5-dimethyl-1H-pyrrol-2-yl)methylene)indolin-2-one **41**.

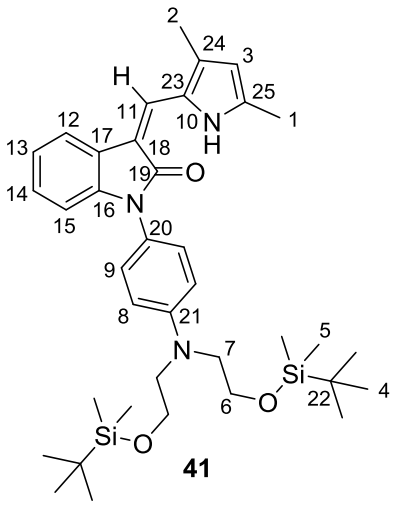

41

^{1}H NMR ($CDCl_3$, 500 MHz): δ 0.07 (s, 12H, H_5), 0.91 (s, 18H, H_4), 2.31 (s, 3H, H_1), 2.34 (s, 12H, H_2), 3.56 (t, 4H, *J* = 6.5 Hz, H_7), 3.80 (t, 4H, *J* = 6.5 Hz, H_6), 5.96 (s, 1H, H_3), 6.77 (d, 1H, *J* = 7.0 Hz, H_{15}), 6.81 (d, 2H, *J* = 9.0 Hz, H_8), 7.08 (m, 2H, H_{13},H_{14}), 7.24 (d, 2H, *J* = 9.0 Hz, H_9), 7.45 (s, 1H, H_{11}), 7.54 (d, 1H, *J* = 7.0 Hz, H_{12}), 13.21 (br s, 1H, H_{10}). ^{13}C NMR ($CDCl_3$, 126 MHz): δ -5.3 (C_5), 11.6 (C_2), 13.9 (C_1), 18.3 (C_{22}), 25.9 (C_4), 53.6 (C_7), 60.3 (C_6), 109.1 (C_{15}), 111.7 (C_{18}), 112.0 (C_8), 112.5 (C_3), 117.0 (C_{12}), 121.7 (C_{13}), 122.8 (C_{20}), 123.3 (C_{11}), 125.4 (C_{14}), 125.5 (C_{17}), 127.1 (C_{24}), 128.0 (C_9), 132.2 (C_{23}), 136.7 (C_{25}), 140.7 (C_{16}), 147.7 (C_{21}), 168.5 (C_{19}). HRMS-ESI: *m/z* calcd for $C_{37}H_{56}N_3O_3Si_2$ [M+H$^+$] 646.3855; observed 646.3860. FTIR: neat (cm^{-1}) 2928, 1666, 1610, 1596, 1564, 1518, 1462, 1371, 1360, 1316, 1278, 1239, 1180, 1150, 1095, 995, 967, 911, 833, 810.

(Z)-N-(4-(bis(2-hydroxyethyl)amino)phenyl)-3-(3,5-dimethyl-1H-pyrrol-2-yl)-2-(2-nitrophenyl)acrylamide (*Z*)-**42**

To a solution of (*Z*)-**7** (0.500 g, 0.721 mmol) in THF (5 mL) at 0 ^{o}C was added 5:1 1 M TBAF (in THF):glacial acetic acid (3 mL) dropwise over 1 minute. The reaction was stirred at 0 ^{o}C for 4 h or until complete consumption of starting material was observed by TLC analysis (1:1 pet. spirit:EtOAc). The reaction was quenched with saturated $NaHCO_3$ (10 mL) and extracted with EtOAc (2 x 40 mL) and the combined organic phase washed with saturated $NaHCO_3$ (2 x 50 mL) and brine (2 x 50 mL), dried over anhydrous $MgSO_4$ and concentrated. The crude residue was purified by silica gel

column chromatography (EtOAc) to afford (*Z*)-**42** (0.28 g, 85%) as a red crystalline solid.

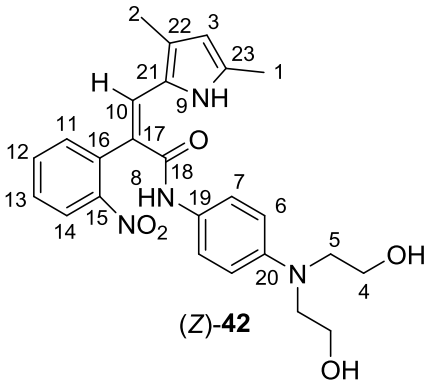

(*Z*)-**42**

M.P. 102-104 ^{o}C. ^{1}H NMR ($CDCl_3$, 500 MHz): δ 2.10 (s, 3H, H_2), 2.26 (s, 3H, H_1), 3.50 (t, 4H, *J* = 6.0 Hz, H_5), 3.78 (t, 4H, *J* = 6.0 Hz, H_4), 5.82 (s, 1H, H_3), 6.54 (s, 1H, H_{10}), 6.61 (d, 2H, *J* = 8.5 Hz, H_6), 6.74 (s, 1H, H_8), 7.12 (d, 2H, *J* = 8.5 Hz, H_7), 7.53 (t, 1H, *J* = 8.0 Hz, H_{13}), 7.58 (d, 1H, *J* = 7.5 Hz, H_{11}), 7.68 (t, 1H, *J* = 7.5 Hz, H_{12}), 8.00 (d, 1H, *J* = 8.5, H_{14}). ^{13}C NMR ($CDCl_3$, 126 MHz): δ 11.4 (C_2), 13.6 (C_1), 55.2 (C_5), 60.5 (C_4), 110.9 (C_3), 112.8 (C_6), 116.0 (C_{17}), 124.1 (C_{21}), 124.2 (C_7), 124.9 (C_{14}), 126.6 (C_{19}), 128.8 (C_{10}), 129.0 (C_{13}), 129.6 (C_{22}), 133.4 (C_{23}), 133.5 ($C_{11/12}$), 136.1 (C_{16}), 145.8 (C_{20}), 149.4 (C_{15}), 166.5 (C_{18}). HRMS-ESI: *m/z* calcd for $C_{25}H_{29}N_4O_5$ [M+H$^+$] 465.2132; observed 465.2138. FTIR: neat (cm^{-1}) 3274, 2868, 1641, 1513, 1341, 1321, 1262, 1235, 1202, 1179, 1151, 1041, 1001.

(Z)-((4-(3-(3,5-dimethyl-1H-pyrrol-2-yl)-2-(2-nitrophenyl)acrylamido)phenyl)azanediyl) bis(ethane-2,1-diyl) dimethanesulfonate (*Z*)-**43** *and (Z)- and (E)-N-(4-(bis(2-chloroethyl)amino)phenyl)-3-(3,5-dimethyl-1H-pyrrol-2-yl)-2-(2-nitrophenyl)acrylamide (Z)*-**1** and (*E*)-**1**

Diol (*Z*)-**42** (0.350 g, 0.75 mmol) was stirred in CH_2Cl_2 (10 mL) at 0 ^{o}C under N_2 and triethylamine (0.30 mL, 2.15 mmol) was added, followed by mesyl chloride (0.15 mL, 1.94 mmol). The reaction was stirred at 0 ^{o}C for 1 h or until complete consumption of starting material by TLC analysis (EtOAc). The reaction was diluted with CH_2Cl_2 (40 mL) and the combined mixture was added to a separating funnel. The organic phase was

washed with saturated $NaHCO_3$ (2 x 50 mL) and brine (2 x 50 mL), dried over anhydrous $MgSO_4$ and concentrated. The crude residue was purified by column chromatography (EtOAc) to afford (*Z*)-**43** (0.40 g, 86% yield) as an unstable red oil.

(*Z*)-**43**. ^{1}H NMR ($CDCl_3$, 500 MHz): δ 2.10 (s, 3H, H_2), 2.22 (s, 3H, H_1), 2.94 (s, 6H, H_4), 3.70 (br s, 4H, H_6), 4.30 (br s, 4H, H_5), 5.83 (s, 1H, H_3), 6.56 (s, 1H, H_{11}), 6.68 (d, 2H, *J* = 8.5 Hz, H_7), 6.67 (br s, 1H, *J* = 4.0 Hz, H_9), 7.21 (d, 2H, *J* = 8.0 Hz, H_8), 7.55 (t, 1H, *J* = 7.0 Hz, H_{14}), 7.59 (d, 1H, *J* = 7.0 Hz, H_{12}), 7.70 (t, 1H, *J* = 7.0 Hz, H_{13}), 8.01 (d, 1H, *J* = 7.0 Hz, H_{15}), 12.01 (br s, 1H, H_{10}). ^{13}C NMR ($CDCl_3$, 126 MHz): δ 11.2 (C_2), 13.4 (C_1), 37.1 (C_4), 50.8 (C_6), 66.6 (C_5), 110.8 (C_3), 112.9 (C_7), 116.1 (C_{18}), 123.9 (C_{22}), 124.0 (C_8), 124.8 (C_{15}), 128.0 (C_{20}), 128.7 (C_{11}), 129.0 (C_{14}), 129.5 (C_{23}), 133.2 (C_{24}), 133.4 (C_{12}), 133.6 (C_{13}), 135.7 (C_{17}), 143.7 (C_{21}), 149.1 (C_{16}), 166.2 (C_{19}). HRMS-ESI: *m/z* calcd for $C_{27}H_{33}N_4O_9S_2$ [$M+H^+$] 621.1683; observed 621.1689.

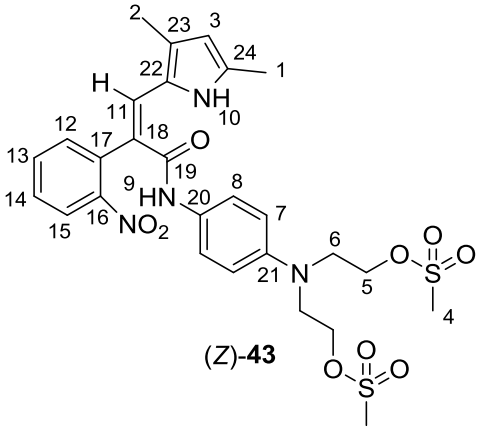

(*Z*)-**43**

Dimesylate (*Z*)-**43** was immediately taken into DMF (8 mL) and excess lithium chloride (~0.2 g) added. The solution was stirred at 75 ^{o}C for 45 minutes until complete consumption of starting material by TLC analysis (1:1 pet. spirit:EtOAc). The reaction was concentrated and taken up in EtOAc (50 mL), washed with water (3 x 50 mL), dried over anhydrous $MgSO_4$ and concentrated. The crude residue was purified by silica gel column chromatography (100% pet. spirit to 8:2 pet. spirit:EtOAc) to afford (*Z*)-**1** (0.30 g, 92% yield) as an orange crystalline product. Trace amounts of (*E*)-**1** (0.01 g, 3% yield) was also obtained from the reaction.

(*Z*)-**1**. M.P. 180 ^{o}C (dec.). ^{1}H NMR ($CDCl_3$, 500 MHz): δ 2.11 (s, 3H, H_2), 2.28 (s, 3H, H_1), 3.60 (t, 4H, *J* = 7.0 Hz, H_5), 3.70 (t, 4H, *J* = 7.0 Hz, H_4), 5.83 (s, 1H, H_3), 6.55 (s, 1H, H_{10}), 6.64 (d, 2H, *J* = 9.0 Hz, H_6), 6.69 (br s, 1H, H_8), 7.21 (d, 2H, *J* = 8.5 Hz, H_7), 7.56 (t, 1H, *J* = 8.0 Hz, H_{13}), 7.60 (d, 1H, *J* = 7.5 Hz, H_{11}), 7.70 (t, 1H, *J* = 7.5 Hz, H_{12}), 8.02 (d, 1H, *J* = 8.0 Hz, H_{14}), 12.03 (br s, 1H, H_9). ^{13}C NMR ($CDCl_3$, 126 MHz): δ 11.4 (C_2), 13.6 (C_1), 40.4 (C_5), 53.6 (C_4), 110.9 (C_3), 112.4 (C_6), 115.8 (C_{17}), 124.1 (C_{21}), 124.5 (C_7), 124.9 (C_{14}), 127.6 (C_{19}), 129.0 ($C_{10,}$ C_{13}), 129.8 (C_{22}), 133.5 (C_{11}, C_{12}), 133.6 (C_{23}), 136.1 (C_{16}), 143.8 (C_{20}), 149.5 (C_{15}), 166.8 (C_{18}). HRMS-ESI: *m/z* calcd for $C_{25}H_{27}(^{35}Cl)_2N_4O_3$ [M+H^{+}] 501.1455; observed 501.1455. FTIR: neat (cm^{-1}) 3402, 2921, 2852, 1647, 1521, 1513, 1460, 1353, 1322, 1235, 1178, 1150, 747.

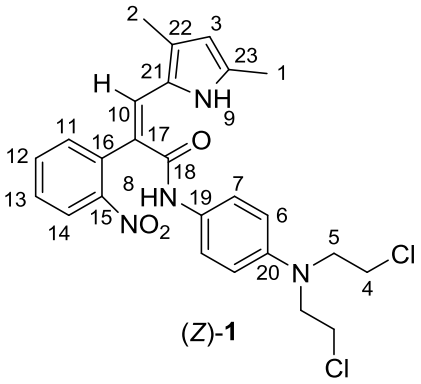

(*Z*)-**1**

(*E*)-**1**. M.P. 70-72 ^{o}C. ^{1}H NMR ($CDCl_3$, 500 MHz): δ 1.93 (s, 3H, H_1), 2.16 (s, 3H, H_2), 3.58 (t, 4H, *J* = 7.0 Hz, H_4), 3.67 (t, 4H, *J* = 7.0 Hz, H_5), 5.71 (s, 1H, H_3), 6.43 (br s, 1H H_9), 6.60 (d, 2H, *J* = 8.0 Hz, H_6), 6.91 (s, 1H, H_8), 7.30 (d, 2H, *J* = 8.0 Hz, H_7), 7.59 (d, 1H, *J* = 7.5 Hz, H_{11}), 7.67 (s, 1H, H_{10}), 7.70 (t, 1H, *J* = 7.5 Hz, H_{13}), 7.78 (t, 1H, *J* = 8.0 Hz, H_{12}), 8.16 (d, 1H, *J* = 8.0 Hz, H_{14}). ^{13}C NMR ($CDCl_3$, 126 MHz): δ 11.3 (C_2), 13.1 (C_1), 40.5 (C_4), 53.6 (C_5), 110.5 (C_3), 112.5 (C_6), 119.0 (C_{17}), 122.7 (C_7), 123.4 (C_{22}), 124.9 (C_{10}), 125.4 (C_{14}), 128.9 (C_{21}), 129.3 (C_{19}), 130.2 (C_{13}), 131.8 (C_{16}), 133.2 (C_{23}), 133.9 (C_{11}), 134.2 (C_{12}), 143.1 (C_{20}), 149.6 (C_{15}), 164.8 (C_{18}). HRMS-ESI: *m/z* calcd for $C_{25}H_{27}(^{35}Cl)_2N_4O_3$

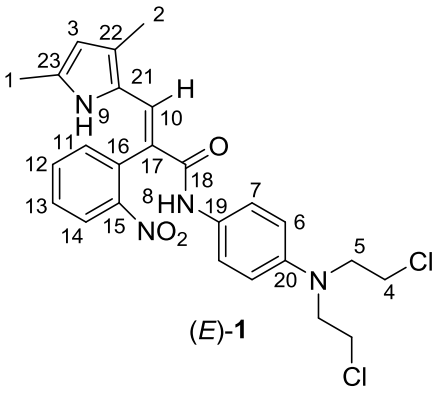

(*E*)-**1**

[$M+H^+$] 501.1455; observed 501.1453. FTIR: neat (cm^{-1}) 3309, 2912, 1653, 1525, 1517, 1346, 1249, 1216, 807, 636.

5.2.1 2-Aryl-3*H*-pyrrolizin-3-ones

5.2.1.1 General Procedure

An oven-dried 50 mL round-bottom flask containing a magnetic stirrer bar was sealed with a septum, charged with Ar and tared. KH (~0.5 g, 30% mineral oil dispersion) was then added to the flask and mineral oil was removed by washing with pet. spirit (2 x 30 mL) using a syringe under N_2 flow. The flask containing dry KH was charged with Ar and weighed to obtain an accurate mass of KH. Dry THF (10 mL) was added to the flask containing KH (0.15 g, 3.7 mmoles, under Ar) and the mixture cooled to 0 ^oC. 3,5-dimethyl-1H-pyrrole-2-carbaldehyde **4** (0.23 g, 1.9 mmoles) was dissolved in dry THF (5 mL) under Ar and slowly cannulated into the stirring KH solution (caution: flask requires outlet needle to release evolving H_2 gas). The mixture was left to stir for 5 minutes at 0 ^oC. Phenylacetic acid derivative (1.9 mmoles) was added to a separate 50 mL round-bottom flask under Ar along with HBTU (0.71 g, 1.9 mmoles) and dry CH_2Cl_2 (10 mL) under Ar. DIPEA (0.65 mL, 3.7 mmoles) was added dropwise to the solution and stirred for 5 minutes until the HBTU completely dissolved. The HBTU solution was cooled to 0 ^oC before addition in a single portion to the pyrrole carboxaldehyde solution at 0 ^oC. The reaction was allowed to warm slowly to room temperature. A dark red colour was observed in each reaction indicating formation of the desired product. The reaction was quenched with ice-cold water after 2 h and extracted with Et_2O (2 x 50 mL). The combined organic phase was washed with saturated $NaHCO_3$ solution (2 x 50 mL) and brine (2 x 50 mL), dried over anhydrous

$MgSO_4$ and concentrated. The crude residue was purified by silica gel column chromatography using a gradient from 100% pet. spirit to 1:9 acetone:pet. spirit) to afford the 2-aryl-3H-pyrrolizin-3-one product as a dark red solid.

5.2.1.2 Compound Chatacterisation

5,7-dimethyl-2-(2-nitrophenyl)-3H-pyrrolizin-3-one **14**

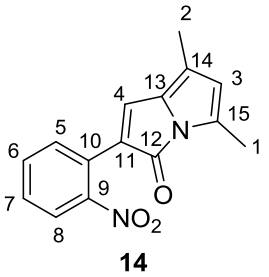

14

27% yield. M.P. 122-124 ^{o}C. ^{1}H NMR ($CDCl_3$, 500 MHz): δ 2.03 (s, 3H, H_2), 2.29 (s, 3H, H_1), 5.57 (s, 1H, H_3), 7.14 (s, 1H, H_4), 7.45 (t, 1H, J = 8.5 Hz, H_7), 7.47 (d, 1H, J = 8.5 Hz, H_5), 7.59 (t, 1H, J = 8.5 Hz, H_6), 7.95 (d, 1H, J = 8.5 Hz, H_8). ^{13}C NMR ($CDCl_3$, 126 MHz): δ 11.4 (C_2), 12.4 (C_1), 116.2 (C_3), 124.6 (C_8), 126.3 (C_{10}), 126.6 (C_{11}, C_{14}), 128.8 (C_6), 130.7 (C_4), 130.8 (C_5), 132.1 (C_{13}), 132.8 (C_7), 135.8 (C_{15}), 148.6 (C_9), 163.7 (C_{12}). ESI-HRMS: *m/z* calculated for $C_{17}H_{16}N_2O_4$ $[M + H]^+$ 269.0926; observed 269.0898. FTIR: neat (cm^{-1}) 2921, 2360, 1727, 1603, 1560, 1523, 1395, 1354, 1288, 1248, 1209, 1128.

5,7-dimethyl-2-phenyl-3H-pyrrolizin-3-one **51**

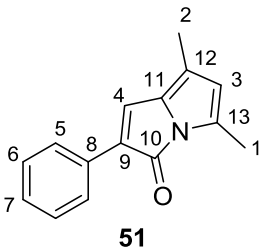

51

48% yield. M.P. 46-48 ^{o}C. ^{1}H NMR ($CDCl_3$, 500 MHz): δ 2.01 (s, 3H, H_2), 2.33 (s, 3H, H_1), 5.55 (s, 1H, H_3), 7.22 (s, 1H, H_4), 7.27 (t, 1H, J = 7.5 Hz, H_7), 7.36 (t, 2H, J = 8.0 Hz, H_6), 7.77 (d, 2H, J = 8.0 Hz, H_5). ^{13}C NMR ($CDCl_3$, 126 MHz): δ 11.4 (C_2), 12.4 (C_1), 115.9 (C_3), 124.6 (C_{11}), 126.0 (C_6), 127.6 (C_7), 128.2 (C_4), 128.5 (C_5), 130.0 (C_8), 130.0/132.1 (C_9, C_{12}), 134.7 (C_{13}), 165.6 (C_{10}). ESI-HRMS: *m/z* calculated

for $C_{15}H_{14}NO$ $[M + H]^+$ 224.1068; observed 224.1075. FTIR: neat (cm^{-1}) 2919, 1719, 1700, 1598, 1527, 1445, 1360, 1293, 1269, 1207, 1131.

2-(2-fluorophenyl)-5,7-dimethyl-3H-pyrrolizin-3-one **69**

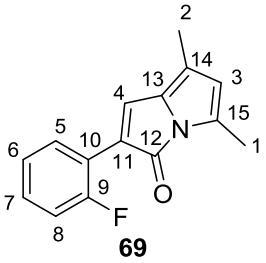

69

37% yield. M.P. 37-38 °C. ^{1}H NMR ($CDCl_3$, 500 MHz): δ 1.99 (s, 3H, H_2), 2.31 (s, 3H, H_1), 5.53 (s, 1H, H_3), 7.06 (dd, 1H, *J* = 12.0, 8.0 Hz, H_8), 7.14 (m, 1H, H_6), 7.19 (m, 1H, H_7), 7.43 (d, 1H, *J* = 2.5 Hz, H_4), 8.15 (m, 1H, H_5). ^{13}C NMR ($CDCl_3$, 126 MHz): δ 11.3 (C_2), 12.3 (C_1), 115.5 (C_8, $^2J_{C\text{-}F}$ = 22.6 Hz), 116.1 (C_3), 120.1 (C_{10}, $^2J_{C\text{-}F}$ = 11.6 Hz), 123.1 (C_{11}, $^3J_{C\text{-}F}$ = 2.5 Hz), 124.03 (C_6, $^4J_{C\text{-}F}$ = 3.4 Hz), 125.6 (C_{13}), 128.4 (C_7, $^3J_{C\text{-}F}$ = 8.7 Hz), 129.0 (C_5, $^3J_{C\text{-}F}$ = 2.9 Hz), 132.29 (C_{14}), 132.6 (C_4), 135.0 (C_{15}), 160.4 (C_9, $^1J_{C\text{-}F}$ = 249.9 Hz), 165.4 (C_{12}). ESI-HRMS: *m/z* calculated for $C_{15}H_{13}FNO$ $[M + H]^+$ 242.0981; observed 242.0981. FTIR: neat (cm^{-1}) 2922, 1734, 1716, 1530, 1486, 1397, 1368, 1302, 1260.54, 1211, 1136, 770.

2-(3-fluorophenyl)-5,7-dimethyl-3H-pyrrolizin-3-one **70**

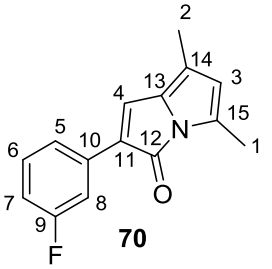

70

37% yield. M.P. 55-57 °C. ^{1}H NMR ($CDCl_3$, 500 MHz): δ 2.01 (s, 3H, H_2), 2.32 (s, 3H, H_1), 5.56 (s, 1H, H_3), 6.95 (m, 1H, H_7), 7.23 (s, 1H, H_4), 7.30 (dd, 1H, *J* = 14.0 Hz, 7.5 Hz, H_6), 7.53 (d, 1H, *J* = 11.0 Hz, H_8) , 7.54 (d, 1H, 6.5 Hz, H_5). ^{13}C NMR ($CDCl_3$, 126 MHz): δ11.4 (C_2), 12.4 (C_1), 112.8 (C_8, $^2J_{C\text{-}F}$ = 23.0 Hz), 114.3 (C_7, $^2J_{C\text{-}F}$ = 21.6 Hz), 116.1 (C_3), 121.49 (C_5, $^4J_{C\text{-}F}$ = 2,9 Hz), 125.7 (C_{14}), 128.5 (C_{11}, $^4J_{C\text{-}F}$ = 2.8 Hz), 129.0 (C_4), 129.9 (C_6, $^3J_{C\text{-}F}$ = 8.7 Hz), 131.7 (C_{14}), 134.1 (C_{10}, $^3J_{C\text{-}F}$ = 8.7 Hz), 135.2 (C_{15}), 161.9 (C_9, $^1J_{C\text{-}F}$ = 245 Hz), 165.2 (C_{12}). ESI-

HRMS: *m/z* calculated for $C_{15}H_{13}FNO$ $[M + H]^+$ 242.0981; observed 242.0979. FTIR: neat (cm^{-1}) 2916, 1707, 1601, 1582, 1530, 1437, 1397, 1366, 1298, 1265, 1215, 1138, 1134, 910, 874, 809, 782.

2-(4-fluorophenyl)-5,7-dimethyl-3H-pyrrolizin-3-one **71**

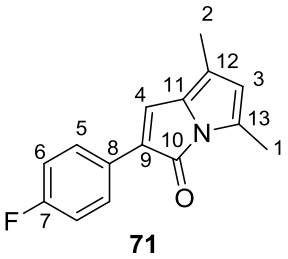

71

38% yield. M.P. 56-58 ^oC. ^1H NMR ($CDCl_3$, 500 MHz): δ 2.00 (s, 3H, H_2), 2.31 (s, 3H, H_1), 5.54 (s, 1H, H_3), 7.04 (t, 2H, J = 8.5 Hz, H_6), 7.15 (s, 1H, H_4), 7.75 (dd, 2H, J = 8.5, 5.5 Hz, H_5). ^{13}C NMR ($CDCl_3$, 126 MHz): δ11.4 (C_2), 12.4 (C_1), 115.5 (C_6, $^2J_{C\text{-}F}$ = 21.5 Hz), 115.9 (C_3), 124.8 (C_{11}), 127.7 (C_4), 127.8 (C_5), 128.2 (C_9), 129.0 (C_8), 131.9 (C_{12}), 134.7 (C_{13}), 161.3/163.2 (C_7, $^1J_{C\text{-}F}$ = 247.8 Hz), 165.5 (C_{10}). ESI-HRMS: *m/z* calculated for $C_{15}H_{13}NOF$ $[M + H]^+$ 242.0981; observed 242.0981. FTIR: neat (cm^{-1}) 2917, 1711, 1608, 1557, 1531, 1499, 1450, 1394, 1364, 1299, 1267, 1225, 1158, 1139, 1133, 1095, 828.

2-(2-chlorophenyl)-5,7-dimethyl-3H-pyrrolizin-3-one **72**

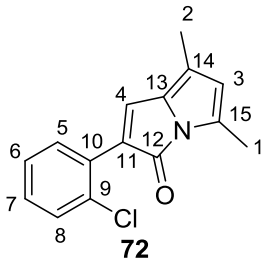

72

16% yield. M.P. 84-86 ^oC. ^1H NMR ($CDCl_3$, 500 MHz): δ 2.03 (s, 3H, H_2), 2.33 (s, 3H, H_1), 5.57 (s, 1H, H_3), 7.21 (m, 1H, H_6), 7.28 (m, 1H, H_7), 7.42 (dd, 1H, J = 7.5, 1.0 Hz, H_5), 7.43 (s, 1H, H_4), 7.62 (dd, 1H, J = 8.0, 1.5 Hz, H_8). ^{13}C NMR ($CDCl_3$, 126 MHz): δ 11.4 (C_2), 12.3 (C_1), 116.0 (C_3), 125.6 (C_{13}), 126.6 (C_7), 127.5 (C_{14}), 128.6 (C_6), 130.2 (C_5), 130.2 (C_9), 131.0 (C_8), 131.9 (C_{10}), 132.8 (C_{11}), 133.6 (C_4), 135.1 (C_{15}), 165.3 (C_{12}). ESI-HRMS: *m/z* calculated for $C_{15}H_{13}(^{35}Cl)NO$ $[M + H]^+$ 258.0686; observed 258.0681. FTIR: neat (cm^{-1}) 2924, 2357, 1719, 1612, 1533, 1295, 768, 734.

2-(3-chlorophenyl)-5,7-dimethyl-3H-pyrrolizin-3-one **73**

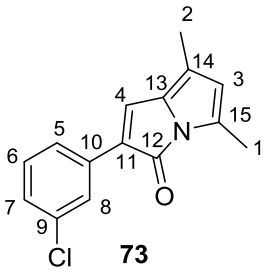

73

35% yield. M.P. 84-86 ^{o}C. ^{1}H NMR ($CDCl_3$, 500 MHz): δ 2.01 (s, 3H, H_2), 2.32 (s, 3H, H_1), 5.56 (s, 1H, H_3), 7.23 (t, 1H, *J* = 8.5 Hz, H_7), 7.23 (s, 1H, H_4), 7.27 (t, 1H, *J* = 8.0 Hz, H_6), 7.66 (d, 1H, *J* = 8.0 Hz, H_5), 7.78 (t, 1H, *J* = 1.5 Hz, H_8). ^{13}C NMR ($CDCl_3$, 126 MHz): δ 11.4 (C_2), 12.4 (C_1), 116.1 (C_3), 123.96 (C_5), 123.97 (C_{11}), 125.7 (C_{13}), 125.9 (C_8), 127.4 (C_7), 128.3 (C_{14}), 129.0 (C_4), 129.7 (C_6), 133.7 (C_{10}), 134.5 (C_9), 135.2 (C_{15}), 156.1 (C_{12}). ESI-HRMS: *m/z* calculated for $C_{15}H_{13}NO(^{35}Cl)$ $[M + H]^+$ 258.0680; observed 258.0695. FTIR: neat (cm^{-1}) 2913, 1716, 1589, 1530, 1477, 1379, 1364, 1137, 1093, 782, 722, 683.

2-(4-chlorophenyl)-5,7-dimethyl-3H-pyrrolizin-3-one **74**

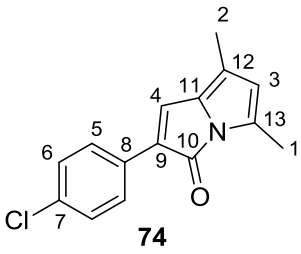

74

30% yield. M.P. 87-89 ^{o}C. ^{1}H NMR ($CDCl_3$, 500 MHz): δ 2.01 (s, 3H, H_2), 2.32 (s, 3H, H_1), 5.55 (s, 1H, H_3), 7.20 (s, 1H, H_4), 7.32 (d, 1H, *J* = 7.5 Hz, H_6), 7.72 (d, 1H, *J* = 7.5 Hz, H_5). ^{13}C NMR ($CDCl_3$, 126 MHz): δ11.4 (C_2), 12.4 (C_1), 116.1 (C_3), 125.3 (C_{11}), 127.2 (C_5), 128.3 (C_4), 128.7 (C_6), 128.7 (C_9), 130.5 (C_8), 131.9 (C_{12}), 133.3 (C_7), 135.0 (C_{13}), 165.4 (C_{10}). ESI-HRMS: *m/z* calculated for $C_{15}H_{13}(^{35}Cl)NO$ $[M + H]^+$ 258.0680; observed 258.0681. FTIR: neat (cm^{-1}) 2932, 1721, 1604, 1525, 1262, 875, 796.

2-(2-bromophenyl)-5,7-dimethyl-3H-pyrrolizin-3-one **75**

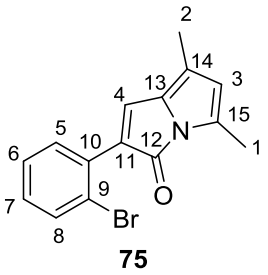

75

13% yield. M.P. 114-116 ^{o}C. ^{1}H NMR ($CDCl_3$, 500 MHz): δ 2.02 (s, 3H, H_2), 2.32 (s, 3H, H_1), 5.57 (s, 1H, H_3), 7.14 (m, 1H, H_7), 7.32 (m, 1H, H_6), 7.50 (dd, 1H, J = 8.0, 1.5 Hz, H_5), 7.62 (dd, 1H, J = 8.0, 1.0 Hz, H_8). ^{13}C NMR ($CDCl_3$, 126 MHz): δ 11.4 (C_2), 12.3 (C_1), 115.9 (C_3), 122.8 (C_9), 125.6 (C_{14}), 127.1 (C_6), 128.9 (C_7), 129.5 (C_{11}), 131.2 (C_5), 131.7 (C_{15}), 132.2 (C_{10}), 133.4 (C_8), 133.5 (C_4), 135.1 (C_{13}), 165.0 (C_{12}). ESI-HRMS: *m/z* calculated for $C_{15}H_{13}(^{79}Br)NO$ $[M + H]^+$ 302.0175; observed 302.0177. FTIR: neat (cm^{-1}) 3100, 2917, 1720, 1610, 1556, 1533, 1467, 1426, 1365, 1252, 1132, 768, 733, 629.

2-(3-bromophenyl)-5,7-dimethyl-3H-pyrrolizin-3-one **76**

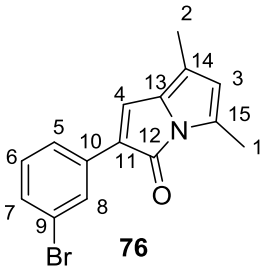

76

44% yield. M.P. 103-105 ^{o}C. ^{1}H NMR ($CDCl_3$, 500 MHz): δ 2.01 (s, 3H, H_2), 2.32 (s, 3H, H_1), 5.56 (s, 1H, H_3), 7.21 (t, 1H, J = 8.0 Hz, H_6), 7.24 (s, 1H, H_4), 7.37 (d, 1H, J = 8.0 Hz, H_7), 7.72 (d, 1H, J = 8.0 Hz, H_5), 7.93 (s, 1H, H_8). ^{13}C NMR ($CDCl_3$, 126 MHz): δ 11.4 (C_2), 12.4 (C_1), 116.2 (C_3), 122.7 (C_{10}), 124.4 (C_7), 125.8 (C_{15}), 128.2 (C_{11}), 128.8 (C_8), 129.1 (C_4), 130.0 (C_6), 130.3 (C_5), 131.8 (C_{13}), 134.0 (C_9), 135.2 (C_{14}), 165.1 (C_{12}). ESI-HRMS: *m/z* calculated for $C_{15}H_{13}(^{79}Br)NO$ $[M + H]^+$ 302.0175; observed 302.0172. FTIR: neat (cm^{-1}) 2932, 2367, 1712, 1663, 1587, 1530, 1475, 1364, 1297, 1256, 1136, 863, 782, 682.

2-(4-bromophenyl)-5,7-dimethyl-3H-pyrrolizin-3-one **77**

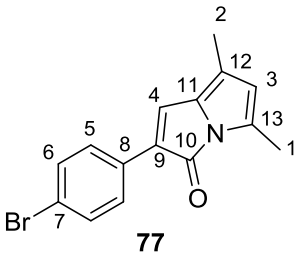

77

34% yield. M.P. 93-95 ^{o}C. ^{1}H NMR ($CDCl_3$, 500 MHz): δ 2.00 (s, 3H, H_2), 2.31 (s, 3H, H_1), 5.55 (s, 1H, H_3), 7.22 (s, 1H, H_4), 7.47 (d, 2H, *J* = 8.5 Hz, H_6), 7.65 (d, 2H, *J* = 8.5 Hz, H_5). ^{13}C NMR ($CDCl_3$, 126 MHz): δ 11.4 (C_2), 12.4 (C_1), 116.1 (C_3), 121.5 (C_9), 125.4 (C_{11}), 127.5 (C_5), 128.4 (C_4), 128.7 (C_7), 130.9 (C_8), 131.6 (C_6), 131.7 (C_{13}), 135.1 (C_{12}), 165.3 (C_{10}). ESI-HRMS: *m/z* calculated for $C_{15}H_{13}(^{79}Br)NO$ $[M + H]^+$ 302.0175; observed 302.0176. FTIR: neat (cm^{-1}) 2923, 2363, 1719, 1608, 1527, 1457, 1362, 1262, 1207, 1130, 1028, 881, 817, 803, 788.

5,7-dimethyl-2-o-tolyl-3H-pyrrolizin-3-one **78**

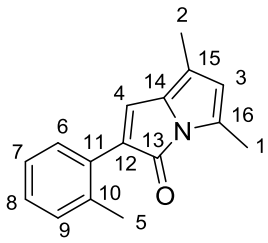

78

21% yield. M.P. 48-50 ^{o}C. ^{1}H NMR ($CDCl_3$, 500 MHz): δ 2.00 (s, 3H, H_2), 2.31 (s, 3H, H_1), 2.38 (s, 3H, H_5), 5.54 (s, 1H, H_3), 6.97 (s, 1H, H_4), 7.21 (m, 3H, $H_{7,8,9}$), 7.35 (d, 1H, H_6). ^{13}C NMR ($CDCl_3$, 126 MHz): δ 11.3 (C_2), 12.3 (C_1), 20.9 (C_5), 115.6 (C_3), 124.2 (C_{14}), 125.6 ($C_{7/8/9}$), 127.9 ($C_{7/8/9}$), 129.7 (C_6), 130.5 ($C_{7/8/9}$), 131.3, 131.7, 131.8 (C_4), 132.2, 134.7, 136.4, 165.5 (C_{13}). ESI-HRMS: *m/z* calculated for $C_{16}H_{16}NO$ $[M + H]^+$ 238.1232; observed 238.1220. FTIR: neat (cm^{-1}) 3308, 2925, 1707, 1375, 1231, 1138, 1081, 1033, 968, 923, 790.

5,7-dimethyl-2-m-tolyl-3H-pyrrolizin-3-one **79**

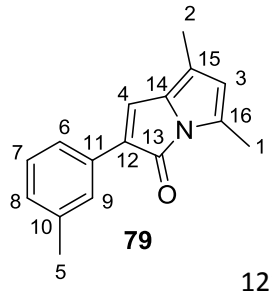

79

41% yield. M.P. 70-71 ^{o}C. ^{1}H NMR ($CDCl_3$, 500 MHz): δ 2.00 (s, 3H, H_2), 2.32 (s, 3H, H_1), 2.36 (s, 3H, H_5), 5.54 (s, 1H, H_3), 7.09 (d, 1H, *J* = 7.5 Hz, H_8), 7.20 (s, 1H, H_4), 7.25 (t, 1H, *J* =

7.5 Hz, H_7), 7.56 (d, 1H, *J* = 8.0 Hz, H_6), 7.60 (s, 1H, H_9). ^{13}C NMR ($CDCl_3$, 126 MHz): δ 11.4 (C_2), 12.4 (C_1), 21.5 (C_5), 115.8 (C_3), 123.1 (C_6), 124.4 (C_{14}), 126.7 (C_9), 128.1 (C_4), 128.39/128.41 (C_7, C_8), 130.1 (C_{12}), 131.9 (C_{11}), 132.0 (C_{15}), 134.6 (C_{16}), 138.0 (C_{10}), 165.7 (C_{13}). ESI-HRMS: *m/z* calculated for $C_{16}H_{16}NO$ $[M + H]^+$ 238.1232; observed 238.1225. FTIR: neat (cm^{-1}) 2915, 1707, 1600, 1533, 1442, 1368, 1276, 1172, 1091, 918, 862, 783, 776, 690.

5,7-dimethyl-2-p-tolyl-3H-pyrrolizin-3-one **80**

37% yield. M.P. 67-69 °C. ^1H NMR ($CDCl_3$, 500 MHz): δ 1.98 (s, 3H, H_2), 2.30 (s, 3H, H_1), 2.34 (s, 3H, H_5), 5.51 (s, 1H, H_3), 7.13 (s, 1H, H_4), 7.16 (d, 2H, *J* = 8.0 Hz, H_7), 7.66 (d, 2H, *J* = 8.0 Hz, H_6). ^{13}C NMR ($CDCl_3$, 126 MHz): δ 11.3 (C_2), 12.3 (C_1), 21.2 (C_5), 115.7 (C_3), 124.1 (C_{12}), 125.9 (C_6), 127.2 (C_4), 129.1 (C_7), 129.2 (C_9), 130.0 (C_{10}), 132.1 (C_{13}), 134.4 (C_{14}), 137.4 (C_8), 165.7 (C_{11}). ESI-HRMS: *m/z* calculated for $C_{16}H_{16}NO$ $[M + H]^+$ 238.1232; observed 238.1229. FTIR: neat (cm^{-1}) 2915, 1723, 1711, 1615, 1531, 1451, 1365, 1297, 1266, 1135, 966, 811.

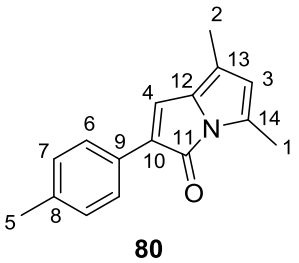

80

2-(2-methoxyphenyl)-5,7-dimethyl-3H-pyrrolizin-3-one **81**

33% yield. M.P. 96-98 °C. ^1H NMR ($CDCl_3$, 500 MHz): δ 2.01 (s, 3H, H_2), 2.31 (s, 3H, H_1), 3.89 (s, 3H, H_5), 5.53 (s, 1H, H_3), 6.99 (t, 1H, *J* = 7.5 Hz, H_7), 6.92 (d, 1H, *J* = 8.5 Hz, H_9), 7.23 (m, 1H, H_8), 7.55 (s, 1H, H_4), 8.05 (dd, 1H, *J* = 7.5, 1.0 Hz, H_6). ^{13}C NMR ($CDCl_3$, 126 MHz): δ 11.3 (C_2), 12.3 (C_1), 55.4 (C_5), 110.7 (C_9), 115.8 (C_3), 120.6 (C_7), 120.9 (C_{11}), 124.1 (C_{15}), 125.7 (C_{12}), 128.2 (C_8), 129.3 (C_6), 132.2 (C_4),

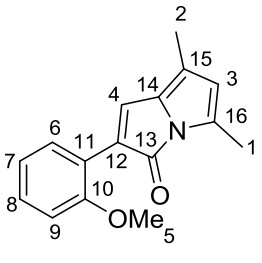

81

132.6 (C_{14}), 134.4 (C_{16}), 157.4 (C_{10}), 166.3 (C_{13}). ESI-HRMS: *m/z* calculated for $C_{16}H_{16}NO_2$ $[M + H]^+$ 254.1181; observed 254.1169. FTIR: neat (cm^{-1}) 2919, 2363, 1712, 1605, 1529, 1492, 1433, 1369, 1287, 1246, 1184, 1121, 1061, 1022.

2-(3-methoxyphenyl)-5,7-dimethyl-3H-pyrrolizin-3-one **82**

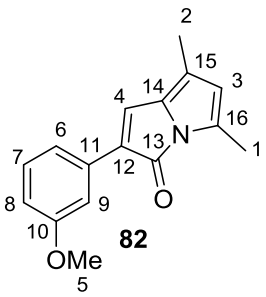

82

45% yield. M.P. 62-64 °C. ^{1}H NMR ($CDCl_3$, 500 MHz): δ 2.01 (s, 3H, H_2), 2.32 (s, 3H, H_1), 3.83 (s, 3H, H_5), 5.54 (s, 1H, H_3), 6.82 (dd, 1H, *J* = 8.0 / 2.5 Hz, H_8), 7.21 (s, 1H, H_4), 7.26 (t, 1H, *J* = 8.0 Hz, H_7), 7.33 (d, 1H, *J* = 8.0 Hz, H_6), 7.40 (s, 1H, H_9). ^{13}C NMR ($CDCl_3$, 126 MHz): δ 11.4 (C_2), 12.4 (C_1), 55.2 (C_5), 111.1 (C_9), 113.7 (C_8), 115.9 (C_3), 118.4 (C_6), 124.8 (C_{14}), 128.4 (C_4), 129.4 (C_7), 129.7 (C_{12}), 131.9 (C_{15}), 133.3 (C_{16}), 134.8 (C_{11}), 159.7 (C_{10}), 165.6 (C_{13}). ESI-HRMS: *m/z* calculated for $C_{16}H_{16}NO_2$ $[M + H]^+$ 254.1181; observed 254.1181. FTIR: neat (cm^{-1}) 2936, 1712, 1597, 1579, 1531, 1484, 1429, 1396, 1365, 1295, 1278, 1261, 1171, 1037.

2-(4-methoxyphenyl)-5,7-dimethyl-3H-pyrrolizin-3-one **83**

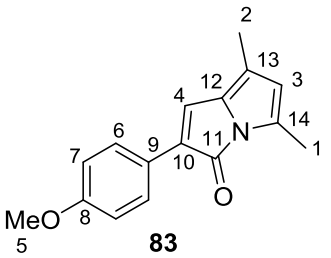

83

33% yield. M.P. 57-59 °C. ^{1}H NMR ($CDCl_3$, 500 MHz): δ 1.98 (s, 3H, H_2), 2.30 (s, 3H, H_1), 3.82 (s, 3H, H_5), 5.51 (s, 1H, H_3), 6.89 (d, 2H, *J* = 9.0, H_7), 7.07, (s, 1H, H_4), 7.72 (d, 2H, *J* = 9.0, H_7). ^{13}C NMR ($CDCl_3$, 126 MHz): δ 22.3 (C_2), 12.3 (C_1), 55.2 (C_5), 113.9 (C_7), 115.7 (C_3), 123.7 (C_{12}), 124.8 (C_9), 126.1 (C_4), 127.3 (C_6), 129.8 (C_{10}), 132.2 (C_{13}), 134.2 (C_{14}), 159.2 (C_8), 165.9 (C_{11}). ESI-HRMS: *m/z* calculated for $C_{16}H_{16}NO_2$ $[M + H]^+$ 254.1181; observed 254.1190. FTIR: neat (cm^{-1}) 2919, 1713, 1614, 1534, 1436, 1376, 1364, 1291, 1255, 1235, 1182, 1138, 1028.

5,7-dimethyl-2-(3-nitrophenyl)-3H-pyrrolizin-3-one **84**

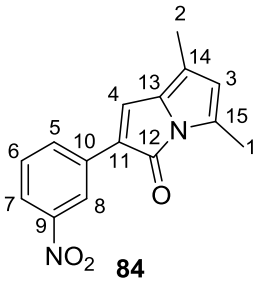

84

15% yield. M.P. 177-179 ^{o}C. ^{1}H NMR ($CDCl_3$, 500 MHz): δ 2.05 (s, 3H, H_2), 2.34 (s, 3H, H_1), 5.60 (s, 1H, H_3), 7.39 (s, 1H, H_4), 7.52 (t, 1H, *J* = 8.0 Hz, H_6), 8.09 (dd, 1H, *J* = 7.5, 1.5 Hz, H_7), 8.17 (d, 1H, *J* = 7.5 Hz, H_5), 8.60 (t, 1H, *J* = 1.5 Hz, H_8). ^{13}C NMR ($CDCl_3$, 126 MHz): δ 11.5 (C_2), 12.4 (C_1), 116.5 (C_3), 120.5 (C_8), 121.8 (C_7), 127.07/127.09 (C_{11}, C_{14}), 129.4 (C_6), 130.2 (C_4), 131.5 (C_5), 131.6 (C_{15}), 133.6 (C_{10}), 135.9 (C_{13}), 148.5 (C_9), 164.8 (C_{12}). ESI-HRMS: *m/z* calculated for $C_{17}H_{16}N_2O_4$ $[M + H]^+$ 269.0926; observed 269.0932. FTIR: neat (cm^{-1}) 2920, 1712, 1598, 1516, 1397, 1347, 1295, 1258, 1212, 1140, 1137, 1100.

5,7-dimethyl-2-(4-nitrophenyl)-3H-pyrrolizin-3-one **85**

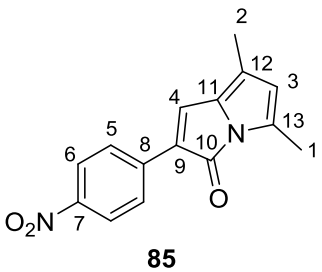

85

4% yield. M.P. 178-181 ^{o}C. ^{1}H NMR ($CDCl_3$, 500 MHz): δ 2.06 (s, 3H, H_2), 2.35 (s, 3H, H_1), 5.62 (s, 1H, H_3), 7.43 (s, 1H, H_4), 7.96 (d, 2H, *J* = 8.5 Hz, H_5), 8.21 (d, 2H, *J* = 8.5 Hz, H_6). ^{13}C NMR ($CDCl_3$, 126 MHz): δ 11.6 (C_2), 12.5 (C_1), 116.8 (C_3), 123.9 (C_6), 126.0 (C_5), 126.9 (C_9), 128.0 (C_{11}), 131.3 (C_4), 131.8 (C_{12}), 136.4 (C_{13}), 138.4 (C_8), 146.3 (C_7), 164.7 (C_{10}). ESI-HRMS: *m/z* calculated for $C_{17}H_{16}N_2O_4$ $[M + H]^+$ 269.0926; observed 269.0931. FTIR: neat (cm^{-1}) 3160, 2920, 2369, 1723, 1586, 1522, 1505, 1397, 1335, 1316, 1270, 1210, 1142, 1106.

5.3 Proof of Concept Chemical Reduction Reactions

Reduction with Fe(0) in CH_3COOH

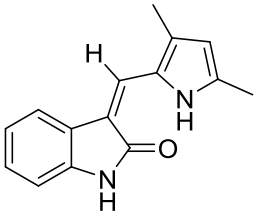

2

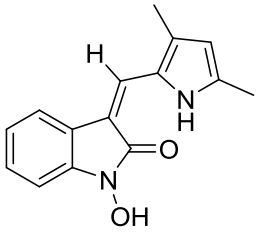

2-OH

Compound (*Z*)-**1** (17.5 mg, 0.035 mmol) was dissolved in a mixture of 1:1:1 glacial acetic acid:EtOH:water (3 mL). Reduced iron powder (23.1 mg, 0.41 mmol) was added and the reaction subjected to ultrasonic irradiation for 1 h at 30 °C or until complete consumption of starting material by TLC analysis (7:3 pet. spirit:acetone). The reaction mixture was filtered through a celite plug and washed with EtOH (10 mL). The filtrate was concentrated and taken into Et_2O (25 mL). The organic layer was washed with saturated $NaHCO_3$ (20 mL) and brine (20 mL), dried over anhydrous $MgSO_4$ and concentrated. The crude residue was purified by silica gel column chromatography (100% pet. spirit to 85:15 pet. spirit:acetone) to afford SU5416 **2** (4.2 mg, 50% yield) as a yellow solid and **2**-OH (2.5 mg, 28%) as a dark orange solid. A similar procedure using (*Z*)-**10** (50.8 mg, 0.161 mmol) also afforded SU5416 **2** (30.9 mg, 81.4%).

Reduction with $FeCl_3.6H_2O$/Zn (dust)

A mixture of ferric chloride hexahydrate (60.2 mg, 0.22 mmol), zinc dust (53.1 mg, 0.81 mmol) and (*Z*)-**1** (18.0 mg, 0.036 mmol) was stirred at room temperature in 1:1 DMF:water (2 mL). After 3 h or complete consumption of starting material by TLC analysis (7:3 pet. spirit:acetone), the reaction mixture was diluted with Et_2O (30 mL) and filtered through celite. The filtrate was added to a separating funnel and washed with brine (2 x 20 mL), dried over anhydrous $MgSO_4$ and concentrated. The crude

residues were purified by silica gel column chromatography (100% pet. spirit to 85:15 pet. spirit:acetone) to afford SU5416 **2** (4.3 mg, 50%) as a yellow solid, along with **2**-OH (2.2 mg, 24%) as a dark orange solid. A similar procedure using (*Z*)-**10** (53.3 mg, 0.169 mmol) also afforded SU5416 **2** (26.5 mg, 70%) and **2**-OH (8.6 mg, 20%).

Reduction with $NaBH_4$/Pd-C

To a stirred suspension of (*Z*)-**1** (16.8 mg, 0.034 mmol) and Pd-C (10 mg) in 2:1 MeOH:H_2O (2.5 mL), $NaBH_4$ (13.1 mg, 0.35 mmol) was added. The reaction mixture was stirred at rt for 30 mins before the catalyst was removed through a celite plug. The plug was washed with MeOH and the filtrates concentrated. The crude product was taken into Et_2O (25 mL), washed with brine (2 x 25 mL), dried over anhydrous $MgSO_4$ and concentrated. The crude residue was purified by column chromatography using a gradient from 100% pet. spirit to 85:15 pet. spirit:acetone to give SU5416 **2** (4.7 mg, 58%) as a yellow solid along with **2**-OH (1.8 mg, 21%) as a dark orange solid. A similar procedure using (*Z*)-**10** (52 mg, 0.17 mmol) afforded **2** (27 mg, 72%).

5.4 Rat Aortic Ring Angiogenesis Assay

Compounds were tested for angiogenesis inhibition by Anna Bezos in Professor Chris Parish's lab at the John Curtin School of Medical Research (ANU). Experiments were carried out in 48-well culture plates using the previously reported assay conditions with some modifications.[192] Briefly, thoracic aortas from female Fischer 344 rats were excised and the 2.5 cm long vessels placed in Hank's buffered salt solution (HBSS) media containing 2.5 µg/mL amphotericin B and cross-sectioned at 1 mm intervals. In the angiogenesis assay, 15 mL of bovine thrombin (50 NIH unit/mL in 0.15M NaCl)

was added to each well, followed by 0.5 mL per well of 3 mg/mL bovine fibrinogen in Medium 199. The thrombin and fibrinogen were mixed rapidly and one aortic section was quickly placed in the centre of the well before clot formation. Fibrin gel formation usually occurred within 0.5 min, leaving the vessel fragment suspended in the gel.

On gel formation, 0.5 mL of Medium 199 supplemented with 20% foetal calf serum (FCS), 0.1% 6-aminohexanoic acid, L-glutamine, and antibiotics (gentamicin sulfate and amphotericin B) and test compound were added to each well. Six replicate cultures were examined for each concentration of compound. Vessels were cultured at 37 ^{o}C in 5% CO_2 in a humidified environment for 7 days, with the medium being changed on Day 4. On Day 5, the percentage of the field of view occupied by vessel outgrowths (F.O.V. occupancy %) was used as a quantitative measure of angiogenesis (inhibition) relative to control (no compound added).

5.5 HUVEC Tube Formation Assay

The endothelial tube formation assay was performed in accordance with the vendor's recommendations.[219] Briefly, adherent human umbilical vein endothelial cells (C-003-5C, Life Technologies) were seeded at 2.5 x 10^3 cells/cm^2 in standard T75 flasks and incubated at 37 ºC and 5% CO_2 in a humidified cell culture incubator with Medium 200 supplemented with low serum growth supplement (LSGS, Life Technologies). Media was refreshed every 36 hours and cultures were passaged at 80% confluency (5-6 days). HUVECs were used for assays between passages 2-4.

Geltrex was thawed overnight at 4 ^{o}C and 50-100 µL was added to coat the base of 24-well culture plates and the plates incubated at 37 ^{o}C for 1 hour to set the gel. Cells were seeded at 4 x 10^3 cells/200 µL in LSGS-supplemented Medium 200 and incubated for 2

hours at 37 ^{o}C to allow adherence. Compounds were added to give a final concentration of 10 uM in LSGS-supplemented Medium 200 containing 1% DMSO. Cells were incubated at 37 ^{o}C for a further 5 hours before the media was carefully aspirated and replaced with PBS for visualisation by optical microscopy.

A series of 3-5 images of each well were taken using a microscope camera at 20x magnification and used for the analysis. Experiments were performed twice with individual cultures of HUVECs, giving 6-10 images for each compound. Angiogenesis analysis was performed according to Aranda et al.[218] Briefly, total cell count, sprouting (i.e. differentiating, elongated) cells, connected cells, enclosed polygons and complex polygons (those with 2-3 cells thick edges and those with 4+) were counted and each image was scored according to the following equation:

$$Score = (0, 1\ or\ 2) + \frac{[(sprouting\ cells)1 + (connected\ cells)2 + (polygons)3]}{total\ cell\ count}$$

Where 0 is no complex polygons, 1 is at least one polygon with walls 2-3 cells thick and 2 is at least one polygon with walls 4+ cells thick. 1% DMSO in LSGS-supplemented Medium 200 was used as a positive control (vehicle) and 10 µM sunitinib malate was used as a negative control. Experiments containing test compounds were scored as a percentage of vehicle.

Chapter 6

Appendices

6.1 Appendix 1

6.1.1 Crystallographic data

(a) Compound (*Z*)-**5**.

$C_{15}H_{14}N_2O_4$, M_r = 286.29, T = 150 K; monoclinic, space group $P2_1/n$, Z = 4; a = 13.8996 (1) Å, b = 7.3274 (1) Å, c = 14.6266 (1) Å; β = 113.1054 (9)°; V = 1370.19 (2) Å^3; D_x = 1.388 g.cm^{-3}; 20464 reflections measured (θ = 4-72°) merged to 2692 unique data; R = 0.033 (for 2610 data with $I > 2\sigma(I)$), R_w = 0.089 (all data); S = 1.01.

(b) Compound **14**.

$C_{15}H_{12}N_2O_3$, M_r = 268.27, T = 150 K; triclinic, space group $P1$, Z = 2; a = 7.9103 (7) Å, b = 8.2020 (4) Å, c = 10.8545 (9) Å; α = 79.807 (6)°; β = 69.688 (8)°; γ = 87.445 (6)°; V = 649.92 (9) Å^3; D_x = 1.371 g.cm^{-3}; 9934 reflections measured (θ = 4-72°) merged to 2534 unique data; R = 0.059 (for 2263 data with $I > 2\sigma(I)$), R_w = 0.178 (all data); S = 1.01.

(c) Compound (*Z*)-**13**.

$C_{18}H_{18}N_2O_4$, M_r = 326.35, T = 200 K; monoclinic, space group $P2_1/c$, Z = 4; a = 12.5669 (4) Å, b = 7.9086 (3) Å, c = 17.6200 (4) Å; β = 103.730 (2)°; V = 1701.15 (6) Å^3; D_x = 1.274 g.cm^{-3}; 32664 reflections measured (2θ = 5-55°) merged to 3903 unique data; R = 0.053 (for 2656 data with $I > 2\sigma(I)$), R_w = 0.147 (all data); S = 0.95.

(d) Compound (*E*)-**13**.

$C_{18}H_{18}N_2O_4$, M_r = 326.35, T = 298(2) K; triclinic, space group P-1, Z = 2; a = 8.4326 (4) Å, b = 10.2147 (4) Å , c = 11.0598 (6) Å; α = 72.485 (3)°, β = 76.605 (2)°, γ = 71.312 (3)°; V = 850.89 (7) Å^3; D_x = 1.274 g.cm^{-3}; 7615 reflections measured (2θ = 4-54.2°) merged to 3674 unique data R = 0.064 (for 2849 data with $I > 2\sigma(I)$), R_w = 0.187 (all data); S = 0.99.

(e) Compound **15**.

$C_{22}H_{22}N_4O$, M_r = 358.44, T = 150 K; monoclinic, space group $P2_1/n$, Z = 4; a = 10.7644 (2) Å, b = 7.0938 (2) Å, c = 23.6831 (4) Å; β = 101.3654 (19)°; V = 1772.99 (7) Å^3; D_x = 1.343 g.cm^{-3}; 8260 reflections measured (θ = 5-72°) merged to 3501 unique data; R = 0.036 (for 3202 data with $I > 2\sigma(I)$), R_w = 0.097 (all data); S = 0.99.

(f) Compound **17**.

$C_{14}H_{12}N_2O_2$, M_r = 240.26, T = 150 K; orthorhombic, space group $Pca2_1$, Z = 8; a = 26.7517 (16) Å, b = 5.4982 (5) Å, c = 15.7489 (16) Å; V = 2316.4 (3) Å^3; D_x = 1.378 g.cm^{-3}; 8621 reflections measured (θ = 3-69°) merged to 2285 unique data; R = 0.080 (for 1797 data with $I > 2\sigma(I)$), R_w = 0.183 (all data); S = 1.04.

6.1.2 Crystal Structure Determination

Images of (*Z*)-**13** and (*E*)-**13** were measured on Nonius Kappa CCD diffractometers (Mo *K*α radiation, graphite monochromator, λ 0.71073Å) and data were extracted using the *DENZO* package.[221] Images of (*Z*)-**5**, **14**, **15** and **17** were measured on Agilent SuperNova diffractometers (Cu *K*α radiation, graphite or mirror monochromators, λ 1.54180 Å) and data were extracted using the *CrysAlis PRO* package.[222]

For (*Z*)-**13**, (*Z*)-**5**, **14**, **15** and **17** structure solution was by direct methods (SIR92)[223] and the structure was refined using the *CRYSTALS* program package.[224] For (*E*)-**13**, structure solution was by direct methods (*SIR97*)[225] and the structure was refined using the *SHELXL-97* program package.[226] Atomic coordinates, bond lengths and angles, and displacement parameters of (*Z*)-**13** and (*E*)-**13** have been deposited at the Cambridge Crystallographic Data Centre (CCDC accession numbers 905343 and 905344 respectively).

6.2 Appendix 2

(a)

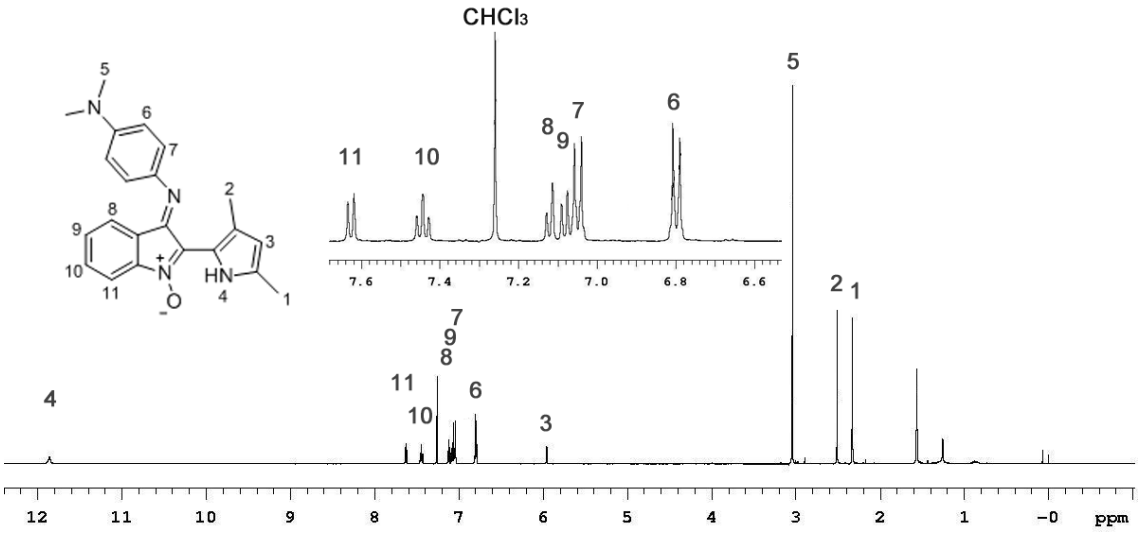

(b)

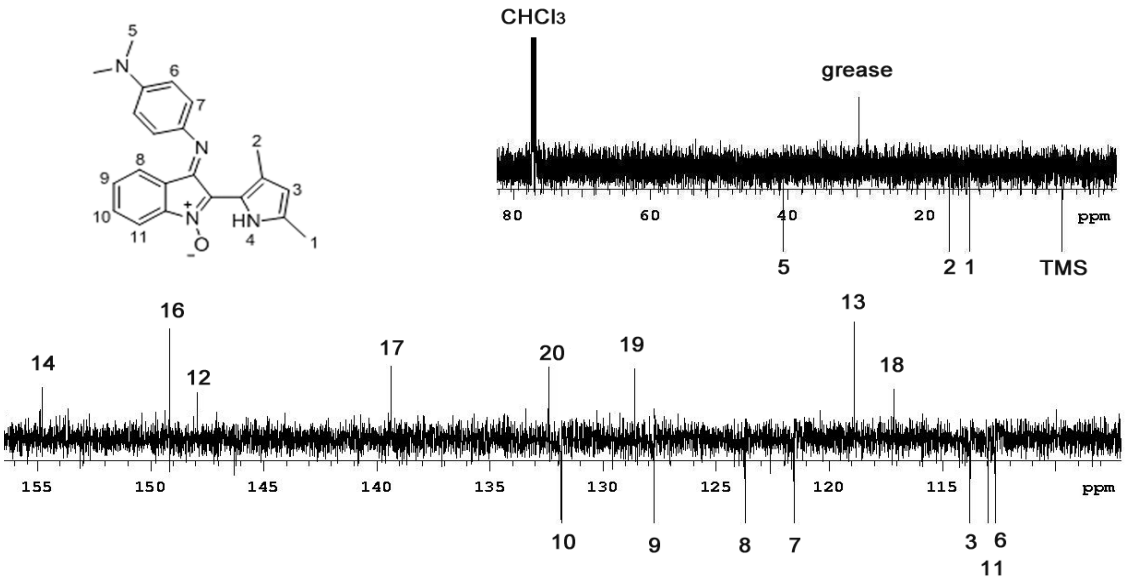

Appendix 2. NMR spectra of compound **15**. (a) ^{1}H NMR spectrum of **15**; (b) ^{13}C NMR spectrum of **15**. Assignments were derived from 2D NMR experiments, including gCOSY, NOESY, gHSQC and gHMBC.

Chapter 7

References

1. Australian Institute of Health and Welfare. *Cancer in Australia: an overview, 2012*. (2012).

2. Australian Institute of Health and Welfare. Australian Cancer Incidence and Mortality (ACIM) books: All cancers combined. (2014). at <http://www.aihw.gov.au/acim-books>

3. Zaenker, K. S. & Entschladen, F. Paving Roads for New Drugs in Oncology. *Recent Pat. Anticancer. Drug Discov.* **4,** 137–145 (2009).

4. Amit, I. *et al.* A module of negative feedback regulators defines growth factor signaling. *Nat. Genet.* **39,** 503–12 (2007).

5. Hanahan, D. & Weinberg, R. a. Hallmarks of cancer: the next generation. *Cell* **144,** 646–74 (2011).

6. *Cancer Management: A Multidisciplinary Approach*. (UBM Medica, 2011).

7. DeVita, V. T. & Chu, E. A history of cancer chemotherapy. *Cancer Res.* **68,** 8643–53 (2008).

8. Midgley, R. & Kerr, D. J. Adjuvant chemotherapy for stage II colorectal cancer: the time is right! *Nat Clin Pr. Oncol* **2,** 364–369 (2005).

9. Neoptolemos, J. P. Adjuvant therapy in pancreatic cancer: historical and current perspectives. *Ann. Oncol.* **14,** 675–692 (2003).

10. Kent, E. C. & Hussain, M. H. Neoadjuvant Therapy for Prostate Cancer: An Oncologist's Perspective. *Rev. Urol.* **5 Suppl 3,** S28–37 (2003).

11. Thompson, a M. & Moulder-Thompson, S. L. Neoadjuvant treatment of breast cancer. *Ann. Oncol.* **23 Suppl 1,** x231–6 (2012).

12. Archer, V. R., Billingham, L. J. & Cullen, M. H. Palliative chemotherapy: no longer a contradiction in terms. *Oncologist* **4,** 470–7 (1999).

13. Malayeri, R., Pirker, R. & Huber, H. New Drugs in the Palliative Chemotherapy of Advanced Non-Small-Cell Lung Cancer. *Oncol. Res. Treat.* **24,** 416–421 (2001).

14. Wöhrer, S. S., Raderer, M. & Hejna, M. Palliative chemotherapy for advanced gastric cancer. *Ann. Oncol.* **15 ,** 1585–1595 (2004).

15. Löwenberg, B. *et al.* On the value of intensive remission-induction chemotherapy in elderly patients of 65+ years with acute myeloid leukemia: a randomized phase III study of the European Organization for Research and Treatment of Cancer Leukemia Group. *J. Clin. Oncol.* **7 ,** 1268–1274 (1989).

16. Stone, R. M. Consolidation chemotherapy for adults with AML in first remission: is there a best choice? *J. Clin. Oncol.* **31,** 2067–9 (2013).

17. Larson, R. a *et al.* A five-drug remission induction regimen with intensive consolidation for adults with acute lymphoblastic leukemia: cancer and leukemia group B study 8811. *Blood* **85,** 2025–37 (1995).

18. Sanz, M., Martín, G. & Coco, F. Choice of chemotherapy in induction, consolidation and maintenance in acute promyelocytic leukaemia. *Best Pract. Res. Clin. …* **16,** 433–451 (2003).

19. Grossi, F. *et al.* Sequential, alternating, and maintenance/consolidation chemotherapy in advanced non-small cell lung cancer: a review of the literature. *Oncologist* **12,** 451–64 (2007).

20. Tallman, M. S. *et al.* Pretransplantation consolidation chemotherapy decreases leukemia relapse after autologous blood and bone marrow transplants for acute myelogenous leukemia in first remission. *Biol. Blood Marrow Transplant.* **12,** 204–16 (2006).

21. American Cancer Society. Non-hodgkin lymphoma. at <http://www.cancer.org/acs/groups/cid/documents/webcontent/003126-pdf.pdf>

22. Widakowich, C., de Castro, G., de Azambuja, E., Dinh, P. & Awada, A. Review: side effects of approved molecular targeted therapies in solid cancers. *Oncologist* **12,** 1443–55 (2007).

23. U.S. Food and Drug Administration. Hematology/Oncology (Cancer) Approvals & Safety Notifications. at <http://www.fda.gov/drugs/informationondrugs/approveddrugs/ucm279174.htm>

24. Dobbelstein, M. & Moll, U. Targeting tumour-supportive cellular machineries in anticancer drug development. *Nat. Rev. Drug Discov.* **13,** 179–96 (2014).

25. Ramaswamy, S. Rational Design of Cancer-Drug Combinations. *N. Engl. J. Med.* **357,** 299–300 (2007).

26. Zimmermann, G. R., Lehár, J. & Keith, C. T. Multi-target therapeutics: when the whole is greater than the sum of the parts. *Drug Discov. Today* **12,** 34–42 (2007).

27. Eastman, A. The formation, isolation and characterization of DNA adducts produced by anticancer platinum complexes. *Pharmacol. Ther.* **34,** 155–166 (1987).

28. Siddik, Z. H. Cisplatin: mode of cytotoxic action and molecular basis of resistance. *Oncogene* **22,** 7265–79 (2003).

29. An alkylating agent for multiple myeloma: Melphalan (alkeran). *JAMA* **191,** 547–549 (1965).

30. Adamietz, I. A., Schober, C., Schulte, R. W. M., Peest, D. & Renner, K. Palliative radiotherapy in plasma cell myeloma. *Radiother. Oncol.* **20,** 111–116 (2014).

31. Longley, D. B., Harkin, D. P. & Johnston, P. G. 5-Fluorouracil: Mechanisms of Action and Clinical Strategies. *Nat. Rev. Cancer* **3,** 330–8 (2003).

32. Santi, D. V, McHenry, C. S. & Sommer, H. Mechanism of interaction of thymidylate synthetase with 5-fluorodeoxyuridylate. *Biochemistry* **13,** 471–481 (1974).

33. American Cancer Society. Fluorouracil. at <http://www.cancer.gov/cancertopics/druginfo/fluorouracil>

34. Wang, L.-M., Courtland White, J. & Capizzi, R. The effect of ara-C-induced inhibition of DNA synthesis on its cellular pharmacology. *Cancer Chemother. Pharmacol.* **25,** 418–424 (1990).

35. Major, P. P., Egan, E. M., Herrick, D. J. & Kufe, D. W. Effect of ara-C incorporation on deoxyribonucleic acid synthesis in cells. *Biochem. Pharmacol.* **31,** 2937–2940 (1982).

36. Hryniuk, W. The mechanism of action of methotrexate in cultured L5178Y leukemia cells. *Cancer Res.* **35,** 1085–1092 (1975).

37. Heinemann, V., Hertel, L. W., Grindey, G. B. & Plunkett, W. Comparison of the Cellular Pharmacokinetics and Toxicity of 2′, 2′-Difluorodeoxycytidine and 1-β-d-Arabinofuranosylcytosine. *Cancer Res.* **48,** 4024–4031 (1988).

38. Pereira, S., Fernandes, P. A. & Ramos, M. J. Mechanism for ribonucleotide reductase inactivation by the anticancer drug gemcitabine. *J. Comput. Chem.* **25,** 1286–94 (2004).

39. Cerqueira, N. M. F. S. a, Fernandes, P. a & Ramos, M. J. Understanding ribonucleotide reductase inactivation by gemcitabine. *Chemistry* **13,** 8507–15 (2007).

40. Bergman, A. M. *et al.* In vivo induction of resistance to gemcitabine results in increased expression of ribonucleotide reductase subunit M1 as the major determinant. *Cancer Res.* **65,** 9510–6 (2005).

41. Burris, H. A. *et al.* Improvements in survival and clinical benefit with gemcitabine as first-line therapy for patients with advanced pancreas cancer: a randomized trial. *J. Clin. Oncol.* **15 ,** 2403–2413 (1997).

42. Sandler, a & Ettinger, D. S. Gemcitabine: single-agent and combination therapy in non-small cell lung cancer. *Oncologist* **4,** 241–51 (1999).

43. Hussain, S. A. & James, N. D. The systemic treatment of advanced and metastatic bladder cancer. *Lancet Oncol.* **4,** 489–497 (2003).

44. Tacar, O., Sriamornsak, P. & Dass, C. R. Doxorubicin: an update on anticancer molecular action, toxicity and novel drug delivery systems. *J. Pharm. Pharmacol.* **65,** 157–70 (2013).

45. Wolters Kluwer Health Inc. Doxorubicin. at <http://www.drugs.com/pro/doxorubicin.html>

46. Frederick, C. A. *et al.* Structural comparison of anticancer drug-DNA complexes: adriamycin and daunomycin. *Biochemistry* **29,** 2538–49 (1990).

47. Chan, K.-S., Koh, C.-G. & Li, H.-Y. Mitosis-targeted anti-cancer therapies: where they stand. *Cell Death Dis.* **3,** e411 (2012).

48. Jordan, M. & Wilson, L. Microtubules as a target for anticancer drugs. *Nat. Rev. Cancer* **4,** 253–265 (2004).

49. Xi, G. *et al.* Autophagy inhibition promotes paclitaxel-induced apoptosis in cancer cells. *Cancer Lett.* **307,** 141–8 (2011).

50. Himes, R., Kersey, R., Heller-Bettinger, I. & Samson, F. Action of the vinca alkaloids vincristine, vinblastine, and desacetyl vinblastine amide on microtubules in vitro. *Cancer Res.* 3798–3802 (1976).

51. Rowinsky, E. K. & Donehower, R. C. Paclitaxel (Taxol). *N. Engl. J. Med.* **332,** 1004–1014 (1995).

52. Rowinksy, E. in *Holland-Frei Cancer Med. 6th Ed.* (2003).

53. Gourdie, T. a *et al.* DNA-directed alkylating agents. 1. Structure-activity relationships for acridine-linked aniline mustards: consequences of varying the reactivity of the mustard. *J. Med. Chem.* **33,** 1177–86 (1990).

54. Yamagata, M. & Tannock, I. F. The chronic administration of drugs that inhibit the regulation of intracellular pH: in vitro and anti-tumour effects. *Br. J. Cancer* **73,** 1328–34 (1996).

55. Houtgraaf, J. H., Versmissen, J. & van der Giessen, W. J. A concise review of DNA damage checkpoints and repair in mammalian cells. *Cardiovasc. Revasc. Med.* **7,** 165–72 (2004).

56. Sancar, A., Lindsey-Boltz, L. A., Unsal-Kaçmaz, K. & Linn, S. Molecular mechanisms of mammalian DNA repair and the DNA damage checkpoints. *Annu. Rev. Biochem.* **73,** 39–85 (2004).

57. Levine, a J. P53, the Cellular Gatekeeper for Growth and Division. *Cell* **88,** 323–31 (1997).

58. Soussi, T., Ishioka, C., Claustres, M. & Béroud, C. Locus-specific mutation databases: pitfalls and good practice based on the p53 experience. *Nat. Rev. Cancer* **6,** 83–90 (2006).

59. Wang, Z. & Sun, Y. Targeting p53 for Novel Anticancer Therapy. *Transl. Oncol.* **3,** 1–12 (2010).

60. Vazquez, A., Bond, E. E., Levine, A. J. & Bond, G. L. The genetics of the p53 pathway, apoptosis and cancer therapy. *Nat. Rev. Drug Discov.* **7,** 979–87 (2008).

61. Wilson, J. M. Gendicine: the first commercial gene therapy product. *Hum. Gene Ther.* **16,** 1014–5 (2005).

62. Gabrilovich, D. INGN 201 (Advexin®): adenoviral p53 gene therapy for cancer. *Expert Opin. Biol. Ther.* **6,** 823–832 (2006).

63. De Lange, T. Shelterin: the protein complex that shapes and safeguards human telomeres. *Genes Dev.* **19,** 2100–10 (2005).

64. Diotti, R. & Loayza, D. Shelterin complex and associated factors at human telomeres. *Nucleus* **2,** 119–35 (2011).

65. Grandin, N. & Charbonneau, M. Protection against chromosome degradation at the telomeres. *Biochimie* **90,** 41–59 (2008).

66. Hayflick, L. The limited in vitro lifetime of human diploid cell strains. *Exp. Cell Res.* **37,** 614–636 (1965).

67. Shay, J. W. & Bacchetti, S. A survey of telomerase activity in human cancer. *Eur. J. Cancer* **33,** 787–791 (2014).

68. Bryan, T. M., Englezou, a, Gupta, J., Bacchetti, S. & Reddel, R. R. Telomere elongation in immortal human cells without detectable telomerase activity. *EMBO J.* **14,** 4240–8 (1995).

69. De Cian, A. *et al.* Targeting telomeres and telomerase. *Biochimie* **90,** 131–55 (2008).

70. Strahl, C. & Blackburn, E. H. Effects of reverse transcriptase inhibitors on telomere length and telomerase activity in two immortalized human cell lines. *Mol. Cell. Biol.* **16,** 53–65 (1996).

71. Datta, A. *et al.* Persistent inhibition of telomerase reprograms adult T-cell leukemia to p53-dependent senescence. *Blood* **108,** 1021–9 (2006).

72. Röth, A., Harley, C. B. & Baerlocher, G. M. Imetelstat (GRN163L)--telomerase-based cancer therapy. *Recent results cancer Res.* **184,** 221–34 (2010).

73. Li, S., Nosrati, M. & Kashani-Sabet, M. Knockdown of telomerase RNA using hammerhead ribozymes and RNA interference. *Methods Mol. Biol.* **405,** 113–31 (2007).

74. Chen, C., Wang, Q., Liu, J., Hao, Y. & Tan, Z. Contribution of Telomere G-Quadruplex Stabilization to the Inhibition of Telomerase-Mediated Telomere Extension by Chemical Ligands. *J. Am. Chem. Soc.* **133,** 15036–15044 (2011).

75. Chambers, A. F. The metastatic process: basic research and clinical implications. *Oncol. Res.* **11,** 161–8 (1999).

76. Kim, J. & Dang, C. V. Cancer's molecular sweet tooth and the Warburg effect. *Cancer Res.* **66,** 8927–30 (2006).

77. Swietach, P., Vaughan-Jones, R. D. & Harris, A. L. Regulation of tumor pH and the role of carbonic anhydrase 9. *Cancer Metastasis Rev.* **26,** 299–310 (2007).

78. Colen, C. B. *et al.* Metabolic Targeting of Lactate Efflux by Malignant Glioma Inhibits Invasiveness and Induces Necrosis : An In Vivo Study 1. **13,** 620–632 (2011).

79. Estrella, V. *et al.* Acidity generated by the tumor microenvironment drives local invasion. *Cancer Res.* **73,** 1524–35 (2013).

80. Kennedy, K. & Dewhirst, M. Tumor metabolism of lactate: the influence and therapeutic potential for MCT and CD147 regulation. *Futur. Oncol.* **6,** 1–32 (2010).

81. Danø, K. *et al.* Plasminogen activation and cancer. *Thromb. Haemost.* 676–681 (2005). doi:10.1160/TH05-01-0054

82. Mohamed, M. M. & Sloane, B. F. Cysteine cathepsins: multifunctional enzymes in cancer. *Nat. Rev. Cancer* **6,** 764–75 (2006).

83. Coussens, L. M. & Werb, Z. Matrix metalloproteinases and the development of cancer. *Chem. Biol.* **3,** 895–904 (1996).

84. Umeda, T., Eguchi, Y., Okino, K., Kodama, M. & Hattori, T. Cellular localization of urokinase-type plasminogen activator, its inhibitors, and their mRNAs in breast cancer tissues. *J. Pathol.* **183,** 388–97 (1997).

85. Overall, C. M. & López-Otín, C. Strategies for MMP inhibition in cancer: innovations for the post-trial era. *Nat. Rev. Cancer* **2,** 657–72 (2002).

86. Goldstein, L. J. Experience in Phase I Trials and an Upcoming Phase II Study with uPA Inhibitors in Metastatic Breast Cancer. *Breast Care (Basel).* **3,** 25–28 (2008).

87. Ertongur, S. *et al.* Inhibition of the invasion capacity of carcinoma cells by WX-UK1, a novel synthetic inhibitor of the urokinase-type plasminogen activator system. *Int. J. Cancer* **110,** 815–24 (2004).

88. Witsch, E., Sela, M. & Yarden, Y. Roles for growth factors in cancer progression. *Physiology (Bethesda).* **25,** 85–101 (2010).

89. Lemmon, M. A. & Schlessinger, J. Cell signaling by receptor tyrosine kinases. *Cell* **141,** 1117–34 (2010).

90. Xu, Y., Richert, N., Ito, S., Merlino, G. T. & Pastan, I. R. A. Characterization of epidermal growth factor receptor gene expression in malignant and normal human cell lines Biochemistry : **81,** 7308–7312 (1984).

91. Yarden, Y. The EGFR family and its ligands in human cancer : signalling mechanisms and therapeutic opportunities. **37,** 3–8 (2001).

92. Attisano, L. & Wrana, J. L. Signal transduction by the TGF-beta superfamily. *Science* **296,** 1646–7 (2002).

93. Elliott, R. L. & Blobe, G. C. Role of transforming growth factor Beta in human cancer. *J. Clin. Oncol.* **23,** 2078–93 (2005).

94. Li, H., Xu, D., Li, J., Berndt, M. C. & Liu, J.-P. Transforming growth factor beta suppresses human telomerase reverse transcriptase (hTERT) by Smad3 interactions with c-Myc and the hTERT gene. *J. Biol. Chem.* **281,** 25588–600 (2006).

95. Hudis, C. A. Trastuzumab--mechanism of action and use in clinical practice. *N. Engl. J. Med.* **357,** 39–51 (2007).

96. Higa, G. M. & Abraham, J. Lapatinib in the treatment of breast cancer. *Expert Rev. Anticancer Ther.* **7,** 1183–92 (2007).

97. Jordan, V. C. Tamoxifen (ICI46,474) as a targeted therapy to treat and prevent breast cancer. *Br. J. Pharmacol.* **147 Suppl,** S269–76 (2006).

98. Fradet, Y. Bicalutamide (Casodex) in the treatment of prostate cancer. *Expert Rev. Anticancer Ther.* **4,** 37–48 (2004).

99. Griffioen, a W. & Molema, G. Angiogenesis: potentials for pharmacologic intervention in the treatment of cancer, cardiovascular diseases, and chronic inflammation. *Pharmacol. Rev.* **52,** 237–68 (2000).

100. Fox, S. B., Gasparini, G. & Harris, a L. Angiogenesis: pathological, prognostic, and growth-factor pathways and their link to trial design and anticancer drugs. *Lancet Oncol.* **2,** 278–89 (2001).

101. Kesisis, G., Broxterman, H. & Giaccone, G. Angiogenesis inhibitors. Drug selectivity and target specificity. *Curr. Pharm. Des.* **13,** 2795–2809 (2007).

102. Vaupel, P. & Harrison, L. Tumor hypoxia: causative factors, compensatory mechanisms, and cellular response. *Oncologist* **9 Suppl 5,** 4–9 (2004).

103. Vaupel, P. & Mayer, A. Hypoxia in cancer: significance and impact on clinical outcome. *Cancer Metastasis Rev.* **26,** 225–39 (2007).

104. Unruh, A. *et al.* The hypoxia-inducible factor-1 alpha is a negative factor for tumor therapy. *Oncogene* **22,** 3213–20 (2003).

105. Sullivan, R. & Graham, C. H. Hypoxia-driven selection of the metastatic phenotype. *Cancer Metastasis Rev.* **26,** 319–31 (2007).

106. Kim, J., Gao, P. & Dang, C. V. Effects of hypoxia on tumor metabolism. *Cancer Metastasis Rev.* **26,** 291–8 (2007).

107. Liao, D. & Johnson, R. S. Hypoxia: a key regulator of angiogenesis in cancer. *Cancer Metastasis Rev.* **26,** 281–90 (2007).

108. Denny, W. The role of hypoxia-activated prodrugs in cancer therapy. *Lancet Oncol.* **1,** 25–29 (2000).

109. Semenza, G. L. & Wang, G. L. A nuclear factor induced by hypoxia via de novo protein synthesis binds to the human erythropoietin gene enhancer at a site required for transcriptional activation. *Mol. Cell. Biol.* **12,** 5447–54 (1992).

110. Wang, G. L., Jiang, B. H., Rue, E. a & Semenza, G. L. Hypoxia-inducible factor 1 is a basic-helix-loop-helix-PAS heterodimer regulated by cellular O2 tension. *Proc. Natl. Acad. Sci. U. S. A.* **92,** 5510–4 (1995).

111. Semenza, G. L. Hydroxylation of HIF-1: oxygen sensing at the molecular level. *Physiology (Bethesda).* **19,** 176–82 (2004).

112. Iyer, N. V *et al.* Cellular and developmental control of O2 homeostasis by hypoxia-inducible factor 1 alpha. *Genes Dev.* **12,** 149–62 (1998).

113. Lukashev, D., Ohta, a & Sitkovsky, M. Hypoxia-dependent anti-inflammatory pathways in protection of cancerous tissues. *Cancer Metastasis Rev.* **26,** 273–9 (2007).

114. Zhong, H. *et al.* Overexpression of hypoxia-inducible factor 1alpha in common human cancers and their metastases. *Cancer Res.* **59,** 5830–5 (1999).

115. Melillo, G. Targeting hypoxia cell signaling for cancer therapy. *Cancer Metastasis Rev.* **26,** 341–52 (2007).

116. Harada, H. *et al.* The Akt/mTOR pathway assures the synthesis of HIF-1alpha protein in a glucose- and reoxygenation-dependent manner in irradiated tumors. *J. Biol. Chem.* **284,** 5332–42 (2009).

117. Agani, F. & Jiang, B.-H. Oxygen-independent regulation of HIF-1: novel involvement of PI3K/AKT/mTOR pathway in cancer. *Curr. Cancer Drug Targets* **13,** 245–51 (2013).

118. Kilic-Eren, M., Boylu, T. & Tabor, V. Targeting PI3K/Akt represses Hypoxia inducible factor-1α activation and sensitizes Rhabdomyosarcoma and Ewing's sarcoma cells for apoptosis. *Cancer Cell Int.* **13,** 36 (2013).

119. Mottet, D. *et al.* Regulation of hypoxia-inducible factor-1alpha protein level during hypoxic conditions by the phosphatidylinositol 3-kinase/Akt/glycogen

synthase kinase 3beta pathway in HepG2 cells. *J. Biol. Chem.* **278,** 31277–85 (2003).

120. Hassan, B., Akcakanat, A., Holder, A. M. & Meric-Bernstam, F. Targeting the PI3-kinase/Akt/mTOR signaling pathway. *Surg. Oncol. Clin. N. Am.* **22,** 641–64 (2013).

121. Rubio-Viqueira, B. & Hidalgo, M. Targeting mTOR for cancer treatment. *Curr. Opin. Investig. Drugs* **7,** 501–12 (2006).

122. Yancopoulos, G. D. *et al.* Vascular-specific growth factors and blood vessel formation. *Nature* **407,** 242–8 (2000).

123. Gschwind, A., Fischer, O. M. & Ullrich, A. The discovery of receptor tyrosine kinases: targets for cancer therapy. *Nat. Rev. Cancer* **4,** 361–70 (2004).

124. Ferrara, N. Role of vascular endothelial growth factor in the regulation of angiogenesis. *Kidney Int.* **56,** 794–814 (1999).

125. Jeltsch, M., Leppänen, V.-M., Saharinen, P. & Alitalo, K. Receptor tyrosine kinase-mediated angiogenesis. *Cold Spring Harb. Perspect. Biol.* **5,** (2013).

126. Morabito, A., De Maio, E., Di Maio, M., Normanno, N. & Perrone, F. Tyrosine kinase inhibitors of vascular endothelial growth factor receptors in clinical trials: current status and future directions. *Oncologist* **11,** 753–64 (2006).

127. Gotink, K. J. & Verheul, H. M. W. Anti-angiogenic tyrosine kinase inhibitors: what is their mechanism of action? *Angiogenesis* **13,** 1–14 (2010).

128. Pazdur, R. FDA Approval for Bevacizumab. at <http://www.cancer.gov/cancertopics/druginfo/fda-bevacizumab>

129. Goldman, J. M. & Melo, J. V. Chronic myeloid leukemia--advances in biology and new approaches to treatment. *N. Engl. J. Med.* **349,** 1451–64 (2003).

130. Novartis. Gleevec Prescribing Information. (2008). at <http://www.accessdata.fda.gov/drugsatfda_docs/label/2008/021588s024lbl.pdf>

131. U.S. Food and Drug Administration. FDA approves additional medical indication for Sprycel. (2010). at <http://www.fda.gov/NewsEvents/Newsroom/PressAnnouncements/ucm231409.htm>

132. Chow, L. Q. M. & Eckhardt, S. G. Sunitinib: from rational design to clinical efficacy. *J. Clin. Oncol.* **25,** 884–96 (2007).

133. Roskoski, R. Sunitinib: a VEGF and PDGF receptor protein kinase and angiogenesis inhibitor. *Biochem. Biophys. Res. Commun.* **356,** 323–8 (2007).

134. Muñoz, C. *et al.* Study of differences in the VEGFR2 inhibitory activities between semaxanib and SU5205 using 3D-QSAR, docking, and molecular dynamics simulations. *J. Mol. Graph. Model.* **32,** 39–48 (2012).

135. Pfizer. Sutent Prescribing Information. (2014). at <http://labeling.pfizer.com/ShowLabeling.aspx?id=607>

136. Schenone, S., Bondavalli, F. & Botta, M. Antiangiogenic agents: an update on small molecule VEGFR inhibitors. *Curr. Med. Chem.* **14,** 2495–516 (2007).

137. De Angelis, C. Side effects related to systemic cancer treatment: are we changing the Promethean experience with molecularly targeted therapies? *Curr. Oncol.* **15,** 198–9 (2008).

138. Singh, Y., Palombo, M. & Sinko, P. Recent trends in targeted anticancer prodrug and conjugate design. *Curr. Med. Chem.* **15,** 1802–1826 (2008).

139. Denny, W. Prodrug strategies in cancer therapy. *Eur. J. Med. Chem.* **36,** 577–595 (2001).

140. Huttunen, K. M., Raunio, H. & Rautio, J. Prodrugs - from serendipity to rational design. *Pharmacol. Rev.* **63,** 750–71 (2011).

141. Hwang, J. J. & Marshall, J. L. Capecitabine: fulfilling the promise of oral chemotherapy. *Expert Opin. Pharmacother.* **3,** 733–43 (2002).

142. Takiuchi, H. & Ajani, J. A. Uracil-tegafur in gastric carcinoma: a comprehensive review. *J. Clin. Oncol.* **16,** 2877–85 (1998).

143. Boddy, A. V & Yule, S. M. Metabolism and pharmacokinetics of oxazaphosphorines. *Clin. Pharmacokinet.* **38,** 291–304 (2000).

144. National Cancer Institute. Cyclophosphamide. (2013). at <http://www.cancer.gov/cancertopics/druginfo/cyclophosphamide>

145. Guise, C. P. *et al.* Bioreductive prodrugs as cancer therapeutics: targeting tumor hypoxia. *Chin. J. Cancer* **33,** 80–6 (2014).

146. Rooseboom, M., Commandeur, J. A. N. N. M. & Vermeulen, N. P. E. Enzyme-Catalyzed Activation of Anticancer Prodrugs. **56,** 53–102 (2004).

147. Carter, P. Improving the efficacy of antibody-based cancer therapies. *Nat. Rev. Cancer* **1,** 118–29 (2001).

148. Schrama, D., Reisfeld, R. A. & Becker, J. C. Antibody targeted drugs as cancer therapeutics. *Nat. Rev. Drug Discov.* **5,** 147–59 (2006).

149. Trail, P. Antibody Drug Conjugates as Cancer Therapeutics. *Antibodies* **2,** 113–129 (2013).

150. Lopus, M., Oroudjev, E. & Wilson, L. Maytansine and cellular metabolites of antibody-maytansinoid conjugates strongly suppress microtubule dynamics by binding to microtubules. *Mol. cancer …* **9,** 2689–2699 (2010).

151. Francisco, J. A. *et al.* cAC10-vcMMAE, an anti-CD30-monomethyl auristatin E conjugate with potent and selective antitumor activity. *Blood* **102,** 1458–65 (2003).

152. Horie, R., Higashihara, M. & Watanabe, T. Hodgkin's lymphoma and CD30 signal transduction. *Int. J. Hematol.* **77,** 37–47 (2003).

153. Tarkowski, M. Expression and a role of CD30 in regulation of T-cell activity. *Curr. Opin. Hematol.* **10,** 267–71 (2003).

154. Poncet, J. The dolastatins, a family of promising antineoplastic agents. *Curr. Pharm. Des.* **5,** 139–62 (1999).

155. Vaklavas, C. & Forero-Torres, A. Safety and efficacy of brentuximab vedotin in patients with Hodgkin lymphoma or systemic anaplastic large cell lymphoma. *Ther. Adv. Hematol.* **3,** 209–25 (2012).

156. Chari, R. V *et al.* Immunoconjugates containing novel maytansinoids: promising anticancer drugs. *Cancer Res.* **52,** 127–31 (1992).

157. Niculescu-Duvaz, I. Trastuzumab emtansine, an antibody-drug conjugate for the treatment of HER2+ metastatic breast cancer. *Curr. Opin. Mol. Ther.* **12,** 350–60 (2010).

158. Gillies, R. J. & Gatenby, R. a. Hypoxia and adaptive landscapes in the evolution of carcinogenesis. *Cancer Metastasis Rev.* **26,** 311–7 (2007).

159. Chan, D. a & Giaccia, A. J. Hypoxia, gene expression, and metastasis. *Cancer Metastasis Rev.* **26,** 333–9 (2007).

160. Semenza, G. L. Hypoxia and cancer. *Cancer Metastasis Rev.* **26,** 223–4 (2007).

161. Bertout, J. a, Patel, S. a & Simon, M. C. The impact of O2 availability on human cancer. *Nat. Rev. Cancer* **8,** 967–75 (2008).

162. Chung, A. S., Lee, J. & Ferrara, N. Targeting the tumour vasculature: insights from physiological angiogenesis. *Nat. Rev. Cancer* **10,** 505–14 (2010).

163. Farnsworth, R. H., Lackmann, M., Achen, M. G. & Stacker, S. A. Vascular remodeling in cancer. *Oncogene* (2013). doi:10.1038/onc.2013.304

164. Jain, R. K. Molecular regulation of vessel maturation. *Nat. Med.* **9,** 685–93 (2003).

165. Prekeges, J. L., Rasey, J. S., Grunbaum, Z. & Krohn, K. H. Reduction of fluoromisonidazole, a new imaging agent for hypoxia. *Biochem. ...* **42,** 2387–2395 (1991).

166. Jameson, M. B. *et al.* A phase i trial of PR-104, a nitrogen mustard prodrug activated by both hypoxia and aldo-keto reductase 1C3, in patients with solid tumors. *Cancer Chemother. Pharmacol.* **65,** 791–801 (2010).

167. Meng, F. *et al.* Molecular and cellular pharmacology of the hypoxia-activated prodrug TH-302. *Mol. Cancer Ther.* **11,** 740–51 (2012).

168. McCord, J. M. & Fridovich, I. Superoxide dismutase. An enzymic function for erythrocuprein (hemocuprein). *J. Biol. Chem.* **244,** 6049–6055 (1969).

169. Denny, W. A. W. Hypoxia-activated prodrugs in cancer therapy: progress to the clinic. *Futur. Oncol.* **6,** 419–428 (2010).

170. Palmer, B. D., Wilson, W. R., Pullen, S. M. & Denny, W. a. Hypoxia-selective antitumor agents. 3. Relationships between structure and cytotoxicity against cultured tumor cells for substituted N,N-bis(2-chloroethyl)anilines. *J. Med. Chem.* **33,** 112–21 (1990).

171. Duan, J.-X. *et al.* Potent and highly selective hypoxia-activated achiral phosphoramidate mustards as anticancer drugs. *J. Med. Chem.* **51,** 2412–20 (2008).

172. Roe, F. J. C. Metronidazole: view of uses and toxicity. *J. Antimicrob. Chemother.* **3,** 205–212 (1977).

173. Josephy, P. D., Palcic, B. & Skarsgard, L. D. In vitro metabolism of misonidazole. *Br. J. Cancer* **43,** 443–50 (1981).

174. Baillet, F., Housset, M., Dessard-Diana, B. & Boisserie, G. Positive clinical experience with misonidazole in brachytherapy and external radiotherapy. *Int. J. Radiat. Oncol. Biol. Phys.* **16,** 1073–5 (1989).

175. Dische, S. Chemical sensitizers for hypoxic cells: a decade of experience in clinical radiotherapy. *Radiother. Oncol.* **3,** 97–115 (1985).

176. Atwell, G. J., Sykes, B. M., O'Connor, C. J. & Denny, W. A. Relationships between structure and kinetics of cyclization of 2-aminoaryl amides: potential prodrugs of cyclization-activated aromatic mustards. *J. Med. Chem.* **37,** 371–380 (1994).

177. Blanche, E. a., Maskell, L., Colucci, M. a., Whatmore, J. L. & Moody, C. J. Synthesis of potential prodrug systems for reductive activation. Prodrugs for anti-angiogenic isoflavones and VEGF receptor tyrosine kinase inhibitory oxindoles. *Tetrahedron* **65,** 4894–4903 (2009).

178. Das, N., Dhanawat, M., Dash, B., Nagarwal, R. C. & Shrivastava, S. K. Codrug: An efficient approach for drug optimization. *Eur. J. Pharm. Sci.* **41,** 571–588 (2010).

179. Similä, S., Keinänen, S. & Kouvalainen, K. Oral antipyretic therapy: evaluation of benorylate, an ester of acetylsalicylic acid and paracetamol. *Eur. J. Pediatr.* **121,** 15–20 (1975).

180. Singleton, J. W. *et al.* A trial of sulfasalazine as adjunctive therapy in Crohn's disease. *Gastroenterology* **77,** 887–97 (1979).

181. Williams, C., Panaccione, R., Ghosh, S. & Rioux, K. Optimizing clinical use of mesalazine (5-aminosalicylic acid) in inflammatory bowel disease. *Therap. Adv. Gastroenterol.* **4,** 237–48 (2011).

182. Friedel, H. A., Campoli-Richards, D. M. & Goa, K. L. Sultamicillin. A review of its antibacterial activity, pharmacokinetic properties and therapeutic use. *Drugs* **37,** 491–522 (1989).

183. Mendel, D. B. *et al.* In Vivo Antitumor Activity of SU11248 , a Novel Tyrosine Kinase Inhibitor Targeting Vascular Endothelial Growth Factor and Platelet-derived Growth Factor Receptors : Determination of a Pharmacokinetic / Pharmacodynamic Relationship In Vivo Antitumor Activ. (2003).

184. Sun, L. *et al.* Synthesis and biological evaluations of 3-substituted indolin-2-ones: a novel class of tyrosine kinase inhibitors that exhibit selectivity toward particular receptor tyrosine kinases. *J. Med. Chem.* **41,** 2588–603 (1998).

185. Dubey, L. Side reactions of onium coupling reagents BOP and HBTU in the synthesis of silica polymer supports. *Ukr. Bioorganica Acta* **1,** 13–19 (2005).

186. Reybier, K. *et al.* Electrochemical behavior of indolone-N-oxides: relationship to structure and antiplasmodial activity. *Bioelectrochemistry* **88,** 57–64 (2012).

187. Nepveu, F. *et al.* Synthesis and antiplasmodial activity of new indolone N-oxide derivatives. *J. Med. Chem.* **53,** 699–714 (2010).

188. Ibrahim, H. *et al.* Antibacterial, antifungal and antileishmanial activities of indolone-N-oxide derivatives. *J. Antibiot. (Tokyo).* **65,** 499–504 (2012).

189. Trager, W. & Jensen, J. Human malaria parasites in continuous culture. *Science (80-.).* **193,** 673–675 (1976).

190. Desjardins, R. E., Canfield, C. J., Haynes, J. D. & Chulay, J. D. Quantitative assessment of antimalarial activity in vitro by a semiautomated microdilution technique. *Antimicrob. Agents Chemother.* **16,** 710–718 (1979).

191. O'Brien, J., Wilson, I., Orton, T. & Pognan, F. Investigation of the Alamar Blue (resazurin) fluorescent dye for the assessment of mammalian cell cytotoxicity. *Eur. J. Biochem.* **267,** 5421–5426 (2000).

192. Brown, K. J. *et al.* A novel in vitro assay for human angiogenesis. *Lab. Invest.* **75,** 539–555 (1996).

193. Medigen Biotechnology Corporation. A Phase III Study of PI-88 in the Adjuvant Treatment of Subjects With Hepatitis Virus Related Hepatocellular Carcinoma After Surgical Resection (PATRON). *Clinicaltrials.gov* at <http://clinicaltrials.gov/show/NCT01402908>

194. Lee, M. S. & Kim, S. Y. Synthesis of Poly(arylene ether)s Containing Triphenylamine Units via Nitro Displacement Reaction. *Macromolecules* **38,** 5844–5845 (2005).

195. Huang, A., Liu, F., Zhan, C., Liu, Y. & Ma, C. One-pot synthesis of pyrrolo[1,2-a]quinoxalines. *Org. Biomol. Chem.* **9,** 7351–7 (2011).

196. Ferlin, M. G., Dalla Via, L. & Gia, O. M. Synthesis and antiproliferative activity of some new DNA-targeted alkylating pyrroloquinolines. *Bioorg. Med. Chem.* **12,** 771–7 (2004).

197. Hay, M. P., Anderson, R. F., Ferry, D. M., Wilson, W. R. & Denny, W. a. Synthesis and evaluation of nitroheterocyclic carbamate prodrugs for use with nitroreductase-mediated gene-directed enzyme prodrug therapy. *J. Med. Chem.* **46,** 5533–45 (2003).

198. Porwanski, S. *et al.* Bis-β-cyclodextrinyl- and bis-cellobiosyl-diazacrowns: synthesis and molecular complexation behaviors toward Busulfan anticancer agent and two basic aminoacids. *Tetrahedron* **65,** 6196–6203 (2009).

199. Gamble, A. B., Garner, J., Gordon, C. P., O'Conner, S. M. J. & Keller, P. A. Aryl Nitro Reduction with Iron Powder or Stannous Chloride under Ultrasonic Irradiation. *Synth. Commun.* **37,** 2777–2786 (2007).

200. Desai, D. G., Swami, S. S. & Hapase, S. B. Rapid and Inexpensive Method for Reduction of Nitroarenes to Anilines. *Synth. Commun.* **29,** 1033–1036 (1999).

201. Pogorelić, I. *et al.* Rapid, efficient and selective reduction of aromatic nitro compounds with sodium borohydride and Raney nickel. *J. Mol. Catal. A Chem.* **274,** 202–207 (2007).

202. Bouérat, L. *et al.* Indolin-2-ones with high in vivo efficacy in a model for multiple sclerosis. *J. Med. Chem.* **48,** 5412–5414 (2005).

203. Schmidt, F. *et al.* Glucuronide prodrugs of hydroxy compounds for antibody directed enzyme prodrug therapy (adept): A phenol nitrogen mustard carbamate. *Bioorganic Med. Chem. Lett.* **7,** 1071–1076 (1997).

204. Selva, M., Fabris, M., Lucchini, V., Perosa, A. & Noè, M. The reaction of primary aromatic amines with alkylene carbonates for the selective synthesis of bis-N-(2-hydroxy)alkylanilines: the catalytic effect of phosphonium-based ionic liquids. *Org. Biomol. Chem.* **8,** 5187–5198 (2010).

205. Lazareva, N. F., Albanov, A. I., Lazarev, I. M. & Pestunovich, V. A. N,N,N′,N′,N″-Pentamethyl-N″-[(trifluorosilyl)methyl] phosphoric triamide. First example of the existence of intramolecular P=O→Si coordination bond in the Si-containing phosphoric triamides. *Appl. Organomet. Chem.* **21,** 281–287 (2007).

206. Sun, L. *et al.* Synthesis and biological evaluations of 3-substituted indolin-2-ones: A novel class of tyrosine kinase inhibitors that exhibit selectivity toward particular receptor tyrosine kinases. *J. Med. Chem.* **41,** 2588–2603 (1998).

207. Sun, L. *et al.* Discovery of 5-[5-fluoro-2-oxo-1,2- dihydroindol-(3Z)-ylidenemethyl]-2,4- dimethyl-1H-pyrrole-3-carboxylic acid (2-diethylaminoethyl)amide, a novel tyrosine kinase inhibitor targeting vascular endothelial and platelet-derived growth factor receptor tyrosi. *J. Med. Chem.* **46,** 1116–1119 (2003).

208. Morriello, G. J. *et al.* Fused bicyclic pyrrolizinones as new scaffolds for human NK1 antagonists. *Bioorg. Med. Chem.* **16,** 2156–70 (2008).

209. Morriello, G. J. *et al.* Substituted fused bicyclic pyrrolizinones as potent, orally bioavailable hNK1 antagonists. *Bioorg. Med. Chem. Lett.* **20,** 2007–12 (2010).

210. Park, Y. C., Gunasekera, S. P., Lopez, J. V, McCarthy, P. J. & Wright, A. E. Metabolites from the marine-derived fungus Chromocleista sp. isolated from a deep-water sediment sample collected in the Gulf of Mexico. *J. Nat. Prod.* **69,** 580–4 (2006).

211. Despinoy, X. L. M. & McNab, H. Hydrogenation of pyrrolizin-3-ones; new routes to pyrrolizidines. *Org. Biomol. Chem.* **7,** 4502–11 (2009).

212. Pinho, T. M. V. D., Soares, M. I. L. & Paixa, A. N -Vinyl- and C -Vinylpyrroles from Azafulvenium Methides . Flash Vacuum Pyrolysis Route to 5-Oxo-5 H -pyrrolizines and 1-Azabenzo [f] azulenes. 6629–6638 (2005).

213. McNab, H. & Thornley, C. New chemistry of pyrrolizin-3-one: a concise route to 3,8-didehydroheliotridin-5-one. *J. Chem. Soc. Chem. Commun.* 1570 (1993). doi:10.1039/c39930001570

214. Clark, B. A. J., Despinoy, X. L. M., McNab, H., Sommerville, C. C. & Stevenson, E. Pyrolytic cyclisation reactions of 3-azolylpropenyl alcohols; unexpectedly facile thermal decomposition of 5H-pyrrolo[2,1-a]isoindole. *J. Chem. Soc. Perkin Trans. 1* 2049–2052 (1999). doi:10.1039/a904884g

215. Mcnab, H. & Thornley, (the Late) Craig. Chemistry of pyrrolizinones. Part 1. Reactions of pyrrolizin-3-ones with electrophiles: synthesis of 3,8-didehydroheliotridin-5-ones. *J. Chem. Soc. Perkin Trans. 1* **1,** 3584–3591 (2000).

216. McNab, H., Montgomery, J., Parsons, S. & Tredgett, D. G. Pyrrolizine-1,3-dione. *Org. Biomol. Chem.* **8,** 4383–7 (2010).

217. Sudta, P. *et al.* Synthesis, Structural Characterisation, and Preliminary Evaluation of Non-Indolin-2-one-based Angiogenesis Inhibitors Related to Sunitinib (Sutent). *Aust. J. Chem.* **66,** 864 (2013).

218. Aranda, E. & Owen, G. I. A semi-quantitative assay to screen for angiogenic compounds and compounds with angiogenic potential using the EA.hy926 endothelial cell line. *Biol. Res.* **42,** 377–89 (2009).

219. Invitrogen. Endothelial Tube Formation Assay (In Vitro Angiogenesis). at <http://tools.lifetechnologies.com/content/sfs/manuals/Endothelial_Cells_Tube_Formation.pdf>

220. Lo Meo, P., D'Anna, F., Riela, S., Gruttadauria, M. & Noto, R. Host–guest interactions involving cyclodextrins: useful complementary insights achieved by polarimetry. *Tetrahedron* **63,** 9163–9171 (2007).

221. Otwinowski, Z. & Minor, W. in *Methods Enzymol.* 307–326 (1997). doi:10.1016/S0076-6879(97)76066-X

222. Agilent Technologies. CrysAlis PRO. (2013).

223. Altomare, A. *et al.* SIR 92 – a program for automatic solution of crystal structures by direct methods. *J. Appl. Crystallogr.* **27,** 435 (1994).

224. Betteridge, P. W., Carruthers, J. R., Cooper, R. I., Prout, K. & Watkin, D. J. CRYSTALS version 12: software for guided crystal structure analysis. *J. Appl. Crystallogr.* **36,** 1487–1487 (2003).

225. Altomare, A. *et al.* SIR 97: a new tool for crystal structure determination and refinement. *J. Appl. Crystallogr.* **32,** 115–119 (1999).

226. Sheldrick, G. M. A short history of SHELX. *Acta Crystallogr. Sect. A Found. Crystallogr.* **64,** 112–122 (2008).